ABSTRACT

BUSH, BLAKE MARSHALL. Analytical Evaluation of Concrete Penetration Modeling Techniques. (Under the direction of Dr. Emmett Sumner.)

The resistance of concrete targets to penetration of high speed projectiles is a topic of high value in the national security and catastrophic design fields. Many methods have been developed to effectively analyze these types of problems. Currently there are a number of numerical codes and constitutive models used to analyze concrete impact and penetration with new methods developed continuously.

This research evaluates the accuracy of four analysis codes and five concrete constitutive models. Two Lagrangian analysis programs, EPIC and LS-DYNA, as well as an Eulerian code, CTH, are compared in this work. A developmental version of the Material Point Method is also evaluated in order to study the effectiveness of Arbitrary Lagrangian Eulerian (ALE) modeling methods for concrete impact and penetration. The concrete models evaluated in this research include Holmquist Johnson Cook, Brittle Failure Kinetics, Osborn, Karagozian and Case, and Drucker-Prager. The modeling programs and constitutive models are evaluated by comparing simulation results to a series of concrete impact and penetration experiments.

The experimental test data, provided by Sandia National Laboratories, comprises concrete targets of two compressive strengths (3.3 and 5.7 ksi) and two thicknesses and projectiles of two nose shapes. Extensive material testing of the experimental concrete is used to calibrate the constitutive models in each analysis package. An additional parametric study investigates the influence of experimental variables on the most promising analytical configuration.

Observations from this research show that the EPIC and LS-DYNA analysis codes are currently best suited for concrete impact and penetration problems. Both codes contain features which allow for realistic modeling and produce accurate results for the experimental impact tests. Recommendations for improving analysis methods specific to concrete impact and penetration are presented.

Analytical Evaluation of Concrete Penetration Modeling Techniques

by
Blake Marshall Bush

A thesis submitted to the Graduate Faculty of
North Carolina State University
in partial fulfillment of the
requirements for the Degree of
Master of Science

Civil Engineering

Raleigh, North Carolina

2010

APPROVED BY:

Dr. Murthy Guddati	Dr. Sami Rizkalla

Dr. Emmett Sumner
Chair of Advisory Committee

DEDICATION

This thesis is dedicated to my wife and my parents. Without your continued support and encouragement this work would have been impossible. Thank you!

BIOGRAPHY

Blake Bush was born March 13th, 1985 to Phillip and Amy Bush. He was raised in Laurinburg, North Carolina and later Holly Springs, North Carolina. His family then spent five years in West Monroe, Louisiana until finally moving to Concord, North Carolina where he attended Northwest Cabarrus High School. Interested in mathematics and physics, Blake decided to pursue a degree in Engineering at NC State University. Blake continued to enjoy the study of Structural Engineering and Design, and decided to continue his education with a Master's of Science in Civil Engineering at NC State. Upon completion of his degree in the spring of 2010, he plans to pursue a career in structural engineering in the Raleigh area to gain experience and ultimately receive a Professional Engineer's license.

ACKNOWLEDGMENTS

Sincere appreciation is owed to many individuals who helped me along the way: Dr. Emmett Sumner, Dr. Steve Lorenc, Dr. Stephanie Termaath, Beth Smith, Dr. James Pearson, Lee Nelson, Martin Cardenas, and Kevin Kennedy.

TABLE OF CONTENTS

LIST OF TABLES viii
LIST OF FIGURES ix
LIST OF SYMBOLS, ABBREVIATIONS, AND NOMENCLATURE xii
1. Introduction 1
1.1. Background 1
1.2. Objectives 2
1.3. Scope 3
1.4. Conclusion 3
2. Literature Review 4
2.1. Definition of Concrete Impact 4
2.2. Modeling Techniques 8
2.2.1. Kinematic Descriptions 8
2.2.2. Discretization Methods 14
2.3. Constitutive Models 21
2.3.1. Plasticity Models 22
2.3.2. Continuum Damage Models 31
2.3.3. Constitutive Models Summary 49
2.4. Available Experimental Work 49
2.5. Need for Research 51
3. Basic Problem 53
3.1. Experimental Data 54
3.1.1. Projectile 55
3.1.2. Target 57
3.1.3. Initial and Boundary Conditions 60
3.2. Analysis Methods 61
3.2.1. Material Models 61
3.2.2. Analysis Packages 62
3.2.3. Summary of Packages and Models 65
3.3. Comparison and Evaluation 67
3.3.1. Preliminary Evaluation 67
3.3.2. Method Comparison 67
3.3.3. Experimental Parameter Study 68
3.3.4. Evaluation Criteria 68
3.3.5. Conclusion 71
4. Analytical Investigation 73
4.1. EPIC 73
4.1.1. Input Data 74
4.1.2. Material Models 75
4.1.3. Contact Definition 82
4.1.4. Output Data 83

4.1.5. Code Use ... 83
4.2. LS-DYNA ... 85
4.2.1. Input Data ... 85
4.2.2. Material Models ... 87
4.2.3. Contact Definition ... 92
4.2.4. Output Data ... 92
4.2.5. Code Use ... 93
4.3. CTH ... 94
4.3.1. Input Data ... 94
4.3.2. Material Models ... 96
4.3.3. Output Data ... 98
4.3.4. Code Use ... 98
4.4. Material Point Method (MPM) ... 99
4.4.1. Input Data ... 99
4.4.2. Material Models ... 100
4.4.3. Output Data ... 102
4.4.4. Code Use ... 103
5. Analysis Pairing Comparison Results ... 108
5.1. Preliminary Evaluation ... 109
5.1.1. Penetration Depth ... 110
5.1.2. Projectile Mass Loss ... 111
5.1.3. Deceleration ... 112
5.1.4. Modeling Feature Capabilities ... 120
5.1.5. CPU Run Time ... 121
5.1.6. Conclusions ... 122
5.2. Method Comparison ... 123
5.2.1. Penetration Depth ... 124
5.2.2. Projectile Mass Loss ... 125
5.2.3. Deceleration ... 126
5.2.4. Modeling Feature Capabilities ... 136
5.2.5. Run Time ... 136
5.2.6. Conclusions ... 137
6. Experimental Parameter Study ... 139
6.1. Penetration Depth ... 140
6.2. Projectile Mass Loss ... 144
6.3. Deceleration ... 148
6.4. Damage Plots ... 166
6.5. Conclusions ... 171
7. Conclusions ... 174
7.1. Observations ... 174
7.2. Recommendations for Future Work ... 176
REFERENCES ... 178
APPENDICES ... 185

Appendix A 186
1. Experimental Parameter Study Deceleration Plots 186
1.1. SNL-1 186
1.2. SNL-2 187
1.3. SNL-3 187
1.4. SNL-4 188
1.5. SNL-5 188
1.6. SNL-6 189
1.7. SNL-7 189
1.8. SNL-8 190
1.9. SNL-9 190
1.10. SNL-10 191
1.11. SNL-11 191
1.12. SNL-12 192
1.13. SNL-14 192
1.14. SNL-15 193
1.15. SNL-16 193
2. Experimental Parameter Study Damage Plots 194
2.1. SNL-1 194
2.2. SNL-2 195
2.3. SNL-3 196
2.4. SNL-4 197
2.5. SNL-5 198
2.6. SNL-6 199
2.7. SNL-7 200
2.8. SNL-8 201
2.9. SNL-9 202
2.10. SNL-10 203
2.11. SNL-11 204
2.12. SNL-12 205
2.13. SNL-14 206
2.14. SNL-15 207
2.15. SNL-16 208

LIST OF TABLES

Table 1. Classification of Impact Response by Velocity (Zukas, 1980) 5
Table 2. Classification of Impact Regimes by Impact Pressures and Material Strength (Wilbeck, 1985) 6
Table 3. Concrete Impulse Loading Case Studies 50
Table 4. Experimental Test Matrix (Forrestal, Frew, Hickerson, & Rohwer, 2002)..... 55
Table 5. Mix Design and Properties of the Experimental Concrete (Forrestal, Frew, Hickerson, & Rohwer, 2002) 58
Table 6. Analysis Matrix for Target Material Models 66
Table 7. Analysis Matrix for Projectile Material Models 66
Table 8. Method Comparison Test Matrix..... 68
Table 9. Sample Grading System..... 71
Table 10. JC Material Constants 76
Table 11. Osborn Material Constants 77
Table 12. HJC Material Constants for Low and Conventional Strength Concretes 81
Table 13. Summary of K&C Strength Material Parameters 89
Table 14. Summary of K&C Equation of State Material Parameters 90
Table 15. Summary of K&C Damage Material Parameters 91
Table 16. BFK Material Constants 97
Table 17. BFK Reference Equation of State Values..... 97
Table 18. DP Material Constants 102
Table 19. Analysis Matrix for Target Material Models 108
Table 20. Deceleration Grading for Preliminary Evaluation 119
Table 21. Preliminary Evaluation Grading 122
Table 22. Deceleration Descending Slope Linear Trend Lines for Method Comparison 132
Table 23. Deceleration Grading for the Method Comparison 135
Table 24. Method Comparison Run Times..... 137
Table 25. Method Comparison Grading 137

LIST OF FIGURES

Figure 1. System Response (Cargile D. , 1998) 7
Figure 2. Comparison of Lagrangian, Eulerian, and ALE Descriptions (Donea, Huerta, Ponthot, & Rodriguez-Ferran, 2004) 12
Figure 3. Lagrange Interpolation and Shape Functions: a) Linear, b) Quadratic (Cook, Malkus, Plesha, & Witt, 2002) 16
Figure 4. Symmetric Tetrahedral Arrangement (Johnson, et al., 2006) 18
Figure 5. Eight-node Solid Hexahedron Element (Hallquist, 2006) 19
Figure 6. von Mises and Drucker-Prager Yield Surface 26
Figure 7. Osborn Model a) Strength b) Pressure (Johnson, et al., 2006) 29
Figure 8. HJC Model (Holmquist, Johnson, & Cook, 1993) 32
Figure 9. BFK: a) Equation of State, b) Strength (Silling, 1997) 36
Figure 10. BFK Damage: Triaxial Failure Envelope (Silling, 1997) 38
Figure 11. K&C Strength Model a) Strength vs. Pressure, b) Typical Stress-Strain Curve (Malvar & Simons, 1996) 40
Figure 12. a) Deviatoric Sections of the K&C Failure Surface (Malvar & Simons, 1996), b) William and Warnke Model (Noble, Kokko, Darnell, Dunn, Hagler, & Leininger, 2005) 41
Figure 13. a) Shear Dilation of the K&C Model, b) Concrete Aggregate Interlock (Noble, Kokko, Darnell, Dunn, Hagler, & Leininger, 2005) 43
Figure 14. Typical CSCM Strength Model: a) vs. Pressure, b) Deviatoric Plane (Murray, 2007) 46
Figure 15. Example of Strain Softening and Modulus Reduction by Damage (Murray, 2007) 47
Figure 16. Experimental Setup of Impact Study 53
Figure 17. a) 3.0 CRH, b) 6.0 CRH Projectile Geometries in Inches (Forrestal, Frew, Hickerson, & Rohwer, 2002) 56
Figure 18. Relative Target Resistance with Respect to the Target-Projectile Diameter Ratio (Sjol & Teland, 2001) 59
Figure 19. Experimental Target Setup (Frew, 2002) 60
Figure 20. SNL-16 Deceleration and Example Grading System 70
Figure 21. Target Damage and Crater Profile for Validation 71
Figure 22. Example Three-Dimensional EPIC Mesh 75
Figure 23. Fitting of HJC Pressure Model for Low Strength Concrete 80
Figure 24. Example LS-DYNA Target Mesh 87
Figure 25. CTH Boundary Condition Diagram 96
Figure 26. Tecplot Output Example: a) Full, b) Zoomed 103
Figure 27. MPM Taylor Impact Example Results: Experimental (left)(Johnson & Holmquist, 1988) and Analytical (right) 104
Figure 28. MPM Taylor Impact Validation Results 106
Figure 29. Penetration Depth for Preliminary Evaluation 111
Figure 30. Projectile Mass Loss for Preliminary Evaluation 112

Figure 31. Deceleration Comparisons for Preliminary Evaluation 113
Figure 32. Peak Decelerations of the Preliminary Evaluation 114
Figure 33. Peak Deceleration of FEM codes for Preliminary Evaluation 115
Figure 34. Preliminary Evaluation Deceleration 116
Figure 35. Deceleration End Time for Preliminary Evaluation 117
Figure 36. Deceleration End Times of FEM Codes for Preliminary Evaluation 118
Figure 37. CPU Run Time for Preliminary Evaluation 121
Figure 38. Penetration Depth for Method Comparison 125
Figure 39. Projectile Mass Loss for Method Comparison 126
Figure 40. Decelerations for the Method Comparison 128
Figure 41. Peak Deceleration for the Method Comparison 129
Figure 42. Deceleration Descending Slopes for Method Comparison 131
Figure 43. Deceleration End Times for the Method Comparison 134
Figure 44. HJC Low Strength Erosion Strain Determination 140
Figure 45. Penetration Depth for Low Strength Concrete Targets 141
Figure 46. Penetration Depth for Conventional Strength Targets 143
Figure 47. Penetration Depth with Increasing Initial Kinetic Energy for Low (LS) and Conventional Strength (CS) Concrete Targets 144
Figure 48. Projectile Mass Loss for Low Strength Concrete Targets 145
Figure 49. Projectile Mass Loss for Conventional Strength Targets 146
Figure 50. Projectile Mass Loss with Increasing Initial Kinetic Energy for Low (LS) and Conventional Strength (CS) Targets 148
Figure 51. Experimental and E-1 Comparison for Test SNL-5 149
Figure 52. Peak Decelerations for Low Strength Concrete Targets 150
Figure 53. Peak Decelerations for Four ft. Thick Conventional Strength Targets 151
Figure 54. Peak Decelerations for Six ft. Thick Conventional Strength Targets 152
Figure 55. Peak Decelerations for Low Strength Concrete Tests with Increasing Impact Velocity 154
Figure 56. Peak Deceleration for Conventional Strength Concrete Tests with Increasing Impact Velocity 155
Figure 57. Low Strength Concrete Descending Slopes 156
Figure 58. Low Strength Concrete Linear Fit Descending Slopes 157
Figure 59. Four ft. Thick Conventional Strength Target Descending Slopes 158
Figure 60. Deceleration Descending Slopes for Four ft. Thick Conventional Strength Concrete Targets 159
Figure 61. Deceleration Descending Slopes for Six ft. Thick Conventional Strength Concrete Targets 160
Figure 62. Linear Fit Deceleration Descending Slopes for Six ft. Thick Conventional Strength Concrete Targets 161
Figure 63. Deceleration End Times for Low Strength Concrete Targets 162
Figure 64. Deceleration End Times for Four ft. Thick Conventional Strength Concrete Targets 163

Figure 65. Deceleration End Times for Six ft. Thick Conventional Strength Concrete Targets 165
Figure 66. SNL-6 Damage: Experimental (left) and E-1 (right) 167
Figure 67. SNL-6 Damage Profiles: Experimental (yellow) Superimposed on E-1 Results (contour)..... 168
Figure 68. SNL-16 Damage: Experimental (left) and E-1 (right) 169
Figure 69. SNL-16 Damage Profiles: Experimental (yellow) Superimposed on E-1 Results (contour)..... 169
Figure 70. Comparison of Experimental Damage for Tests SNL-4 and SNL-7..... 170
Figure 71. Comparison of Experimental Damage for Tests SNL-14 and SNL-16..... 171

LIST OF SYMBOLS, ABBREVIATIONS, AND NOMENCLATURE

Abbreviations and Nomenclature:

VM	von Mises
JC	Johnson Cook Model
DP	Drucker-Prager
HJC	Holmquist Johnson Cook
BFK	Brittle Failure Kinetics
K&C	Karagozian & Case
CSCM	Continuous Surface Cap Model
EPIC	Elastic Plastic Impact Calculations
CTH	Chart Two and a Half
MPM	Material Point Method
PIC	Particle-in-Cell
TXC	Triaxial Compression
TXE	Triaxial Extension
TOR	Torsion
FEM	Finite Element Method

FDM	Finite Difference Method

Variable Definitions:

IP	Impact Pressure
P	Pressure
σ	Equivalent Strength, Stress
σ_{ij}	Total Stress Tensor
ε	Equivalent Strain
ε_{ij}	Total Strain Tensor
E	Elastic Modulus
μ	Volumetric Strain
V	Current Volume (Osborn)
V_0	Original Volume (Osborn)
$\dot{\varepsilon}$	Strain Rate
σ_T	Target Strength
σ_P	Projectile Strength
σ_y	Yield Strength
σ_1, σ_2, σ_3	Principal Stresses
σ_{eq}	Equivalent Stress
σ_a	Axial Stress

σ_r	Radial Stress
I_1	First Invariant of the Stress Tensor
J_2	Second Invariant of the Deviatoric Stress Tensor
J_3	Third Invariant of the Deviatoric Stress Tensor
θ	Angle of Similarity
φ	Internal Angle of Friction
$f'c$	Unconfined Compressive Strength (First Yield Strength for DP)
$f't$	Direct Tensile Strength (First Yield Strength for DP)
ξ	Haigh–Westergaard Coordinate Representation of Pressure Influence
ρ	Haigh–Westergaard Coordinate Representation of Deviatoric Stress
$\dot{\varepsilon}^*$	Normalized Equivalent Strain Rate
P_{crush}	Crushing Pressure
μ_{crush}	Crushing Volumetric Strain
P_{lock}	Locking Pressure
μ_{lock}	Locking Volumetric Strain
σ_{max}	Maximum Equivalent Strength, Stress (Osborn)
P^*	Normalized Pressure
T	Tensile Strength
T^*	Normalized Tensile Strength

σ^*	Normalized Equivalent Strength, Stress
SMAX	Maximum Normalized Equivalent Strength, Stress (HJC)
D	Damage Parameter (HJC)
ε_p^f	Equivalent Plastic Strain to Fracture
EFMIN	Minimum Equivalent Plastic Strain to Fracture
μ_p^f	Volumetric Plastic Strain to Fracture
ϕ	Damage Rate Parameter
Y	Equivalent Strength, Stress (BFK)
Y_{max}	Maximum Equivalent Strength, Stress (BFK)
T_1	Maximum Tensile Principal Stress
p_{ref}	Reference Pressure
p	Current Pressure
v	Current Specific Volume
v_0	Original Specific Volume
Ω	Overload
λ	Shear Damage Parameter
$\Delta\lambda$	Volumetric Damage Parameter
r_f	Rate Enhancement Factor

$\overline{\varepsilon^p}$	Effective Plastic Strain
ε_v	Current Volumetric Strain
ε_{vy}	Volumetric Yield Strain
k_d	Internal Scalar Multiplier
f_d	Closeness Parameter
ω	Associativity Parameter
θ_n	Flow Angle for no Shear Dilation
d	Damage Parameter (CSCM)
$\mathcal{R}$	Rubin Function
β	Angle in Deviatoric Plane

Arbitrary Constants:

α, k, β, A, B, N, C, K_1, K_2, K_3, D_1, D_2, b_1, b_2, b_3

Mathematical Symbols:

exp	Euler's constant, e

BUSH, BLAKE MARSHALL. Analytical Evaluation of Concrete Penetration Modeling Techniques.
Introduction

ANALYTICAL EVALUATION OF CONCRETE PENETRATION MODELING TECHNIQUES

1. Introduction

1.1. Background

Impact studies have traditionally focused on military applications (Zukas, 1980); however, research interests now include that of shock compaction of powders, and modeling of void growth (Benson, 1992). Also, a developing interest has arisen for high strain rate events including collisions of automobiles, impact design for air and space vehicles, as well as processes involved in manufacturing (Benson, 1992). Zukas (1980) further includes uses for impact studies such as hazardous material transfer, nuclear structure impact design, lightweight armor design, explosive forming and welding of metals, and erosion of solids due to fluid or particle impact.

Impact and penetration problems can range from storm launched debris impacting a structure to a military attack with penetrating weapons (Cargile D. , 1998). These problems, particularly those involving concrete, have become the focus of much research in the past three decades. Increasing availability of experimental data has allowed for the development and validation of analytical modeling methods.

Impact and penetration of concrete involves complex material response that makes obtaining an accurate analytical solution difficult. However, compared with physical experiments that can be financially burdensome, numerical modeling can become a practical and effective alternative (Ma & Zhang, 2007). Additionally, if conditions such as range, velocity, or impact angle outside of laboratory limits need to be studied, numerical modeling becomes necessary to further understand or predict a particular phenomenon. For these reasons, effective numerical modeling techniques are vital to the study of impact and penetration problems.

1.2. Objectives

The primary objective of this research is to evaluate numerical modeling options for concrete impact and penetration. Four software programs are selected for evaluation; they are EPIC, LS-DYNA, CTH, and MPM. These programs are compared through a grading system based on their ability to capture concrete penetration behavior and their effectiveness with respect to configuration limits and computational cost. Concrete constitutive models are also assessed in this research; these models include Drucker-Prager, Osborn, Holmquist Johnson Cook, Brittle Failure Kinetics, and Karagozian and Case models. In addition to a comparison of modeling techniques, this research will study the influence of experimental variables on analytical accuracy.

1.3. Scope

An experimental test series performed by Sandia National Laboratories over a five month period from September 2000 to February 2001 is used as validation criteria (Rowher, Heise, & Wilder, 2001). The experimental series consisted of extensive material characterization of the target and projectile, as well as thorough data instrumentation of the impact tests. A subset of the experimental impact tests is chosen for evaluating the modeling methods and constitutive models. A single numerical approach is then applied to the entire experimental test series to further assess the code performance.

1.4. Conclusion

This document contains a survey of previous work regarding impact and penetration, modeling methods, concrete constitutive models, and available experimental data. A summation of the experimental parameters and analysis packages is presented, followed by more in depth methodology and discussion of user experience. The results of the numerical modeling software evaluation and the sensitivity study of an individual analysis configuration are discussed. The final chapter summarizes the observations of this research and provides recommendations for future work.

2. Literature Review

Modeling of concrete impact and penetration has many useful applications that include a range of responses and resulting phenomena. For this reason, many modeling methods and constitutive relations are continuously created and extended. The following section presents a summary of impact problems, material impact response, modeling methods, concrete constitutive models, and available experimental data.

2.1. Definition of Concrete Impact

Impact problems range widely and can be classified by key variables including impact velocity, impact pressure, projectile strength, and target strength as shown in Table 1 and Table 2. Table 1 shows the effect of strain rate upon material impact response and the loading methods that can be used to study the velocity ranges of interest. Table 2 shows typical impact scenarios according to the impact pressure and strengths of the projectile and target.

Table 1. Classification of Impact Response by Velocity (Zukas, 1980)

Striking Velocity (km/s)	Strain Rate (m/m/s)	Effect	Loading Method
>12	10^8	Explosive impact; colliding solids vaporize	Two-stage guns
3 – 12	10^7	Hydrodynamic; material compressibility cannot be ignored	Explosive acceleration
1 – 3	10^5	Materials behave as fluids; pressures approach or exceed material strength; density a dominant property	Powder and gas guns
0.5 – 1	10^4	Viscous; material still strength significant	Powder guns
0.05 – 0.5	10^2	Plastic deformations	Mechanical devices
<0.05	10^0	Elastic; some local plasticity	Mechanical devices

Table 2. Classification of Impact Regimes by Impact Pressures and Material Strength (Wilbeck, 1985)

	$IP/\sigma_T << 1$	$IP/\sigma_T \sim 1$	$IP/\sigma_T >> 1$
$IP/\sigma_P << 1$	Elastic Impact: Impact of two billiard balls, collision of a ball and bat, tire rolling on pavement	Projectiles penetrating concrete, explosively launched debris	Hard Penetrator into Soft Target: Earth penetrators, torpedoes in water, flight of aircraft
$IP/\sigma_P \sim 1$	Fruit pickers, head injury from windshield impact	Design of armor and armor penetrators, containment of turbine components, impact of hard objects on aircraft engine components	Containment of turbine components, projectiles penetrating concrete
$IP/\sigma_P >> 1$	Soft Penetrator into Hard Target: Birds impacting aircraft canopies at low flight velocity, lead bullets impacting a steel plate	Tornado-driven missiles, bird and hail impacts, rain erosion	Significant Material Failure: Hypervelocity impacts,

IP – Impact Pressures, σ_P – Projectile Strength, σ_T – Target Strength

The phenomena resulting from the impact of a projectile with a concrete target can also be classified into individual areas of study. Cargile lists possible responses as projectile defeat, ricochet, broach, perforation, and penetration (Figure 1 (1998)).

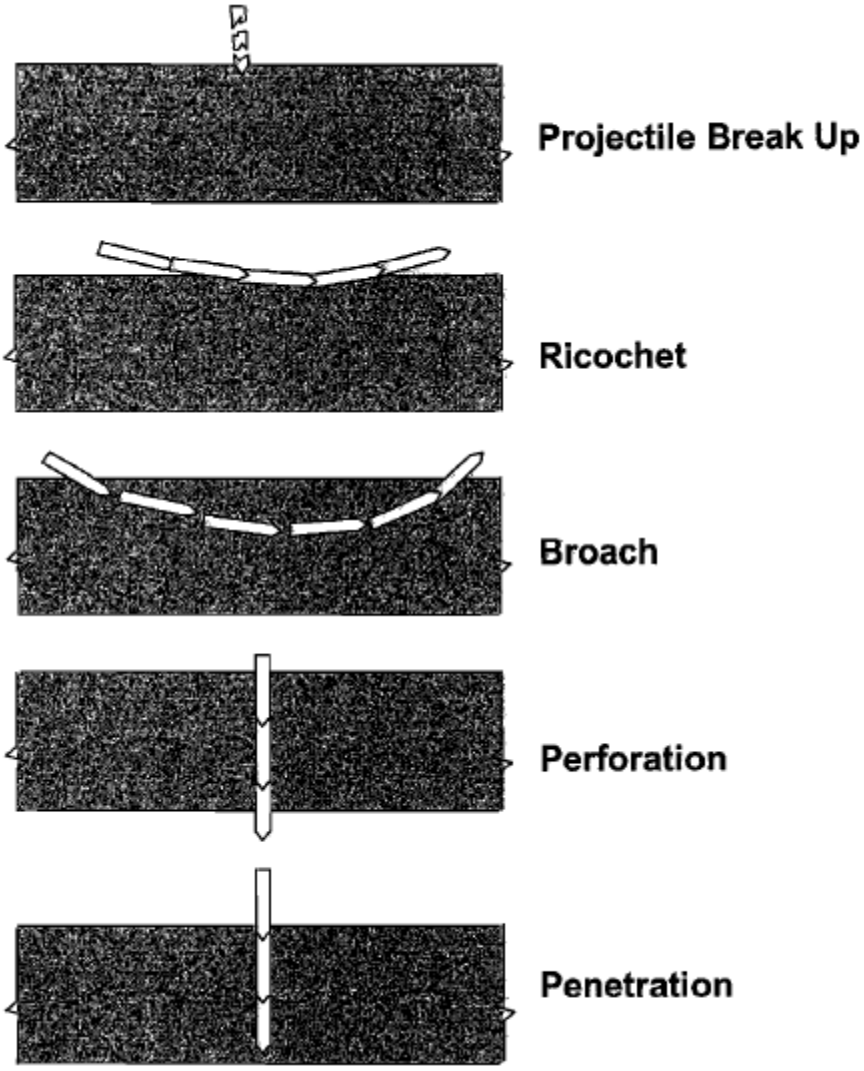

Figure 1. System Response (Cargile D. , 1998)

These responses are influenced by the material properties of the projectile and target as well as the impact conditions. Much of the early concrete impact work studied target perforation

and penetration. Perforation is the complete piercing of a target by a projectile, whereas penetration is entrance of a projectile into a target without complete passage (Zukas, 1980). These two processes result in large deformations in both projectile and target. Availability of research into projectile ricochet and broach are limited possibly due the difficulty of safe experimental control and data collection.

2.2. Modeling Techniques

Analytical techniques of projectile penetration analysis are empirical equations, analytical models, and numerical methods (Cargile D. , 1998; Jonas & Zukas, 1978). Of these methods the most detailed level of analysis is numerical methods; the techniques in this section will be focused on numerical methods used in impact modeling. Numerical methods can be characterized by three essential aspects involved in any simulation: kinematic description, discretization, and solution method.

2.2.1. Kinematic Descriptions

The kinematic description is the method of following motion. Two major kinematic descriptions were originally used for impact type problems: Lagrangian and Eulerian. While these two descriptions continue to be represented in the majority of impact modeling codes, additional techniques have been developed that couple the two or form extensions of the base

methods. Of these additional methods, only Arbitrary Lagrangian Eulerian (ALE) and meshless methods will be presented in this section.

2.2.1.1. Lagrangian

Lagrangian methods use dynamic grids to follow the distortion of materials. The governing conservation equations are solved on the deformed mesh at discrete points in time. Cells are only allowed to contain individual materials; they cannot contain a mix of multiple materials. This trait requires slide lines or contact definitions to handle material contact. For a particular cell in a Lagrangian point of reference, mass remains constant throughout computation, but the volume is allowed to change due to extension or compression of the material. Lagrangian analysis programs have grown in popularity and are commonly selected for modeling collision and manufacturing problems (Benson, 1992). LS-DYNA is a Lagrangian analysis software commonly used for these problems. Lagrangian techniques are advantageous for impact of brittle materials because of the ease at which history dependent material models can be implemented; however, Lagrangian methods exhibit inaccuracies with computations involving large deformations resulting in highly distorted meshes. (Anderson, 1987)

2.2.1.2. Eulerian

Eulerian methods use a stationary mesh through which material is advected. The flow into and out of a fixed cell is used to calculate new values for field variables in that cell. While early implementation of Eulerian methods involved mass particles, most modern versions use continuous materials. CTH (Crawford, et al., 2007) is a popular Eulerian code (Mair, 1999), and has been frequently employed for impact research (Senft & Stewart, 2007; Donea, Huerta, Ponthot, & Rodriguez-Ferran, 2004). Eulerian methods present great advantages in models with large deformation due to their ability to capture this behavior without a deformed mesh. Impact modeling with Lagrangian techniques often requires remeshing or erosion algorithms to maintain numerical stability; this can be avoided with an Eulerian frame of reference. Because the mesh is stationary throughout calculation, Eulerian cells are allowed to contain multiple materials. This mixing of materials in cells can present difficulties in modeling material and boundary interfaces. One improvement often implemented in Eulerian codes is an additional Lagrangian step, known as “operator-split”, in which the mesh is allowed to distort and follow the material; then the solution is mapped back to the Eulerian grid (Anderson, 1987). Eulerian methods remain commonly used for impact problems due to their ability to model large deformation.

2.2.1.3. Arbitrary Lagrangian-Eulerian

The most well known extension of the Lagrangian and Eulerian methods is the Arbitrary Lagrangian-Eulerian method. Developed to combine advantages and minimize limitations of Lagrangian and Eulerian methods, ALE maps the solution to a dynamic mesh independent of material motions or spatial coordinates. This mesh is allowed to remain fixed like Eulerian methods, follow the material distortion like Lagrangian methods, or move arbitrarily (Donea, Huerta, Ponthot, & Rodriguez-Ferran, 2004). This flexibility enables ALE codes to capture large deformations while maintaining clear interface distinctions. Figure 2 illustrates differences in Lagrangian, Eulerian, and ALE descriptions for a simplified mesh with respect to time. The Lagrangian nodes follow exactly the motion of the material. While the Eulerian mesh stays constant in spite of material motion, the ALE mesh neither necessarily remains constant nor copies the material motion (Donea, Huerta, Ponthot, & Rodriguez-Ferran, 2004).

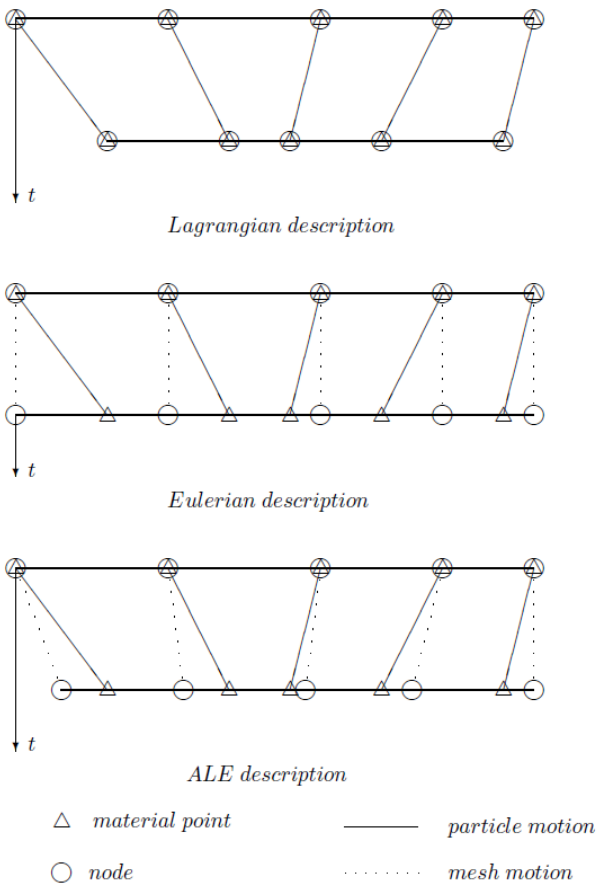

Figure 2. Comparison of Lagrangian, Eulerian, and ALE Descriptions (Donea, Huerta, Ponthot, & Rodriguez-Ferran, 2004)

A simplified implementation of the ALE method is provided in the 2006 version of LS-DYNA which allows for automatic rezoning to stabilize calculations with large deformations (Hallquist, 2006); ALE methods like this one provide second order accurate solution remapping where first order manual remapping would ordinarily be required. This ability has

garnered ALE methods much interest and use in problems of fluid and structural dynamics including situations involving impact and penetration (Donea, Huerta, Ponthot, & Rodriguez-Ferran, 2004). However, ALE codes typically involve higher computational costs per element than other methods, and these costs vary depending on remapping algorithms and whether or not the method allows more than one material per cell (Benson, 1992).

2.2.1.4. Meshless Methods

Meshless methods represent the motion of a continuous system by use of nodal points or particles without the restrictions of a mesh (Li & Liu, 2002). Many early meshless methods required background cells to be integrated over the problem domain. Examples of these are particle-in-cell methods which combine Eulerian and Lagrangian methods (Belytschko, Krongauz, Organ, Fleming, & Krysl, 1996). The Fluid Implicit Particle method (FLIP), a particle-in-cell scheme, solves the governing equations on an Eulerian grid, maps the solution to Lagrangian material particles which move and carry history dependent material properties, and then maps the particle values back to the Eulerian grid for the ensuing time step (York, 1997). Alternatively, within the last 15 years “truly” meshless methods that require no background mesh have been developed such as the Meshless Local Petrov-Galerkin (MLPG) method (Lin & Atluri, 2001). Constructing approximations in terms of nodes, truly meshless methods solve problems difficult to solve in mesh-based methods. Meshless methods contain

great potential to model history dependent materials in problems with large distortions without highly distorted meshing or difficulties of material boundaries and cell mixing.

2.2.1.5. Kinematic Description Summary

Lagrangian methods have been popular for structural mechanics problems, especially in static problems. However, with increased material interaction the Lagrangian point of reference can become highly distorted and unstable. Eulerian methods have been more common in the field of fluid dynamics, but face difficulties in material interface descriptions in structural problems. ALE methods are coupled Lagrangian and Eulerian methods that have shown improved modeling, but incur higher computational costs. Meshless methods represent efforts to move from the limitations associated with all meshed techniques; these methods are still early in development but show promise. While each of these kinematic description methods has potential areas of difficulty, all present capable means of modeling impact and penetration problems.

2.2.2. Discretization Methods

Discretization is a means of approximating a full system by use of a finite number of connecting individual parts. Discretizing systems were originally developed by both mathematicians and engineers; each used a different method for solving the governing equations about the discrete model. Mathematicians developed differencing techniques to

approximate the governing differential equations while engineers created relations between actual discrete elements and finite sections of a continuum domain. These methods of discretization have been developed simultaneously and interdependently. (Zienkiewicz, 1979)

Finite difference and finite element methods now represent two popular numerical approximations used to model partial differential equations involved in continuum problems (Anderson, 1987). The major difference between most finite element and finite difference programs used in impact and penetration applications is the method used to calculate accelerations and their associated forces, while the equations to update the stresses, energy, and shock viscosity are equivalent (Benson, 1992). In implementation, finite element methods employ segmented ordinary polynomial equations to approximate partial differential equations where finite difference codes employ differencing equations.

2.2.2.1. Finite Element Method

The Finite Element Method (FEM) is a numerical technique that provides approximations of partial differential equations. FEM approximates a fully continuous solution by a piecewise continuous field of finite elements (Anderson, 1987). The value for the field quantity (and possibly its derivatives) is solved by an interpolation scheme within each discrete element. Many interpolation schemes exist in FEM, most of which are polynomial based (Cook, Malkus, Plesha, & Witt, 2002). As an example of one-dimensional polynomial

interpolation schemes, consider "Lagrange's interpolation formula" shown in Figure 3; where N_i is the shape function corresponding to the node at x_i for n number of nodes along the coordinate x. The figure shows linear (a) and quadratic (b) interpolation regarding the field variable ϕ. FEM applications can provide convergent solutions in analysis programs and are commonly used in many types structural mechanics applications. (Cook, Malkus, Plesha, & Witt, 2002)

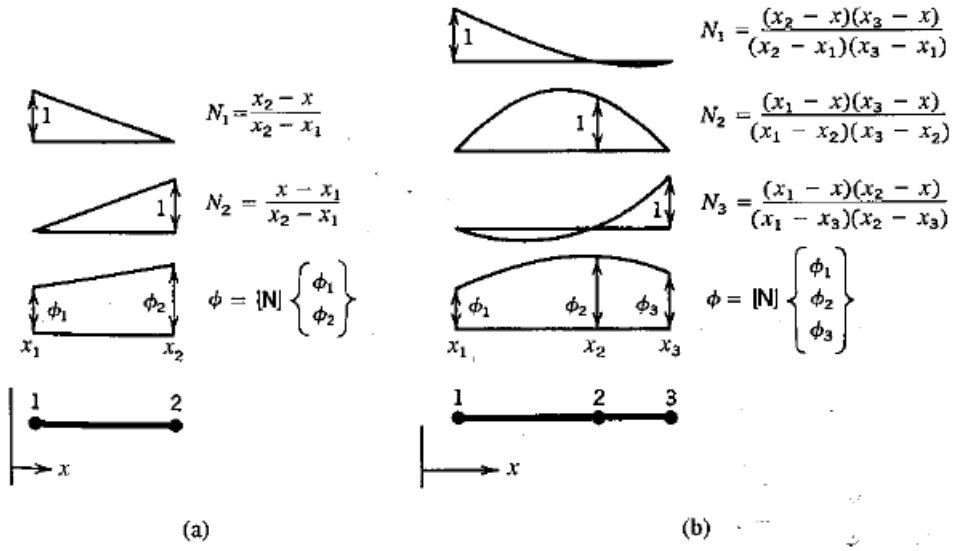

Figure 3. Lagrange Interpolation and Shape Functions: a) Linear, b) Quadratic (Cook, Malkus, Plesha, & Witt, 2002)

2.2.2.1.1. Element Type

Within finite element codes, element types are separated by available degrees of freedom and form of the shape function. This can have significant affects on the analysis. Different

FEM programs offer a number of elements to choose from, but avaiablilities differ between codes. To illustrate the importance of element type selection, consider two common two-dimensional elements that meet commonly accepted FEM robustness requirements: the linear, constant strain triangle (CST) and the bilinear quadrilateral (Q4). Because of the linear deformation and resulting constant strains across the element, the CST exhibits slow convergence, spurious shear, and excessive stiffness in bending and even demonstrates erroneous locking in plane strain conditions (Cook, Malkus, Plesha, & Witt, 2002). The Q4 is unable to model pure shear because it experiences shear locking behavior due to parasitic shear (Cook, Malkus, Plesha, & Witt, 2002). While both the CST and Q4 meet the fundamental robustness requirements of continuity, compatablity, and completeness, both exhibit inherent inaccuracies.

In current three-dimensional FEM programs, tetrahedral and hexahedron (brick) elements are commonly used. Johnson et al. (2006) recommend using tetrahedral elements in a symmetric arrangement in the EPIC 2006 program. The tetrahedral elements employ weighted residual formulations involving volumetric strain to resist volumetric locking and preserve reasonable timesteps; there has been work to validate their use in high velocity impact problems demonstrating high distortion (Beissel & Johnson, 2000). The LS-DYNA theory manual recommends the use of the eight-node hexahedron with one-point Gaussian quadrature due to significant cost savings and avoidance of locking response in bending

modes (Hallquist, 2006); however, potential hourglassing modes may occur that must be prevented by viscous damping or the recommended elastic stiffness method. Figure 4 and Figure 5 show typical tetrahedral and hexahedron elements.

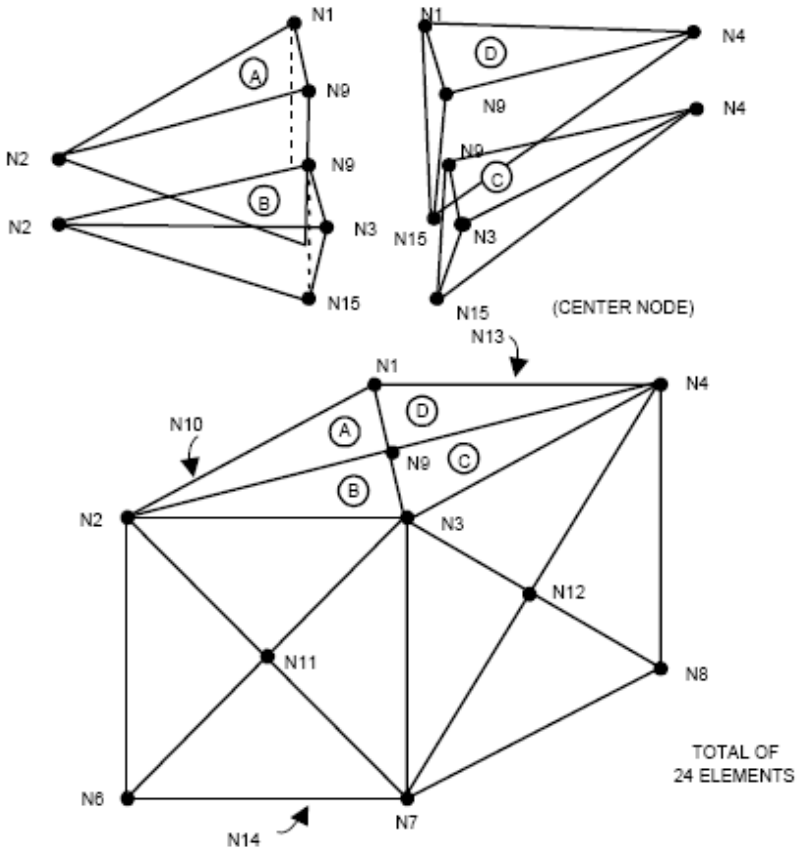

Figure 4. Symmetric Tetrahedral Arrangement (Johnson, et al., 2006)

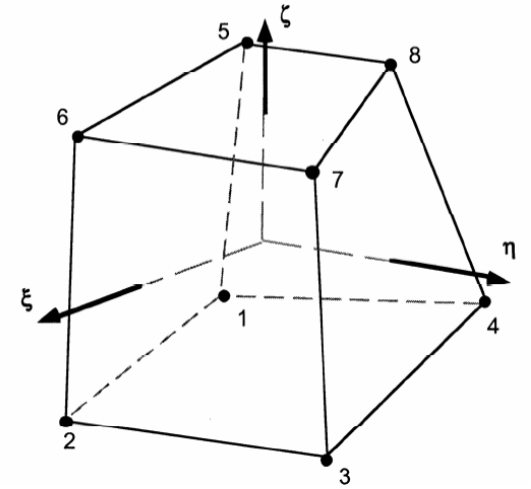

Figure 5. Eight-node Solid Hexahedron Element (Hallquist, 2006)

Elements used in FEM analyses range in complexity and efficiency. The most effective element may depend on the particular application or FEM code. The CST and Q4 two-dimensional elements serve as an illustration that elements common to finite element codes must be cautiously selected in order to avoid discretization error.Whatever the application or analysis code, much attention should be paid to the choice of element type to avoid erroneous results.

2.2.2.2. Finite Difference Method

The Finite Difference Method (FDM) uses a system of discrete points to form a grid that approximates an exact solution for partial differential equations (Anderson, 1987). The values computed at the points represent the system for some discrete space. Numerous

differencing equations are employed to replace the partial derivatives in differential equations inherent with continuum solutions. Forward, backward, and central difference equations are examples of FDM approximations for the derivatives of a continuous function. FDM represents the differential equation solution with pointwise descriptions of the discrete system that exhibit minimal computational cost and are typically easier to implement than FEM algorithms. Despite offering less accuracy than FEM, the ease and efficiency of FDM approximations have made them popular in applications of computational fluid dynamics where problems can involve discretizations on the order of a million or more grid cells. (Smith, 1985)

2.2.2.3. Discretization Summary

FEM and FDM represent two prominent discretization techniques currently used. The differences between the two approaches have reduced significantly over years of development. Johnson has been quoted by Anderson in a definitive summary of the two methods: “Finite difference techniques are an approximate solution of an exact problem, finite element techniques are an exact solution of an approximate problem” (1987). In most current applications, the techniques can be generalized as providing different algorithms resulting in comparable solutions to the same differential equation (Anderson, 1987). The accuracy of an FDM analysis is dependent upon the differencing technique implemented, while FEM solutions rely on the selected element type and corresponding shape functions. It

has been shown that in solid dynamic problem sizes where it remains computationally effective, FEM analyses provide more robust solutions (Cook, Malkus, Plesha, & Witt, 2002).

2.3. Constitutive Models

Numerical methods require constitutive relationships that describe the physical response of each of the materials involved in the analysis. Constitutive models vary in complexity and require laboratory testing for material property data (Babu, Benipal, & Singh, 2005). Material models used in impact and penetration analysis must describe physical observations of material response. Inaccuracies with constitutive models largely limit numerical methods and deserve greater attention especially when considering impact at ordinance velocities where the material strengths dominate the response (Jonas & Zukas, 1978).

Impact problems involving composite brittle materials such as concrete require especially close attention as the material responses are complex. The unique behaviors exhibited by concrete include nonlinear stress-strain response, variation in tensile and compressive strength, ductility with confinement, limited shear dilation in compression, strain softening, and stiffness degradation with cyclic loading (Chen & Han, 1988). In addition, the concrete penetration problem introduces the effects of high strain-rates, high pressures, and fracture or damage accumulation (Cargile D. , 1998).

Concrete constitutive models for numerical methods have improved in the last 40 years based upon the ability to capture accurate material response from experiments (Babu, Benipal, & Singh, 2005). Material models for concrete have historically been classified into numerous approaches including elasticity, plasticity, and inelasticity theories. More recently fracturing, continuum damage, and microplane models have appeared in the literature. Two common categories of concrete modeling are plasticity models and continuum damage models. While plasticity models do not form the majority of current material relations used for brittle geomaterials, they represent a large portion of previous literature in constitutive modeling and form a basis for material models used currently. Continuum damage models represent a larger portion of concrete material models used in current numerical methods.

2.3.1. Plasticity Models

The theory of plasticity was developed by extending the mathematical theory of elasticity beyond yield. After much foundational work by Tresca and others, von Mises developed the first pressure-insensitive yield criterion in 1913. Prandtl and Melan later contributed to the theory with the development of hardening relationships for materials (Chen & Han, 1988). While classical plasticity models contain only a yield criterion, modern plasticity models are additionally characterized by their flow rule and hardening rule. The von Mises and Drucker-Prager are two fundamental plasticity yield criteria. While they are found in some current analysis program libraries, they are discussed below to provide a background to the strength

relation of more recent continuum damage models. The Osborn model will also be discussed though it would not be defined as a classical plasticity model. However, it does represent a connection of current continuum damage models with the theory of plasticity.

2.3.1.1. von Mises

The von Mises yield criterion is one of the earliest pressure independent plasticity models. The yield criterion or yield function, *f*, is defined by a critical yield stress, σ_y, and the second invariant of the deviatoric stress tensor, J_2, which is defined by the stresses in the principle directions, σ_1, σ_2, and σ_3:

$$f(J_2) = J_2 + \sigma_y^2 = 0 \qquad \textbf{Equation 2.1}$$

$$\text{where } J_2 = \frac{1}{6}\left[(\sigma_1 - \sigma_2)^2 + (\sigma_2 - \sigma_3)^2 + (\sigma_3 - \sigma_1)^2\right] \qquad \textbf{Equation 2.2}$$

It is helpful to note that, in the plasticity models and continuum damage models discussed here, strength is defined as an equivalent stress, σ_{eq}, or von Mises stress ($\sqrt{3J_2}$):

$$\sigma_{eq} = \left[\frac{1}{2}(\sigma_1 - \sigma_2)^2 + \frac{1}{2}(\sigma_2 - \sigma_3)^2 + \frac{1}{2}(\sigma_3 - \sigma_1)^2\right]^{1/2} \qquad \textbf{Equation 2.3}$$

This equivalent stress can also be described as shear strength or principle stress difference, τ, in terms of axial stress ($\sigma_a = \sigma_1$) and radial stress ($\sigma_r = \sigma_2 = \sigma_3$) of a concrete cylinder under axial compression with or without confinement (Hanchak, Forrestal, Young, & Ehrgott, 1992):

$$\tau = \sigma_a - \sigma_r \quad \text{and} \quad \sigma_{eq} = \tau \qquad \textbf{Equation 2.4}$$

The yield function, interpreted visually as a failure surface, can be defined as an elastic limit of the equivalent stress. The von Mises yield criterion laid the foundation for future concrete plasticity models; however it was developed and designed for materials whose strength was unaffected by confining pressure. This has not been found true for concrete (Ashby & Hallam, 1986; Joy & Moxley, 1993; Cargile D. , 1998), therefore von Mises is inadequate for concrete modeling.

2.3.1.2. Drucker-Prager

Drucker-Prager is a two-parameter plasticity yield criterion that represents a pressure dependent extension the von Mises yield criterion (Chen & Han, 1988). The Drucker-Prager function includes the first invariant of the stress tensor, referred to as I_1:

$$I_1 = \sigma_1 + \sigma_2 + \sigma_3 \qquad \textbf{Equation 2.5}$$

which allows for the influence of pressure on the strength of the material. The influence of pressure is important and can be observed in concrete testing; the addition of pressure by confinement in an axial compression test results in greater observed strengths.

The Drucker-Prager yield criterion takes the form:

$$f(I_1, J_2) = \alpha I_1 + \sqrt{J_2} - k = 0, \qquad \textbf{Equation 2.6}$$

where α and k are arbitrary material constants. A possible definition for the α and k constants involves internal angle of friction φ and compressive and tensile first yield strengths, f'c and f't (Lopez-Cela, 2002):

$$\alpha = \frac{6\sin\varphi}{\sqrt{3}(3\pm\sin\varphi)} \quad \text{and} \quad k = \frac{3\sqrt{f'cf't}\cos\varphi}{\sqrt{3}(3\pm\sin\varphi)} \qquad \textbf{Equation 2.7}$$

$$\text{where} \quad \varphi = \sin^{-1}\frac{f'c-f't}{f'c+f't} \qquad \textbf{Equation 2.8}$$

The internal angle of friction was originally developed in the Mohr-Coulomb plasticity criterion, and the " $\pm$ " in the α and k equations describes whether the Drucker-Prager function circumscribes (compressive meridians) or is inscribed by (tensile meridians) the Mohr-Coulomb function (Lopez-Cela, 2002). In three-dimensional stress space the failure surface appears conical for Drucker-Prager as compared to the cylindrical von Mises yield surface, both centered about the axis of hydrostatic compression. Figure 6 compares the two models in the meridian plane (a, c) and deviatoric plane (b, d). (Chen & Han, 1988)

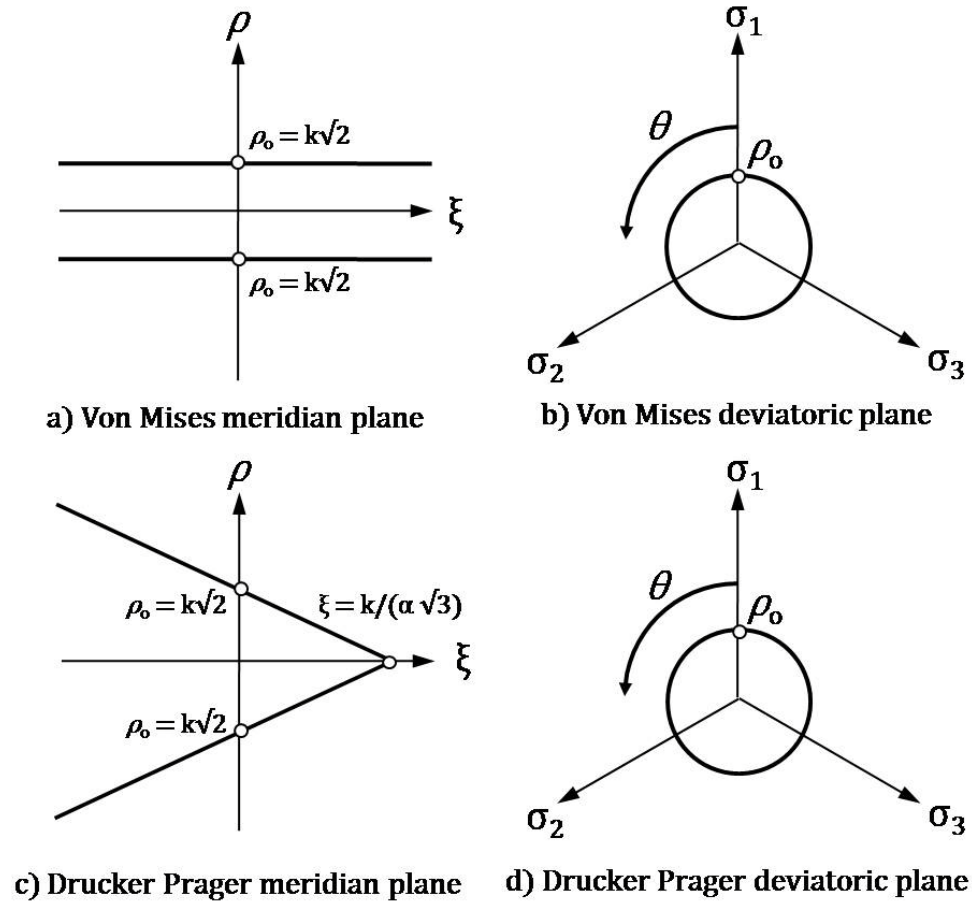

Figure 6. von Mises and Drucker-Prager Yield Surface

The meridian plane represents a comparison of a quantity of deviatoric stress, ρ, to a quantity of hydrostatic stress, ξ; these terms are expressed:

$$\rho = \sqrt{2J_2} \quad \text{and} \quad \xi = I_1/\sqrt{3} \qquad \textbf{Equation 2.9}$$

The angle of similarity, θ, represents differences between compressive and tensile meridians. Implementation of the Drucker-Prager model requires a hardening rule and a flow rule to define plastic deformation. Hardening rules require that material constants, α and k, be variable functions of a hardening parameter which is often defined by a hardening modulus applied to the elastic-plastic equations. Commonly, the flow rule is formed by replacing the parameter α with a material dilatancy constant, β. If β is greater than 0, plastic deformation will result in volume increase. If β is equal to α, the flow rule is said to be associative which assumes the material is elastic-perfectly plastic; this is not commonly assumed for concrete, and terms for β range between zero and α (Loret & Prevost, 1986).

Of the plasticity models, Drucker-Prager is one of the more basic pressure dependent models with constants that are easily determined from compression and tension tests. While Drucker-Prager has been frequently used for modeling soils in the past, the model exhibits deficiencies in modeling concrete because it includes a simple linear relationship between ρ and ξ, as well as no effect by the angle of similarity, θ, resulting in undesired similarity between compressive and tensile meridians (Chen & Han, 1988). As do the majority of plasticity models, the Drucker-Prager model omits the effects of strain rate and damage accumulation. Extensions of the model have been made to improve the linear relationship between ρ and ξ (Bresler & Pister, 1958), as well as add the effects of the similarity angle (William & Warnke, 1974; Ottosen, 1977). While these improved extensions exhibit more

accurate concrete modeling; in current literature, Drucker-Prager is only an adequate concrete representation in limited loading cases where materials remain in the elastic range (Loret & Prevost, 1986; Lopez-Cela, 2002).

2.3.1.3. Osborn (Hull)

The Osborn concrete model originated from an earlier, simpler model in the Hull program. The original model was only recommended for low pressures (below 100 MPa), and based on a small amount of static test data (Matuska, Durret, & Osborn, 1982). The newer Osborn model was improved and included in the EPIC analysis code. The model is summarized by two relations shown in Figure 7: strength and pressure, or, more clearly, strength versus pressure and pressure versus volumetric strain, often referred to as an equation of state.

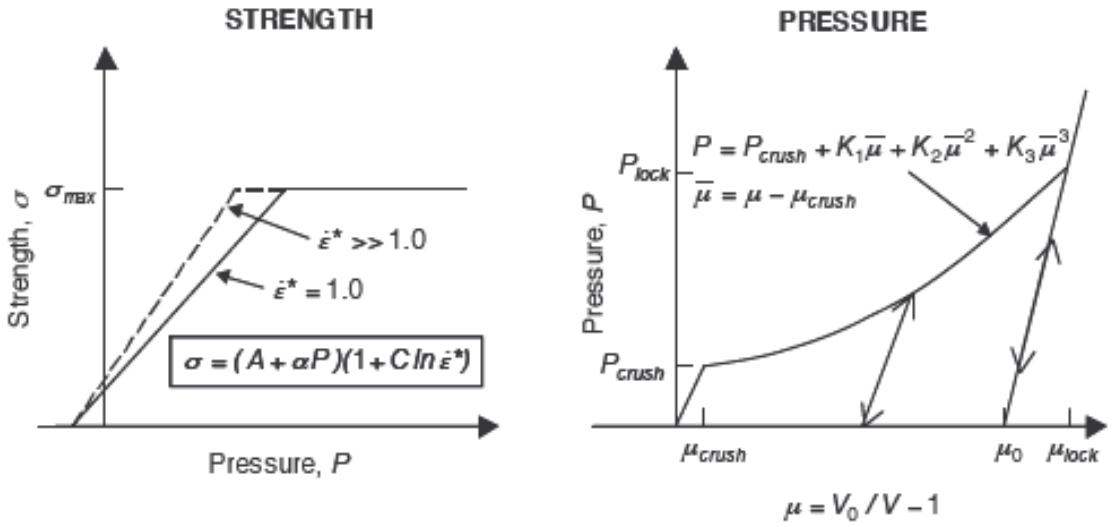

Figure 7. Osborn Model a) Strength b) Pressure (Johnson, et al., 2006)

The strength, σ, is defined as the equivalent stress or shear strength and is shown in Figure 7 a). The pressure, *P*, is defined as the average of the three principle stresses. Both strength and pressure are defined as positive in compression. The pressure axis in the strength model is similar to the hydrostatic compression axis in the Drucker-Prager model. The effect of strain rate is included by a strain rate constant, C, applied to the natural log of the strain rate ratio, $\dot{\varepsilon}^*$. The term $\dot{\varepsilon}^*$ is equal to the actual strain rate divided by a reference strain rate which was used to find the material constants. Strain rate effect is a critical consideration in sub-millisecond loading conditions like those present in high velocity concrete penetration events.

Literature Review

The equation of state, or pressure model, is used to characterize the high pressure, impulsive loading present in high velocity impact (Cargile D. , 1998). Volumetric strain, μ, is a representation of the multi-dimensional deformation of the concrete and is defined in terms of relative volume, V_0/V, as shown in Figure 7 b). The equation of state is defined in three sections: elastic (prior to the crushing point), crushing (between the crushing and locking points), and locking (where all voids are assumed removed). These sections rely on the definitions of the curve fitting constants, K_1, K_2, and K_3, as well as the crushing point (defined by P_{crush} and μ_{crush}) and locking point (defined by P_{lock} and μ_{lock}).

The Osborn model decouples the deviatoric and volumetric responses and requires specification of twelve material constants, usually obtained by material testing. Required material testing would include multiple triaxial compression tests with varying confining pressures to define the strength curve, and the equation of state definition would require a hydrostatic compression test and shock Hugoniot testing for higher pressures. Hugoniot is the description of material states obtainable through a single shock wave loading. The strength portion of the model is similar to the Drucker-Prager model with a linear strength-pressure relationship based on constants A and α; however it also utilizes a strength limit, σ_{max}, independent of pressure, similar to that of von Mises (Johnson, et al., 2006). The shortcomings of the Osborn model include the linear relationship between strength and pressure which has been shown to be curved from experimental data and no distinction between tensile and compressive meridians. While the Osborn model does include the effects

of strain rate on the concrete strength, it neglects the accumulation of damage. Validation work for this concrete model is limited and difficult to access. The Osborn concrete model represents an extension of plasticity theory towards decoupled deviatoric and volumetric response; and while validation of the model is scarce, it does present potential advances in concrete modeling.

2.3.2. Continuum Damage Models

While plasticity theory models have been implemented with a level of accuracy in the past, they are highly dependent on the assumption of a well defined yield surface which can be difficult to specify in concretes. Concrete response beyond the elastic limits is based largely on the growth and spread of microcracks (Cargile D. , 1998), and recent work has been devoted to the incorporation of cumulative damage on the strength of brittle geomaterials (Babu, Benipal, & Singh, 2005). Continuum damage models use a set of state variables to quantify the amount of internal damage sustained as a result of a specific loading history. The use of the damage variables assumes that local damage can be averaged in the material and applied to the stiffness and/or strength of the concrete. Babu states that continuum damage models typically either extend from plasticity models or employ thermodynamic fundamentals and energy balance (2005). Continuum damage models currently represent a large portion of popular concrete constitutive models, and a representative sample is discussed below.

2.3.2.1. Holmquist Johnson Cook Concrete (HJC)

As an expansion of the Osborn model, the HJC model contains a strength relation and equation of state similar Osborn; however, HJC introduces features to better model concrete penetration by considering large strains, high strain rates and high pressures (Holmquist, Johnson, & Cook, 1993). Among these improvements, HJC incorporates the effects of cumulative damage and complete crushing of concrete at high pressures (Figure 8).

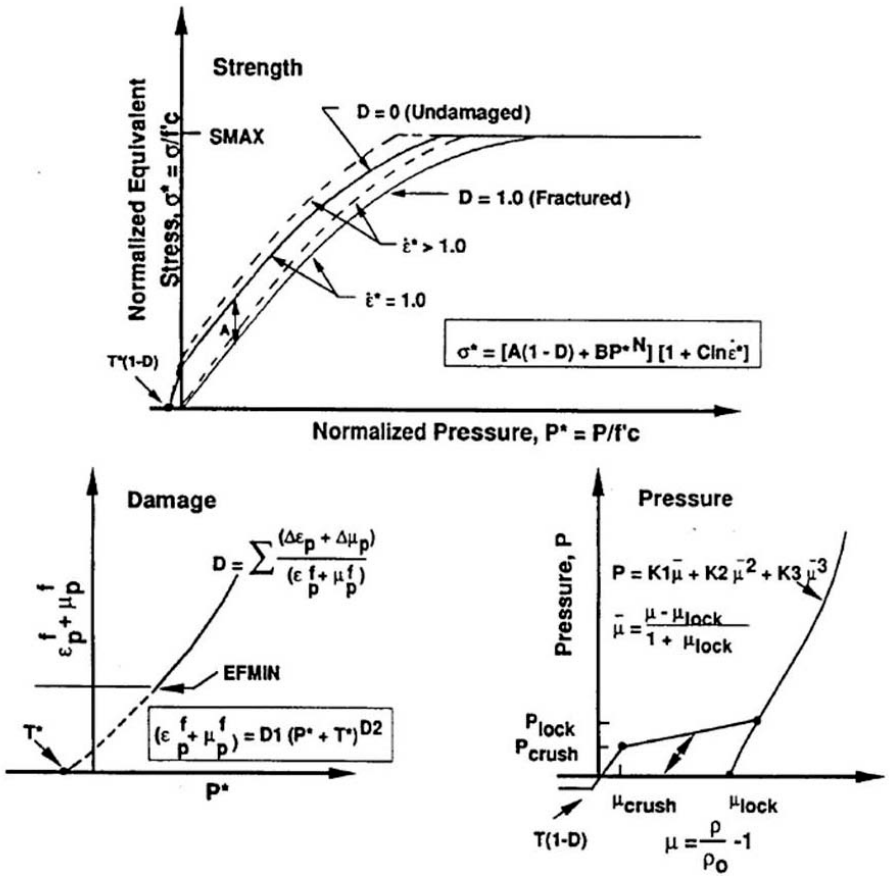

Figure 8. HJC Model (Holmquist, Johnson, & Cook, 1993)

The strength portion of the model is nonlinear and defined by normalized equivalent stress, σ*, versus normalized pressure, P*, both normalized by the unconfined compressive strength, f'c. A damage parameter, D, is applied to the cohesive strength constant, A, which represents the difference between undamaged and fractured strength. Other strength constants include the normalized pressure hardening coefficient and exponent, B and N, respectively, as well as the strain rate constant, C, and the normalized maximum strength, SMAX. The tensile portion of the strength curve is determined by a normalized tensile strength constant, T*, with damage applied.

The equation of state contains the three regions as described in the Osborn model: elastic, crushing, and locking. The three regions are segmented by the crushing and locking points. In HJC, the crushing region is considered linear and the locking portion is a normalized polynomial. The curve also contains a triaxial tension region based on the direct tension constant, T, with damage applied. As an alternative to modifying all the constants to fit the curve to hydrostatic compression test data, formulas are given for all of the constants in the equation of state except for T, P_{lock}, K_1, K_2, and K_3 which are used to fit the model to data.

The HJC model includes a damage model to calculate the value, between zero and one, of a damage variable, D, which is applied to the strength and equation of state. D is calculated by the proportion of the summation of equivalent and volumetric plastic strains to a failure strain surface defined by the solid line curve in the damage portion of Figure 8. This damage failure surface represents the point at which pressure and plastic strains result in damage

equal to one. Notice that as pressure increases more plastic strain is required to reach a damage value of one. This description of damage considers a behavior that can be seen in triaxial compression tests; with higher confining pressures the strain at failure increases. The damage model contains material constants T*, D_1, D_2, and EFMIN which are selected as the values recommended in the original work. (Holmquist, Johnson, & Cook, 1993)

As an extension of the Osborn model, HJC introduces additional capacity to represent concrete response and requires additional work to implement the model for a specific concrete. The HJC model contains a large number of material constants compared to simpler plasticity models; however, for many of these constants suggested formulas are given or recommended values are provided to ease implementation. Numerous material tests are required to completely define the constants for a particular concrete specimen. The strength model requires an unconfined compression test, a direct-pull test, a series of triaxial compressive tests, and a series of compressive tests at different strain rates. The equation of state requires a hydrostatic compression test and Hugoniot data for aggregate. The damage model requires a cyclic unconfined compression test. While the strength is modeled by a nonlinear curve; the HJC model, like Osborn, does not distinguish between compressive and tensile meridians along the pressure axis. While inclusion of the strain rate effects is an important feature of HJC, two aspects of concrete strain rate effects are neglected. It has been shown in literature that the strain rate enhancement curve is different in tension than in compression, and both enhancement curves are bilinear on a logarithmic scale (Bischoff &

Perry, 1986; Hughes, Tedesco, & Ross, 1993; Ross, Kuennen, & Tedesco, 1992). While the introduction of cumulative damage provides a promising link between elastic and completely crushed concrete, the model representation of damage is limited. For example, triaxial test data shows the strength difference between undamaged and fractured concrete is reduced as confinement levels are increased; this indicates that the cohesive strength constant, A, should be variable, influenced by pressure. Similarly, the damage constant, D_2, which can show lower damage accumulation with higher pressures is commonly assigned a value of one following the work of Holmquist et al. (1993); this implies that failure strain and pressure are directly proportional. Triaxial test data from other literature has not supported this theory (Ashby & Hallam, 1986; Joy & Moxley, 1993; Cargile D. , 1998). Much HJC validation work has focused on the perforation of concrete. The model has shown adequate results for reinforced concrete (Holmquist, Johnson, & Cook, 1993; Tai & Tang, 2006), but other sources have highlighted the existance of deficiencies at high velocities (Dawson, Bless, Levinson, Pedersen, & Satapathy, 2008). Wang et al. found HJC to be inadequate for modeling tensile fracture and spallation craters (2007). Polanco-Loria et al. made modifications to the model and found improvements to resultant velocity predictions for perforation of concrete slabs (2008). While the HJC model contains areas of weakness, it does make efforts to represent complex concrete response with the inclusion of strain rate and damage effects.

2.3.2.2. Brittle Failure Kinetics (BFK)

The Brittle Failure Kinetics model was developed to represent concrete response in problems involving penetration and large stress waves. The model is based on rate effects applied through a time dependent damage variable. BFK employs Mohr-Coulomb failure curves to describe strength and an equation of state to relate pressure and density. The model seperates itself from other rate dependent concrete models in that strain rate is not explicitly included, but treated by a delay time, 'time to failure' (Silling, 1997).

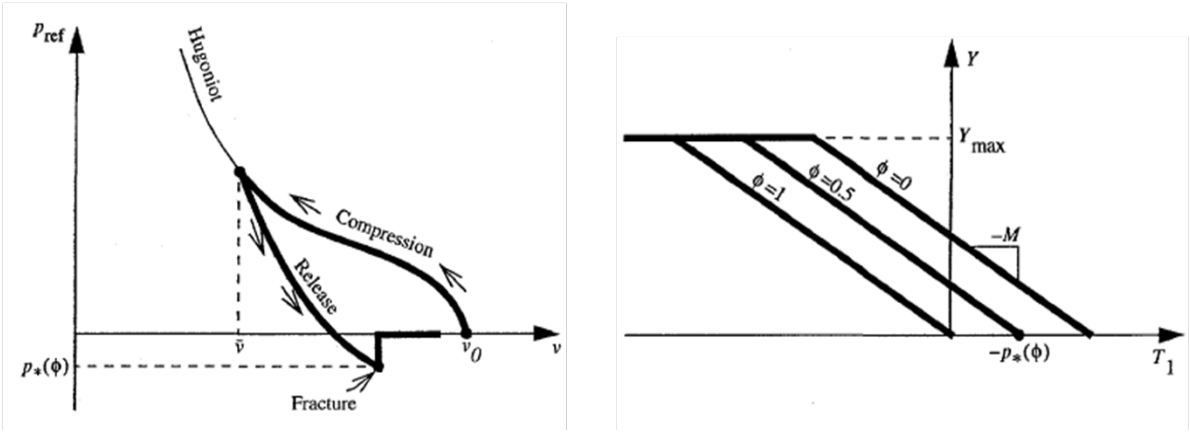

Figure 9. BFK: a) Equation of State, b) Strength (Silling, 1997)

The strength model is used to define the yield strength in a manner similar to that used in plasticity theory. Mohr-Coulomb strength surfaces and a scalar damage parameter, ϕ, are used to find an interpolated failure surface. Figure 9 b) depicts the strength model. The

strength curves are shown as straight lines on the plane of yield strength, Y, versus maximum negative principal stress, T_1, positive in tension. The equation of state for the BFK model is defined by pressure and internal energy density reference curves (Silling, 1997). The pressure reference curve (compression) is fit to shock Hugoniot data by specific volume, *v*, and pressure, *p*, value pairs. The model distinguishes between loading and unloading due to the nature of void compression in concrete by the inclusion of a separate release curve as shown in Figure 9 a). The BFK damage variable, ϕ, is defined by the summation of brittle, ductile, and compressive damage rates and is dependent upon rate and geometry. Figure 10 shows the difference between an ideal strength surface and a typical triaxial failure envelope. The failure envelope does not follow the strength surfaces because the envelope includes damaged states. A separate failure surface exists for each value of ϕ between zero and one. To help describe the rate dependent response, Silling defined Ω as the 'overload', shown in the figure as the horizontal distance reached by the stress state beyond the failure envelope (Silling, 1997).

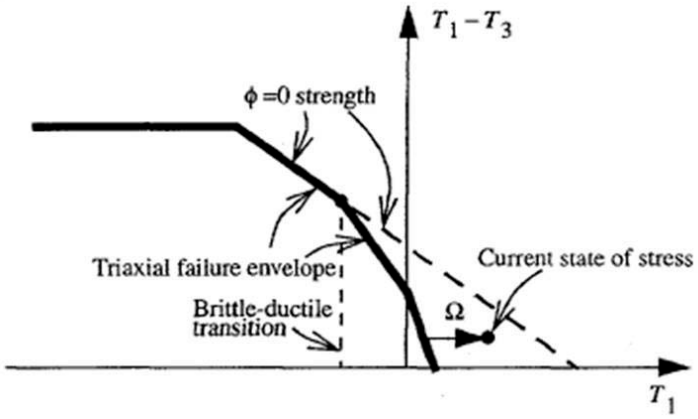

Figure 10. BFK Damage: Triaxial Failure Envelope (Silling, 1997)

The BFK model presents an alternative method for incorporation of rate dependent damage in concrete modeling. BFK provides the capacity of accurately modeling concrete with the cost of more rigorous implementation requirements for specific modeling. Unlike HJC, implementing the model for a specific concrete specimen is not described. Certain testing requirements are implied and means of proportioning data to previously implemented materials are given. The strength model would require compressive testing with multiple confinement levels and tensile testing to determine the curve intercepts with the T_1 axis. The equation of state constants can be determined with the use of Hugoniot shock tests for high pressures and quasi-static triaxial testing for low pressures. The BFK strength model uses maximum negative principal stress instead of pressure to relate stresses which recognizes that tensile strength of concrete is not significantly increased by large compressive confinement.

The representation of damage in terms of rate is a potentially useful method in modeling observed responses of concrete under impulse loads over short durations, specifically like those characteristic of concrete impact. Silling performed initial validation analyses for concrete penetration using BFK (1997) and found the model to perform well when inspecting impact velocity (400 to 1000 m/s) and penetration depth (30 to 1100 cm). The model also exhibited accurate modeling of decelerations of the projectiles perforating concrete. However, the BFK model has shown deficiencies with regard to spalling and late-time damage in concrete perforation simulations involving impact velocities on the order of two km/s (Dawson, Bless, Levinson, Pedersen, & Satapathy, 2008). The BFK model provides a promising means of modeling complicated concrete response with alternative methods for considering the strength relation, strain rate effects, and damage.

2.3.2.3. Karagozian & Case (K&C)

The K&C model was created to effectively and realistically model concrete through the use of the strength model, damage parameter, and user-defined equation of state (Malvar & Simons, 1996). In addition, the model incorporates features to better describe shear dilation, strain rate effects, and differences in compressive and tensile strength meridians with regards to concrete.

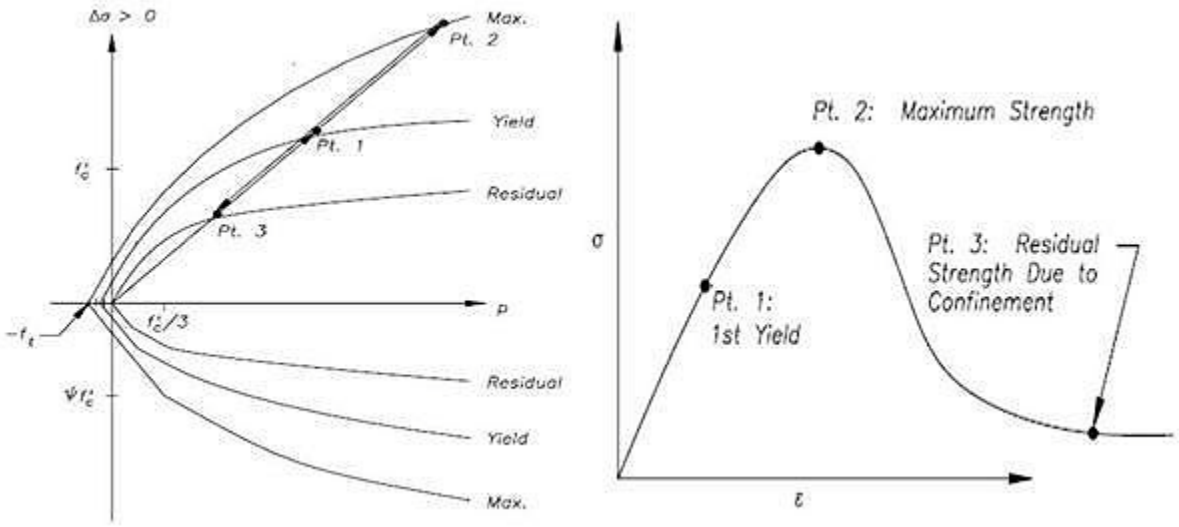

Figure 11. K&C Strength Model a) Strength vs. Pressure, b) Typical Stress-Strain Curve (Malvar & Simons, 1996)

The two major features in this strength model are the distinction between the yield, maximum, and residual failure surfaces and the inclusion of the third invariant of the deviatoric stress tensor, J_3, which is proportional to the similarity angle, θ. The strength failure surface is characterized by three curves (Figure 11 a) and corresponding points seen in the stress-strain curve (Figure 11 b); three points allow for a more thorough description of the hardening and softening behavior of concrete. The William and Warnke (1974) plasticity model formed the basis of the third invariant inclusion which creates the distinction between the compressive (positive Δσ) and tensile (negative Δσ) meridians in Figure 11 a). The

influence of the third invariant on the failure surface in three-dimensional stress space can also be observed in Figure 12 a).

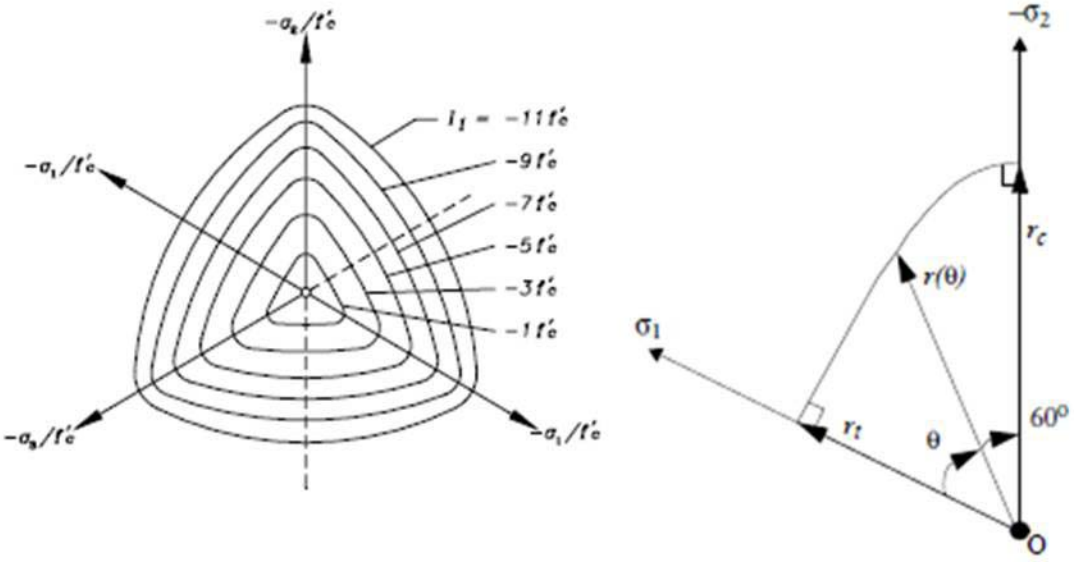

Figure 12. a) Deviatoric Sections of the K&C Failure Surface (Malvar & Simons, 1996), b) William and Warnke Model (Noble, Kokko, Darnell, Dunn, Hagler, & Leininger, 2005)

The intricate three invariant surface requires that the three failure surfaces be fit to concrete material tests using eight material constants determined by triaxial compression data. A direct tensile strength is required to proportion the tensile meridians of the model.

The K&C model includes shear and volumetric damage. The shear damage parameter of the model, λ, involves strain rate enhancement (r_f), pressure (p), effective plastic strain ($\overline{\varepsilon^p}$), and material constants, b_1 and b_2:

$$\lambda = \int_0^{\overline{\varepsilon^p}} \frac{d\overline{\varepsilon^p}}{r_f(1+\frac{p}{r_f f_t})^b} \quad \text{where} \quad b = \begin{cases} b_1 \; for \; p \geq 0 \\ b_2 \; for \; p < 0 \end{cases} \qquad \textbf{Equation 2.10}$$

The rate enhancement factor is a user defined parameter that can be modeled by an input table. In order to include damage in triaxial tension the volumetric damage, Δλ, must be included; it involves current volumetric strain, ε_v, volumetric yield strain, ε_{vy}, an internal scalar multiplier, k_d, material constant, b_3, and a closeness parameter, f_d, that describes how close the stress state is to triaxial tension and is based on the second invariant of the stress tensor, J_2:

$$\Delta\lambda = b_3 f_d k_d (\varepsilon_v - \varepsilon_{vy}) \qquad \textbf{Equation 2.11}$$

$$\text{where } f_d = \begin{cases} 1 - \frac{|\sqrt{3J_2}/p|}{0.1}, & for \;\; 0 \leq |\sqrt{3J_2}/p| < 0.1 \\ 0, & for \;\; |\sqrt{3J_2}/p| \geq 0.1 \end{cases} \qquad \textbf{Equation 2.12}$$

The damage variables are used by the strength model to interpolate the updated strength between the three failure surfaces of the strength model using a relation between the damage and the effective strength ratio, η, ranging from zero at yield strength to one at maximum strength and back to zero at residual strength. To implement the damage model for a concrete material the three material constants b_1, b_2, and b_3 must be determined in addition to a tabular relation between the λ and η.

The K&C model uses a limited shear dilation method to describe material deformation or flow. The method describes the flow behavior of concrete that is between associative (flow normal to failure surface) and non-associative (flow at angle θ_n, no shear dilation). Figure 13

a) illustrates the use of an associativity parameter, ω, to implement partial shear dilation of concrete caused by aggregate interlock; suggested values of ω range from 0.5-0.7 (Noble, Kokko, Darnell, Dunn, Hagler, & Leininger, 2005). Additionally, the maximum width of the concrete aggregate is required to model the material flow.

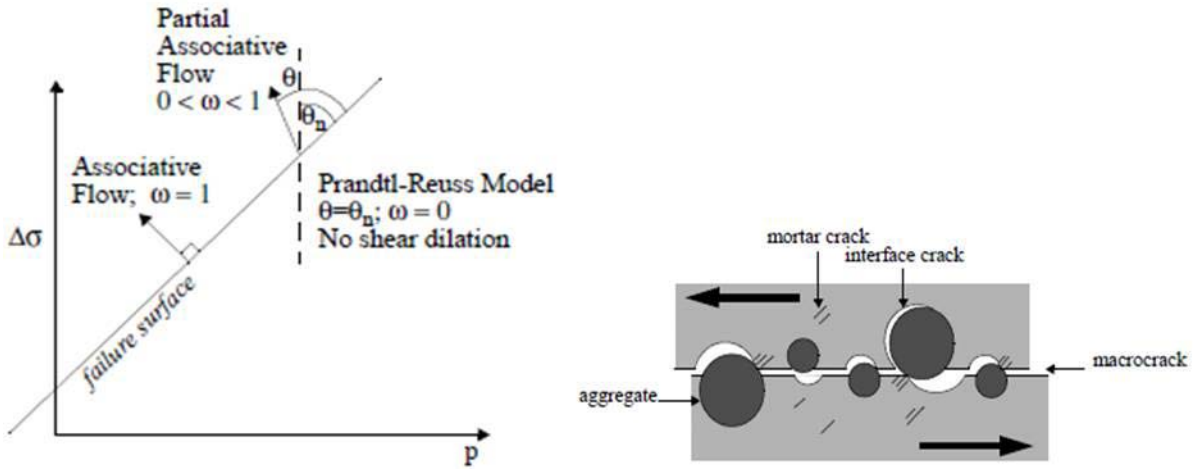

Figure 13. a) Shear Dilation of the K&C Model, b) Concrete Aggregate Interlock (Noble, Kokko, Darnell, Dunn, Hagler, & Leininger, 2005)

The K&C model shows opportunity to accurately capture concrete behavior under impact-type loading. The strength is modeled non-linearly versus pressure and varies between tensile and compressive meridians. Damage moves the effective strength between the three failure surfaces of yield, maximum, and residual in order to capture hardening and softening behavior. Damage incorporates strain rate and pressure effects. Deformation includes limited shear dilation observed in concrete under compression. The inclusion of a

user defined equation of state allows for flexibility, but may introduce unwanted user error. A drawback with the damage implementation is in the area of confining pressure; no distinction is made for stress-strain curves of different confinement levels (Yonten, Manzari, Eskandarian, & Marzougui, 2002). With the complex considerations of the K&C model, determination of material constants becomes rigorous; however, the K&C model offers a parameter-generation feature that proportions the strength and damage constants based on the density and unconfined compressive strength of concrete. This feature is available in the 2006 version of LS-DYNA and is selected by preceding the unconfined compressive strength with a negative sign in the K&C input deck (Hallquist, 2006). Initial validation analyses have shown the model to contain great potential (Malvar & Simons, 1996). An evaluation by Yonten et al. found the K&C model to effectively model the response of concrete in a typical triaxial compression test including a significantly accurate softening behavior (2002). The parameter-generation method has also been validated with success in modeling conventional concrete compression tests with only the knowledge of the unconfined compressive strength (Schwer & Malvar, 2005). The K&C model is a complicated concrete constitutive model that includes strength meridian distinction, shear dilation, and means to implement the method with limited concrete data.

2.3.2.4. Continuous Surface Cap Model (CSCM)

Cap models represent a recent development trend in continuum damage models for concrete. With the earliest work appearing in the late 1970s by Isenberg, Vaughan, and Sandler (1978), the cap model is based on the idea that continued hydrostatic loading will yield concrete material. A more recent implementation, the CSCM model, evolved from a strain sub-incrementing method by Pelessone (1989) and extended the earlier cap implementation known as the Geological Cap Model that neglected the third stress invariant, damage, and strain rate effects (Hallquist, 2006). The CSCM model was originally developed for defense purposes in the analysis of dynamic loading of reinforced concrete structures in the early 1990s under the various titles including ‘Single Surface’, ‘Smooth Cap’, and ‘Schwer-Murray’ (Schwer & Murray, 1994). More Recently the CSCM has been redeveloped to include visco-plastic formulation and additional forms of damage mechanics for use in roadside safety hardware testing (Schwer & Murray, 2002; Murray, 2007). CSCM employs a coupled deviatoric and volumetric failure surface to describe concrete yield and flow. The model considers effects of damage, strain rate and triaxial stress on the concrete strength.

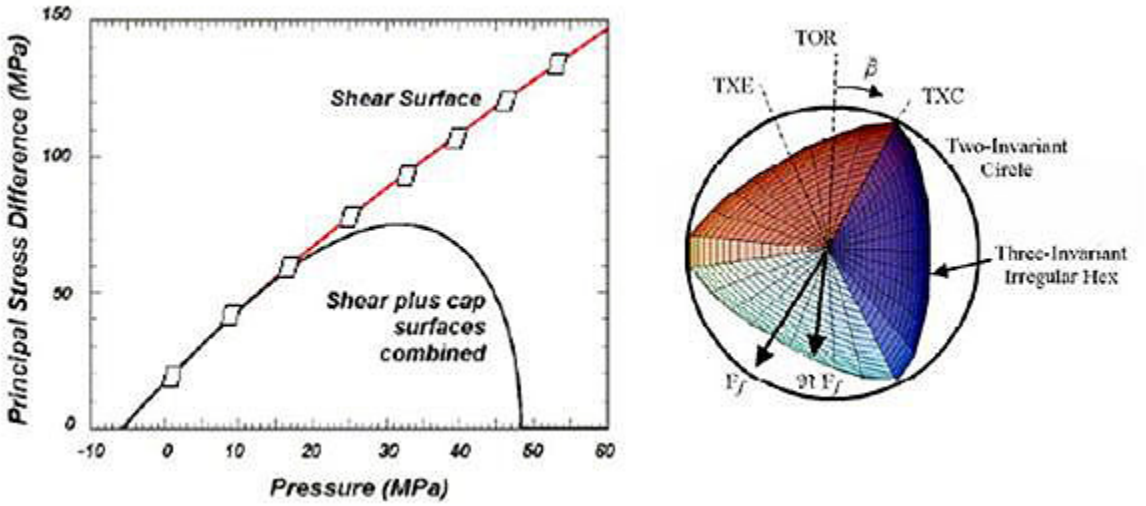

Figure 14. Typical CSCM Strength Model: a) vs. Pressure, b) Deviatoric Plane (Murray, 2007)

The CSCM strength model uses an ultimate failure surface which combines both shear failure and cap hardening (Figure 14 a). The strength model includes an ability to describe the pre-peak nonlinearity in concrete stress-strain curves involving low confinement levels. Figure 14 shows that the Rubin scaling function is incorporated in the strength model to represent the effects of the third invariant of the deviatoric stress tensor, J_3, which is directly proportional to the angle β in the deviatoric plane. The Rubin function is used to scale the material strength according to the triaxial state of stress. While other models often decouple the volumetric and deviatoric responses, CSCM incorporates the two into the failure surface through the use of the cap surface. The formulation allows for the cap to expand in plastic compaction and contract in plastic dilation. The motion of the cap is determined using the

concrete pressure-volumetric strain response or equation of state. CSCM incorporates damage applied in two forms: strain softening and modulus reduction by applying a scalar damage parameter, *d*, varying from zero to one, to the undamaged stress tensor. The effect damage has upon strain softening and modulus reduction is shown in Figure 15.

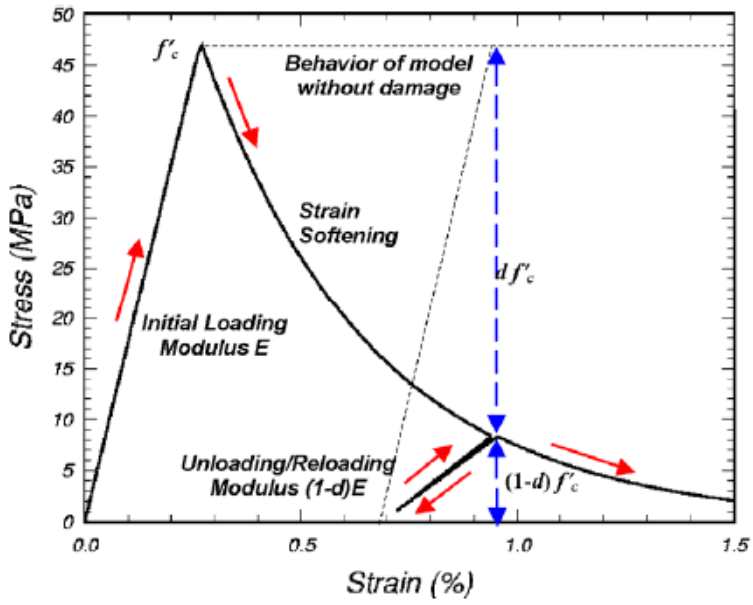

Figure 15. Example of Strain Softening and Modulus Reduction by Damage (Murray, 2007)

Damage initiates and accumulates through the use of brittle and ductile strain-based energy terms and their corresponding thresholds. The ductile damage algorithm limits the possible damage accumulation based on the amount of confining pressure, allowing more ductile behavior to be represented for concrete in higher confinement. (Murray, 2007)

CSCM involves a strength failure surface, damage accumulation, and strain rate effects. The model considers many of the responses of concrete in a range of pressure levels and triaxial stress states. Because CSCM was developed for a time sensitive application for the roadside safety community, ease of use was an important consideration for the developers. The model has up to 37 inputs parameters, with a minimum of 19 that must be fit to experimental data for the concrete. However, with the limitations of time, data, and material modeling expertise in mind, the model includes provisions for standardized material properties based only on the input specifications of the unconfined compressive strength and aggregate size. The standardized material data used to fit the parameters ranged from 2900 to 8400 psi in strength and 0.3 to 1.3 inches in aggregate size. The model underwent several validation tests as part of development including conventional cylinder testing and impact tests (Murray, Abu-Odeh, & Bligh, 2007). Cylinder test modeling has shown that CSCM can represent realistic damage modes of unconfined compression and tensile tests. The model results were comparable to test data for drop tower impact of reinforced and unreinforced concrete beams in both deflections and failure modes, and also proved successful in accurately modeling the displacement histories and damage modes of vehicle impact on reinforced concrete beams at velocities ranging from 5.3 to 20.6 mph. CSCM represents one of the most recently developed concrete constitutive models; it provides a means to model intricate material response and the capacity to do so with limited concrete data.

2.3.3. Constitutive Models Summary

Classical plasticity models represent early efforts to model the yield and flow of materials; however, in high strain rate, impulsive loading conditions these plasticity models fail to capture experimentally observed material responses. Plasticity models have been extended in many of the common continuum damage models for concrete in order to incorporate more of the complex responses of brittle materials under impulse loads extending beyond elastic limits. These continuum damage models show many improvements from the classical plasticity methods by including effects of strain rate, damage, and confining pressures. The continuum damage models can require rigorous efforts for implementation, and the selection of an appropriate material model for analysis may become a balance between experimental data availability and model capacity to capture material response.

2.4. Available Experimental Work

The response of concrete to high strain rate, impulsive loadings has been studied extensively in the last three decades. Additionally, means of conducting and monitoring experimental tests have improved with technological advances like high speed film, radar, and accelerometer acquisition systems. With increased interest and testing capabilities, increased concrete testing has been conducted, much of which can be categorized into

penetration, perforation, and detonation testing. Table 3 presents a survey of concrete case studies.

Table 3. Concrete Impulse Loading Case Studies

Author(s)	Projectile Length (in)	Projectile Mass (lb)	Impact Velocity (ft/s)	Target Type	Test Type
Forrestal et al.(2002)	20.7	28.66	459-1509	Unreinforced	Penetration
Cargile(1998)	9.54	1.98	909-2625	Unreinforced	Penetration
Cargile, Tidwell(1993)	14	5.16	801-1499	Unreinforced	Normal and Oblique Penetration
Dancygier et al.(2007)	7.83	3.31	656-1033	Reinforced	Penetration
Gold et al.(1996)	2.95-7.48	0.35-0.88	4921-6233	reinforced and unreinforced	Penetration
Unosson, Nilsson(2006)	8.86	13.89	2011-2047	reinforced and unreinforced	Penetration and Perforation
Dawson et al.(2008)	3.72	0.114	4888-7415	reinforced and unreinforced	Perforation
Averett et al.(2005)	20.77	29.19	984	unreinforced	Perforation
Hanchack et al.(1992)	5.66	1.1	984-3609	Reinforced	Perforation
Cargile et al.(1993)	14	5.16	1014-1552	Unreinforced	Perforation
Ehrgott et al.(2007)	-	C4, 4.23-8.82	-	Reinforced	Detonation
Akers et al.(2005)	-	C4, 9.92	-	Reinforced	Detonation
Akers et al.(2003)	-	C4, 9.92-13.67	-	Reinforced	Detonation
Malvar, Simons(1996)	-	Class 1.1, 272	-	Reinforced	Detonation

Penetration, perforation, and detonation testing in concrete have been of interest in the design of impact resistant structures, including hardened protective facilities, for industry and military applications. Penetration and perforation experiments assess the performance of projectiles impacting high-strength geological and structural targets. Predominantly, penetration research has considered only impact velocity and penetration depth; while perforation work has focused on residual velocity and post-test condition of the target slab.

Both fields of study have only recently begun to consider projectile erosion, deceleration, and target crater profiles. Detonation testing commonly considers only crater width and profile, and is focused on targeting and weaponeering applications. These experimental studies involving high strain rate, impulsive loading provide valuable observations of material responses that can be used to develop and validate modeling methods and material models.

2.5. Need for Research

Concrete impact and penetration is a complex phenomenon. The nature of concrete response presents particular complexities, especially under loads of highly impulsive pressures over short durations. Much work has been done to improve modeling methods of this problem, and currently there are numerous techniques and constitutive models available exhibiting promising and accurate results. The continued development of numerical analysis methods can offer an invaluable resource to study these phenomena; however, validation and verification through experimental testing is required.

Research is needed to further understand and characterize response of concrete to impact and provide data necessary to refine and validate current analysis methods. Comparison of recently developed methods and constitutive models for impact scenarios is scarce. Additionally, with recent advancements in experimental data collection for impact problems, better data is available for critical evaluation of numerical modeling techniques. Verification of common methods will provide needed reliability for scientists and engineers.

Literature Review

The current research will compare common modeling packages and constitutive models and provide a validation study for their use in concrete impact and penetration, as well as investigate a selected analysis configuration for experimental parameter sensitivity and ability to capture experimental trends.

3. Basic Problem

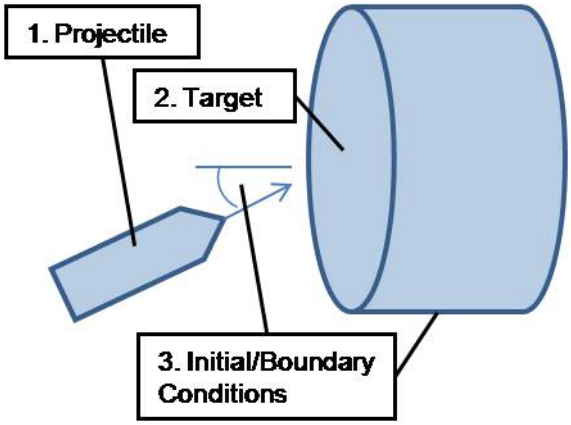

Figure 16. Experimental Setup of Impact Study

This research will compare the analytical results from multiple concrete constitutive models and analysis packages to experimental data to assess performance for concrete impact and penetration scenarios. The modeling of these problems requires understanding of 1) the material properties and geometry of the projectile, 2) the material details and dimensions of the target, and 3) the impact conditions including impact velocity, angle of inclination, and target constraints (Cargile D. , 1998). These three parts of the validation impact experiment, summarized in Figure 16, must be well understood and appropriately applied to each numerical analysis package and material model to produce an objective and creditable comparison. The necessary results must be collected from the analysis codes and a methodology for comparison applied objectively for evaluation.

3.1. Experimental Data

The experimental data selected as a means of validation in this research is a series of non-oblique concrete penetration tests performed by Sandia National Laboratories. The available documentation consists of testing reports (Frew, 2002), an instrumentation report (Rowher, Heise, & Wilder, 2001), and a final published experimental and analytical work document (Forrestal, Frew, Hickerson, & Rohwer, 2002). The test series was selected as validation due to its thorough material testing, and the availability of instrumented accelerometer data from the projectile. Table 4 displays the complete matrix of test cases from the experimental data. The series varied several experimental parameters including projectile shape, target depth, concrete strength and impact velocity. The validation also included the characterization of concrete; extensive data was collected enabling detailed fitting of the materials to available constitutive models.

Table 4. Experimental Test Matrix (Forrestal, Frew, Hickerson, & Rohwer, 2002)

Test Name	Concrete Target			Projectile				Penetration Depth
	Type	Strength (ksi)	Thickness (ft)	Nose Shape	Velocity (ft/s)	Obliquity (degrees) Pitch (Up/Down)	Yaw (Left/Right)	(in)
SNL-00-11	Conv. Str.	5.7	4	3.0 CRH	781	0.1D	0.0	11.8
SNL-00-12	Conv. Str.	5.7	6	3.0 CRH	904	0.1D	0.4L	15.0
SNL-00-09	Conv. Str.	5.7	4	3.0 CRH	1030	0.2D	0.2R	17.7
SNL-00-10	Conv. Str.	5.7	4	3.0 CRH	1212	3.6U	2.5L	20.9
SNL-00-14	Conv. Str.	5.7	6	3.0 CRH	1497	0.2U	0.2R	37.0
SNL-00-15	Conv. Str.	5.7	6	6.0 CRH	1025	N/A	N/A	24.0
SNL-00-16	CSPC	5.7	6	6.0 CRH	1471	0.5U	0.2R	39.0
SNL-00-06	Low Strength	3.3	6	3.0 CRH	457	0.3D	0.2L	9.4
SNL-00-03	Low Strength	3.3	6	3.0 CRH	658	0.0	0.4L	16.5
SNL-00-02	Low Strength	3.3	4	3.0 CRH	820	0.4D	0.3R	24.4
SNL-00-01	Low Strength	3.3	4	3.0 CRH	931	0.2U	0.4L	29.9
SNL-00-05	Low Strength	3.3	6	3.0 CRH	1104	0.2U	0.1R	36.6
SNL-00-04	Low Strength	3.3	6	3.0 CRH	1242	0.3U	0.2R	46.5
SNL-00-08	Low Strength	3.3	6	6.0 CRH	782	0.5D	0.3R	22.8
SNL-00-07	Low Strength	3.3	6	6.0 CRH	1242	0.0	0.6L	49.2

3.1.1. Projectile

The projectiles in the experimental test series were constructed of 4340 R_C45 steel and consisted of two ogive-nose shapes (Forrestal, Frew, Hickerson, & Rohwer, 2002). The nose shapes are defined by the ratio of the projectile diameter defined as caliber radius head (CRH). A larger CRH indicates a larger distance from nose tip to the full diameter cross section. The two nose shapes are the 3.0 CRH and the more slender 6.0 CRH, shown in Figure 17. The 3.0 CRH and 6.0 CRH projectiles are 20.7 and 20.8 in. long, respectively, both are 3.15 in. in diameter. The average weight of the projectiles is 28.7 lbs. The projectiles contain a structurally mounted, single channel accelerometer which recorded in-situ, filtered, decelerations of the projectiles during launch and impact (Rowher, Heise, & Wilder, 2001).

Basic Problem

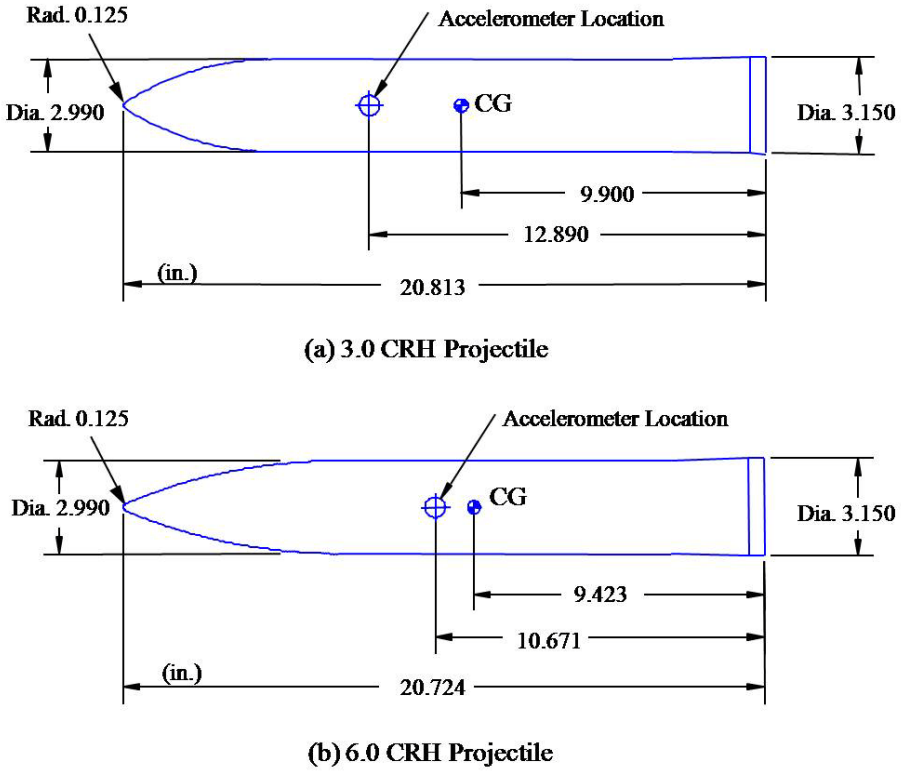

Figure 17. a) 3.0 CRH, b) 6.0 CRH Projectile Geometries in Inches (Forrestal, Frew, Hickerson, & Rohwer, 2002)

Experimental and modeling assumptions were made regarding the projectiles in this research. The projectiles were reused and launched into multiple targets in the validation tests; the abrasion and hardening or softening sustained by the projectiles is assumed to be negligible in this research as was assumed in the experimental work (Forrestal, Frew, Hickerson, & Rohwer, 2002). Additionally, the projectiles were modeled as a uniform material despite containing the accelerometer of different density. The assumed effective

density and projectile voids were modeled so that the weight and center of gravity of the projectiles matched the experimental test projectiles.

3.1.2. Target

The targets in the experimental test series varied in thickness and concrete strength. The targets were constructed by casting concrete into corrugated steel pipes six ft. in diameter, and allowed to cure for at least 140 days. Four ft. and six ft. target thicknesses were used in testing. The target concretes consisted of low-strength (3.3 ksi) and a conventional-strength (5.7 ksi) concrete; the unconfined compressive strengths were determined on the testing date, 140 or more days after the pour, unlike the 28 day test common to civil engineering practice. Table 5 provides detailed material descriptions of the experimental concretes. Further concrete strength testing provided in the experimental data included tests of unconfined uniaxial compression, triaxial compression, and uniaxial extension (Frew, 2002). The mix design and strength testing data was used to fit the material models used in this research.

Table 5. Mix Design and Properties of the Experimental Concrete (Forrestal, Frew, Hickerson, & Rohwer, 2002)

Average Strength		**Low (3.3 ksi)**	**Conventional (5.7 ksi)**
Mix Design			
	Cement (lb/yd^3)	523	539
	Sand (lb/yd^3)	2579	1483
	Aggregate (lb/yd^3)	135	1568
	Water (lb/yd^3)	438	303
	Water Reducer (lb/yd^3)	3.71	3.88
	Aggregate Type	Quartz	Limestone
	Maximum Aggregate Size (in.)	0.374	0.374
Physical Properties			
	Wet density (pcf)	127	140
	Dry density (pcf)	123	137
	Grain density (pcf)	165	165
	Water content (%)	3.1	2.6

The modeling of the target in this analytical research involved certain assumptions. The concrete target material was assumed to be uniformly mixed and cured for each test case and was treated as a homogeneous material. In the experiments, the target remained in the steel culvert during the impact test. For the analytical simulation the confinement was assumed to be negligible. It has been shown that confinement has significant effect on the strength of

concrete cylinders in compression testing (Ashby & Hallam, 1986; Joy & Moxley, 1993; Cargile D. , 1998). However, Sjol and Teland (2001) have shown that in impact testing the boundary effects of steel confinement significantly reduce as the ratio of target to projectile diameter, d_t/d, approaches 25 in./in. (Sjol & Teland, 2001), illustrated in Figure 18. Sjol and Teland conclude that analytical and experimental work indicate confining boundary effects can be neglected for tests involving target to projectile diameter ratios beyond 15 . In the validation impact tests used in this research, the target-projectile diameter ratio equals 22.5.

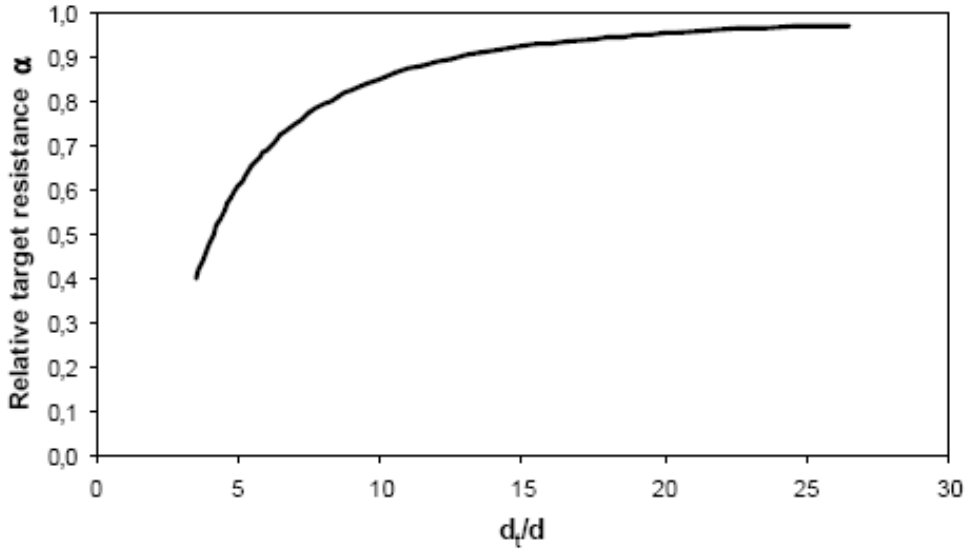

Figure 18. Relative Target Resistance with Respect to the Target-Projectile Diameter Ratio (Sjol & Teland, 2001)

3.1.3. Initial and Boundary Conditions

The initial and boundary conditions in the validation experiments include the velocity and angle of the projectile at impact as well as the restraint placed on the targets during the impact event. The impact tests were conducted by launching the projectiles horizontally from a 3.27 in. diameter powder gun at varying velocities from 456 to 1497 ft/sec. While the test setup was structured in a way to avoid oblique impacts, slight inclination angles did exist upon projectile impact. These inclination angles, captured by high speed digital photographs, were recorded in the experimental data and applied in the analyses. The concrete target contained in the corrugated steel was placed in a carriage restraint for the experimental impact tests; this restraint is described by the diagram in Figure 19.

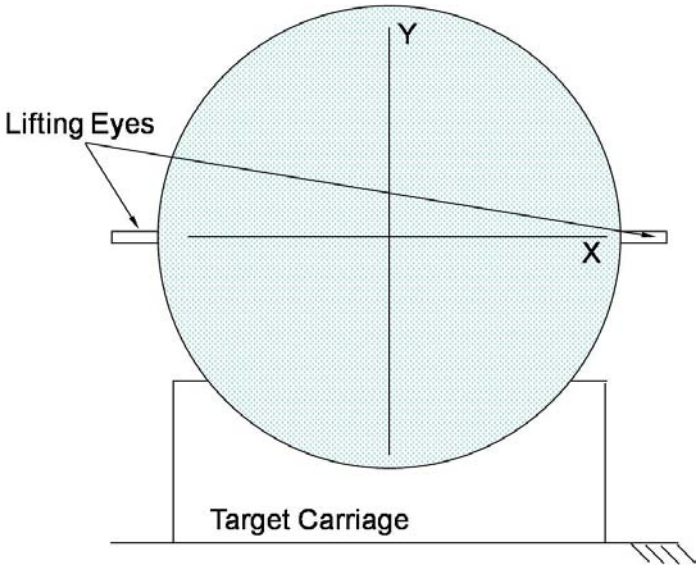

Figure 19. Experimental Target Setup (Frew, 2002)

For the analytical calculations the effect of gravity on the problem is neglected due to the short length of time over which the event takes place, less than six milliseconds. The interaction of gravity on the event is small relative to the forces caused by impact. For all codes with available options, the angles at impact were included and the carriage restraint was modeled consistent with the experimental tests.

3.2. Analysis Methods

Concrete material models and analysis code pairings were evaluated on their ability to reproduce specific concrete penetration results as well as available output and CPU run time. Analysis codes of different foundational backgrounds will be included in this work, and certain concrete constitutive models available in the analysis codes will be used.

3.2.1. Material Models

While the projectiles in the selected experimental case study consist of a material with strength much greater than the impact pressures experienced during the impact event, the material model selected in analysis is significant. In order to better evaluate the performance of concrete material models and the modeling techniques, the effect of the projectile material model will be isolated by keeping the model constant when possible. The material model selected for the projectiles is the Johnson Cook (JC) strength model for solids. This model

has been shown to be an adequate representation of metals (Johnson and Holmquist, 1988) and is available in three of the four modeling programs used in this research. A simpler von Mises plasticity model is used where the JC model is unavailable.

Five commonly available concrete material models will be evaluated due to the direct influence concrete model response has on the accuracy of the modeling program. The Drucker-Prager, Osborn, Brittle Failure Kinetics, Holmquist Johnson Cook and Karagozian & Case concrete models were selected based on code availability and popularity.

3.2.2. Analysis Packages

The four analysis packages compared in this research represent a cross-section of both popular and promising techniques. Two Finite Element Method (FEM) analysis programs are considered in this work, EPIC and LS-DYNA. A third program, CTH, is a Finite Difference Method (FDM) code. The final analysis option is the Material Point Method (MPM) implemented in a two-dimensional FORTRAN code.

3.2.2.1. EPIC

Development of the EPIC FEM analysis software for high velocity elastic-plastic impact began at the Ballistic Research Laboratory in 1977 (Johnson et al. 2006). The 2006 version by Network Computing Services Incorporated is used in this research and is a limited distribution code. With impact analysis as one of its original and continued design goals,

EPIC stands for Elastic Plastic Impact Calculations. For this reason, EPIC contains many useful material models common to projectiles and structural targets as well as useful design features for contact, boundary conditions, and erosion (Johnson et al. 2006). For this research, the three-dimensional tetrahedral modeling method in EPIC is used for evaluation.

3.2.2.2. LS-DYNA

LS-DYNA development has focused on the analysis of structural impact and impulse loading. Evolving from DYNA3D, developed in 1976, LS-DYNA is the commercial version of the software from Livermore Software Technology Corporation (Hallquist, 2006). Version 971 released in 2007 is used in this research. LS-DYNA provides an extensive library of material models, contact options, and other features (Livermore Software Technology Corporation, 2007). While LS-DYNA offers a wide variety of solution types useful for impact and penetration, for the purpose of evaluation, the three-dimensional finite-element hexagonal modeling method is used in the analysis.

3.2.2.3. CTH

CTH is the only finite difference code evaluated in this research. Created by Sandia National Laboratories, CTH is a limited distribution code. Because CTH is an explicit, Eulerian program, it is able to handle the large deformations associated with concrete impact and penetrations. However, to gain computational efficiency, CTH employs a Lagrangian

phase in solving the governing equations while deformations are not large (Crawford et al., 2007). Version 8.1 released in 2007 is used in this research. CTH provides a range of models for materials common to impact as well as several advanced features including adaptive mesh refinement. For the purpose of this evaluation, the standard three-dimensional finite difference solution is selected for analysis. Due to the nature of the fixed mesh in Eulerian methods, difficulties were encountered applying the saddle boundary constraint as a curved surface. As an alternative, a simpler tangential boundary condition was applied to the target.

3.2.2.4. MPM

MPM is an ALE code implemented in FORTRAN by Allen York, Shijian Zhou, and Deborah Sulsky at Sandia National Laboratories (York et al., 1997). It is a research code and not commonly available. MPM has shown potential for improving upon the more common Lagrangian and Eulerian methods, especially in impact and contact problems. Contact between different materials is handled inherently. While still in the developmental stages, MPM provides a limited number of constitutive models and options. This method is limited to a two-dimensional version at this time; hence a cylindrically symmetric boundary condition is applied to the two-dimensional model. Due to the dimensional limitation, a full circumferential boundary condition is applied to the target by constraining the outer surface in the radial and longitudinal directions. Also, any inclination angles of the impact must be neglected due to this restriction in dimensions.

3.2.3. Summary of Packages and Models

The availability of material models differed between codes and Table 6 and Table 7 list the selections made for each analysis methods in order to best compare both the analysis program and the concrete constitutive models available. The analysis code-material model pairing names are formed by the first letter of the analysis code and a number identifying the case run by the code. This naming convention for analysis pairings will be used throughout. Symbols and color selections for displaying results are also shown. Shaded cells in Table 6 and Table 7 indicate unavailability of a material model for the corresponding analysis package.

Basic Problem

Table 6. Analysis Matrix for Target Material Models

Analysis Program	Target Material Model				
	DP	HJC	KC	Osborn	BFK
EPIC		E-1		E-2	
LS-DYNA		L-1	L-2		
CTH		C-1			C-2
MPM	M-1				

DP - Drucker-Prager, HJC – Holmquist Johnson Cook,
KC – Karagozian and Case, BFK – Brittle Failure Kinetics

Table 7. Analysis Matrix for Projectile Material Models

Analysis Program	Projectile Material Model	
	VM	JC
EPIC		E-1, E-2
LS-DYNA		L-1, L-2
CTH		C-1, C-2
MPM	M-1	

VM – von Mises, JC – Johnson Cook

3.3. Comparison and Evaluation

In order to compare and evaluate the analysis packages and material models, a three phase study is conducted in this research. The study consists of a preliminary evaluation, a method comparison, and an experimental parameter study. The goal of the first two phases is to evaluate all the analysis code-material model pairs against a subset of experimental data to select a single best choice. Further investigation of parameter sensitivity will be performed using the selected analysis pairing in the experimental parameter study.

3.3.1. Preliminary Evaluation

A preliminary evaluation was performed in order to eliminate any unsatisfactory methods, and focus efforts only on promising analysis pairings. A single validation test from Table 4, SNL-16/3, was modeled by all eight of the material model-analysis program pairings. The preliminary evaluation enabled any obviously weak models or packages to be eliminated from the remaining analytical evaluations.

3.3.2. Method Comparison

From the 15 original validation tests, a four test subset was run on the analysis pairings that remained after the preliminary evaluation. Table 8 displays the subset matrix. Tests were selected to inspect modeling trends with regard to projectile nose shape and concrete strength. Also, the validation tests were inspected for accuracy; tests where impact occurred

away from the center of the target were not used in the method comparison. After the study, a single analysis pairing was identified as the best performing analytical option.

Table 8. Method Comparison Test Matrix

Test Name	Concrete Target			Projectile				Penetration Depth
	Type	Strength (ksi)	Thickness (ft)	Nose Shape	Velocity (ft/s)	Obliquity (degrees) Pitch (Up/Down)	Obliquity (degrees) Yaw (Left/Right)	(in)
SNL-00-14	CSPC	5.7	6	3.0 CRH	1497	0.2U	0.2R	37.0
SNL-00-16	CSPC	5.7	6	6.0 CRH	1471	0.5U	0.2R	39.0
SNL-00-05	Low Strength	3.3	6	3.0 CRH	1104	0.2U	0.1R	36.6
SNL-00-07	Low Strength	3.3	6	6.0 CRH	1242	0.0	0.6L	49.2

3.3.3. Experimental Parameter Study

The full experimental test series in Table 4 was run on the selected analysis code and concrete material model from the method comparison study. This study uses the variations of experimental parameters and not solution options to understand how target strength and thickness, projectile shape, impact angle, and impact speed affect the penetration depth, impact crater, and overall target damage.

3.3.4. Evaluation Criteria

The modeling methods were evaluated based on their ability to accurately capture the experimental results, the package limitations, and CPU run time. Both mid-experiment and post-experiment data was available for validation. A grading system was devised for the

preliminary evaluation and method comparison. Single points were given based on penetration depth, projectile mass loss, availability of damage, ability of software to model three dimensions, and availability of appropriate boundary conditions. Multiple points were given based on accuracy of model deceleration curve features and CPU run time.

Penetration depth, defined as the largest depth reached by the projectile tip into the target, was measured for each test. Models within 10% of the experimental penetration depth were given one point. Projectile mass loss was compared by percentile with the experimental data; points were given to models within 75% of the measured value which equates to a range of 1.12 lbs for the test with largest projectile erosion of 2.61%. The single channel accelerometer provided in-situ decelerations of the projectiles during launch and impact with a cutoff frequency of 15.4 kHz and the ability to capture data between +10,000 to -30,000 g (Rowher, Heise, & Wilder, 2001). A 5.0 kHz moving average was applied to both experimental and analytical deceleration curves to normalize comparison. Models were given up to three points by predicting features of the experimental deceleration curve: peak decelerations, slope of the descending curve, and end time of deceleration. Effective maximums were calculated as the maximum deceleration of the moving average curve; the bounds for grading were within 15% of experimental effective maximum. Descending curve slopes were determined by a linear fit line between two points: 0.5 ms past moving average maximum and 0.5 ms before moving average end time; grading bounds were +/- 20% of the experimental descending slope in G/ms. The end times were selected where the moving

average crossed the axis of time; the bounds for grading were +/- 0.5 ms. An example of the experimental acceleration data with moving average filtering and grading system is shown in Figure 20.

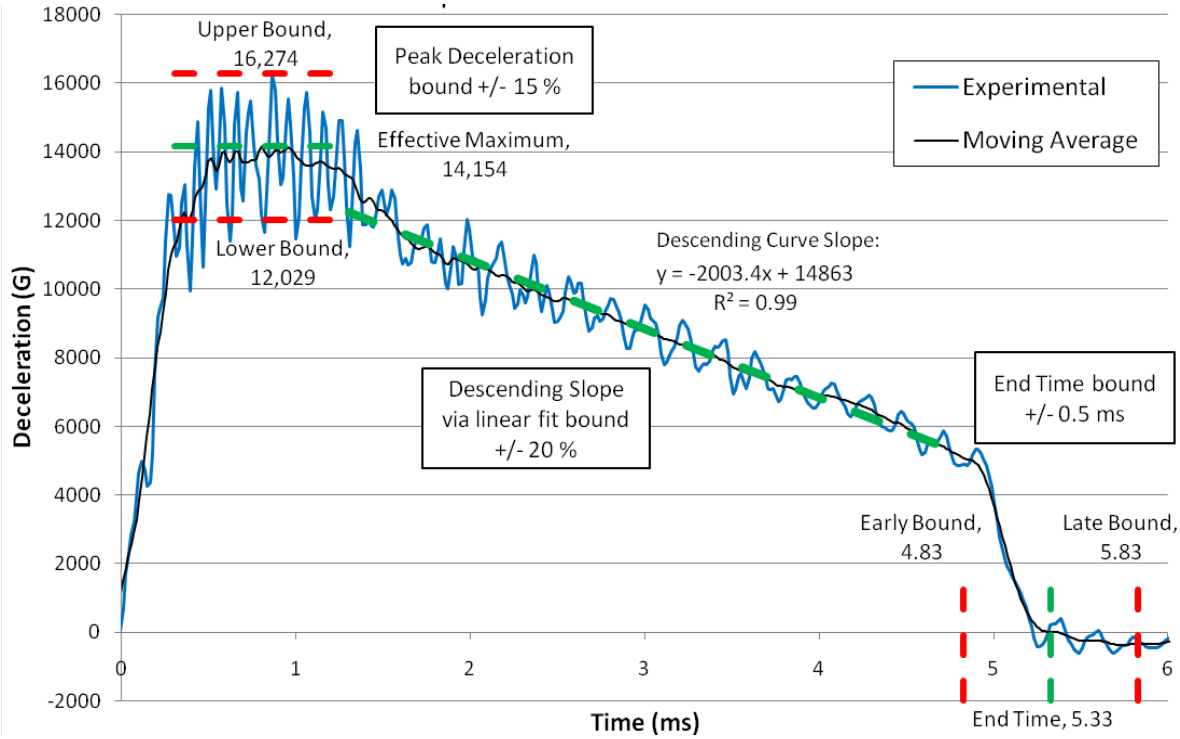

Figure 20. SNL-16 Deceleration and Example Grading System

Points for CPU run time were given to models in the lowest two thirds of the analysis matrix with times in the lowest third receiving two points and times in the middle third receiving one point. Impact crater profiles in the x and y radial directions and post-test photographs shown in Figure 21 were also supplied for each test; as part of the experimental parameter

study, these profiles were compared with the target deformation found in the analyses as well as with contours of damage parameters found in certain concrete material models.

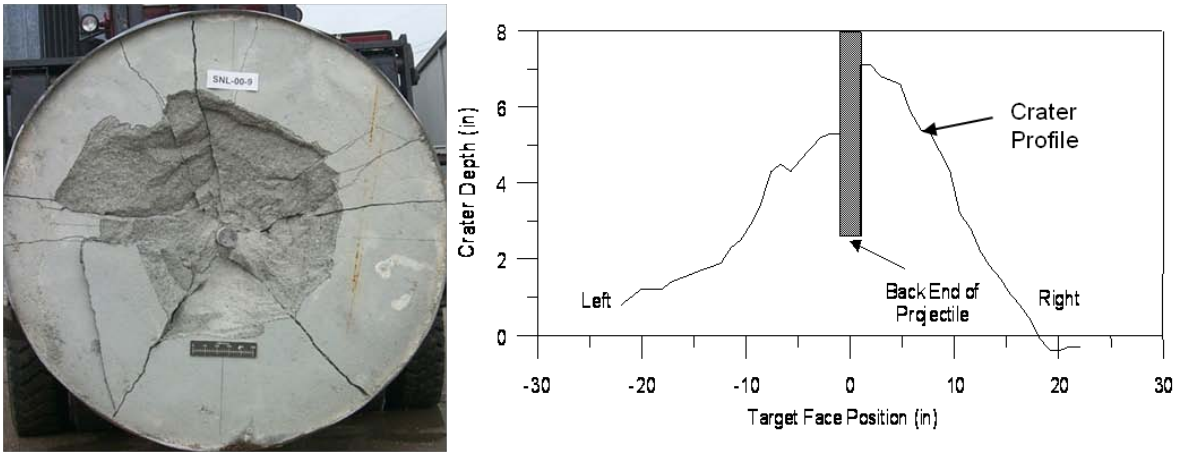

Figure 21. Target Damage and Crater Profile for Validation

Table 9. Sample Grading System

Grading System	Penetration Depth	Projectile Mass Loss	Deceleration	Damage	Boundary Condition	Dimensions	RunTime	Total
Total Possible	**1**	**1**	**3**	**1**	**1**	**1**	**2**	**10**

3.3.5. Conclusion

The research consisting of three sequential phases will evaluate the performance of several analytical methods in analyzing concrete impact and penetration problems. The preliminary evaluation will compare the full analysis matrix shown in Table 6 in order to

observe the effectiveness of a broad range of analytical methods including Lagrangian, Eulerian, and meshless techniques. The second phase of the study, the method comparison, will further inspect the most successful analysis methods of the preliminary evaluation for trends in accuracy. Using an extended set of four experimental tests as validation, the method comparison will expose potential areas of strength or weakness in the selected analysis codes and material models. As the final phase of the study, the experimental parameter study will investigate trends in the full range of the experimental test series and determine the ability of a single analysis code-material model combination to capture the experimental trends.

4. Analytical Investigation

The methodologies specific user experience of the four analysis codes used in this research will be discussed in the following section. The input, output, material models, and significant features or limitations will be presented.

4.1. EPIC

The 2006 version of the EPIC code used in this research can solve three-dimensional impact problems by both FEM calculations and analytical equations. A graphical user interface is also included; however, the interface allows for limited modification to problem geometries, refinement, and boundary conditions for FEM impact and penetration analysis. For more specific input the preprocessor and subsequent main EPIC routine can receive manually created input files. The code includes thorough user instructions (Johnson, et al., 2006), extensive material library, and numerous material models with customizable parameters. Of the available material models, three are used in EPIC simulations: Johnson Cook (JC) is used for the projectile, Osborn and Holmquist Johnson Cook (HJC) are used for the characterizing the concrete target. The 2006 version can be run in parallel, however for this research, serial calculations were performed. Output files are created for state and time plots by the two EPIC postprocessors.

4.1.1. Input Data

To run the EPIC code without the graphical user interface, two input files are necessary: a main ASCII text input file and a Patran mesh file. The main input file contains system parameters necessary for the execution of the preprocessor and main routine. The preprocessor receives information regarding the material properties, material geometry, contact definitions, boundary conditions, and initial conditions. The main input file can indicate to the preprocessor to look for a mesh file containing a target and projectile. The mesh generation software, Cubit version 11.0, was used to create three-dimensional tetrahedral mesh files in Patran format, shown in Figure 22. The target mesh geometries were created with increased refinement at the area of impact while limiting element skew and approximately matching the element width of the projectile at the location of impact. The tetrahedral elements used are those described previously in Section 2.2.2. This element type was developed for accuracy and efficiency in large deformation analysis of solids (Beissel & Johnson, 2000) and recommended by the EPIC user manual (Johnson, et al., 2006). The EPIC user manual recommends only Patran versions 2.4, 2.5, or 3.0; however, version 5.0 Patran mesh files used in this research were compatible. Translations, rotations, and scaling factors can be applied to target and projectile bodies as parameters in the main input file. Constrained nodes on the target in the saddle-like formation, shown as green dots in Figure 22, must be specified in the main input file. In the last portion of the main input file, the main

routine receives information regarding simulation limits, calculation settings, and output options. The main routine can also be used independently to restart or extend already completed calculations to longer simulation times.

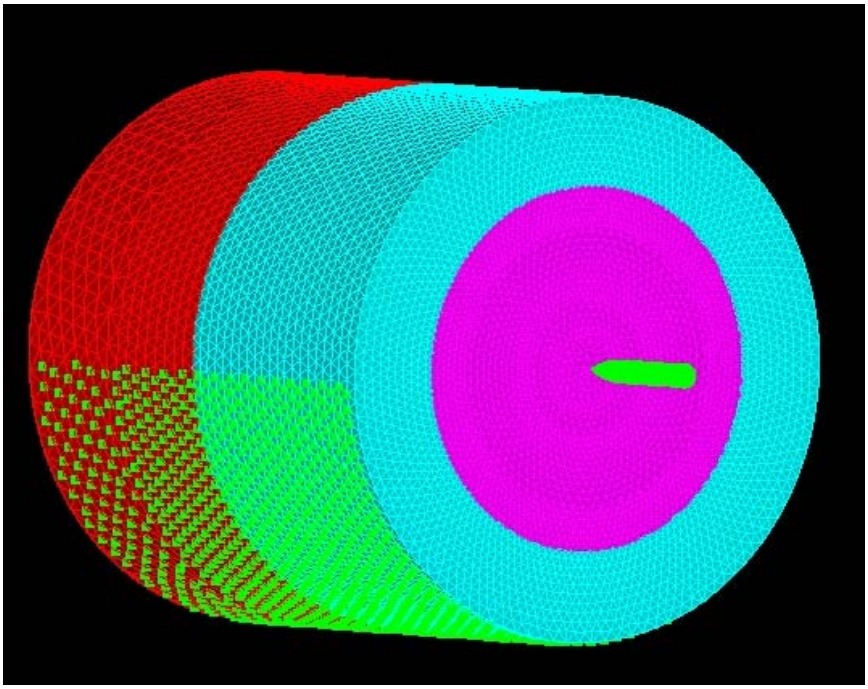

Figure 22. Example Three-Dimensional EPIC Mesh

4.1.2. Material Models

The Johnson Cook material model was selected for the steel projectiles in EPIC. Although the experimental steel had an RC number of 45, a library model for 4340 steel with a similar RC number of 49 was selected from the material library for the projectile material.

Table 10. JC Material Constants

		4340 Steel RC-49
Mass / Thermal		
Density	(lb*s^2/in^4)	7.32E-04
Specific Heat		4.114E+06
Strength		
A		2.19E+05
B		9.1E+04
N		0.16
M		1.19
C		0.006
D		0
SMAX		0
Damage		
D1		-0.63
D2		1.43
D3		-0.5
D4		0
D5		0
EFMIN		0.041
Pressure		
Gruneisen Coef.		1.16
Max Negative Pressure		1.0E+07
K1	(psi)	2.38E+08
K2	(psi)	4.27E+08
K3	(psi)	7.25E+08

The Osborn model was fit to the experimental concrete by the material test data from the testing reports by Frew (2002). A linear fit to triaxial compression maximums determined the strength constants A and α, while the strain rate constant C was set to zero as was done in the original implementation(Johnson, et al., 2006). The equation of state was determined by fitting hydrostatic test data to three response regions: elastic (linear), crushing (polynomial), and locking (linear), shown in Figure 7 b).

Table 11. Osborn Material Constants

		Low Strength	Conventional Strength
Mass / Thermal			
Density	(lb*s^2/in^4)	1.907E-04	2.104E-04
Specific Heat		5.63E+05	5.63E+05
Strength			
Shear Modulus	(psi)	1.141E+06	1.715E+06
A		3333	3333
B		1.0	1.0
C		0.0	0.0
SMAX		1.533E+05	1.533E+05
Pressure			
Pcrush	(psi)	5000	4641
μcrush		0.008	0.007
K1	(psi)	3.465E+05	2.452E+05
K2	(psi)	-9.262E+05	-3.051E+05
K3	(psi)	1.322E+07	9.346E+06
Klock	(psi)	2.600E+06	1.034E+07
μlock		0.200	0.189
T	(psi)	125.2	162.4

Analytical Investigation

The HJC model was implemented using the method demonstrated by Holmquist et al. (1993). The triaxial compression data from the Sandia concrete material tests was used to select the strength fit constants, SMAX, B and N, while recommended values were used for the cohesion constant A, and strain rate constant C. The damage parameters were assumed considering recommendations from Polanco-Loria et al. (2008). The effective plastic strain limit (EFMIN) was assumed as 0.01 for low strength concrete and 0.005 for conventional strength. The constant D2 was assumed as the suggested value of 1.0 and D1 was calculated as recommended by Holmquist et al. (1993). Many of the HJC pressure constants were determined using the formulas based on the Sandia concrete unconfined compressive strength, $f'c$, and concrete and aggregate densities; the remaining pressure constants were determined by fitting the pressure model to the concrete hydrostatic compression testing. The locking pressure, P_{crush}, was calculated as $f'c/3$, and crushing volumetric strain, μ_{crush}, was calculated as $P_{crush}/K_{elastic}$, where $K_{elastic}$ is the elastic bulk modulus determined from the hydrostatic compression tests. The locking volumetric strain, μ_{lock}, is calculated as $(\rho_{grain} / \rho_0) - 1$, where ρ_{grain} is the grain density and ρ_0 is the original wet density of the Sandia concrete. The pressure locking constants, K1, K2, and K3 are intended to be determined by shock Hugoniot data for the concrete aggregate which was unavailable for the experimental concrete; the pressure locking constants were set to the values determined by Holmquist et al. (1993) as the Sandia experimental concrete aggregate was of similar type and size. P_{lock} was used as a fit parameter for the concrete hydrostatic compression tests. Figure 24 shows the

difficulty in fitting the locking portion of the data for the experimental concretes, especially for the low strength concrete. The calculation of μ_{lock} sets the locking region of the model at higher levels of volumetric strain than reached by the material test data. The lower strength concrete does have a lower wet density, but the ρ_{grain} for both concretes is estimated in the Sandia material test data as165 pcf which seems high. An alternative method to avoid this incongruence of data and model would involve ignoring the recommended formula for μ_{lock} that uses the estimated value of ρ_{grain} , and select the value for μ_{lock} that best fits the model to the hydrostatic compression test data. Summary of HJC material constants for the low and conventional strength concretes is shown in Table 12.

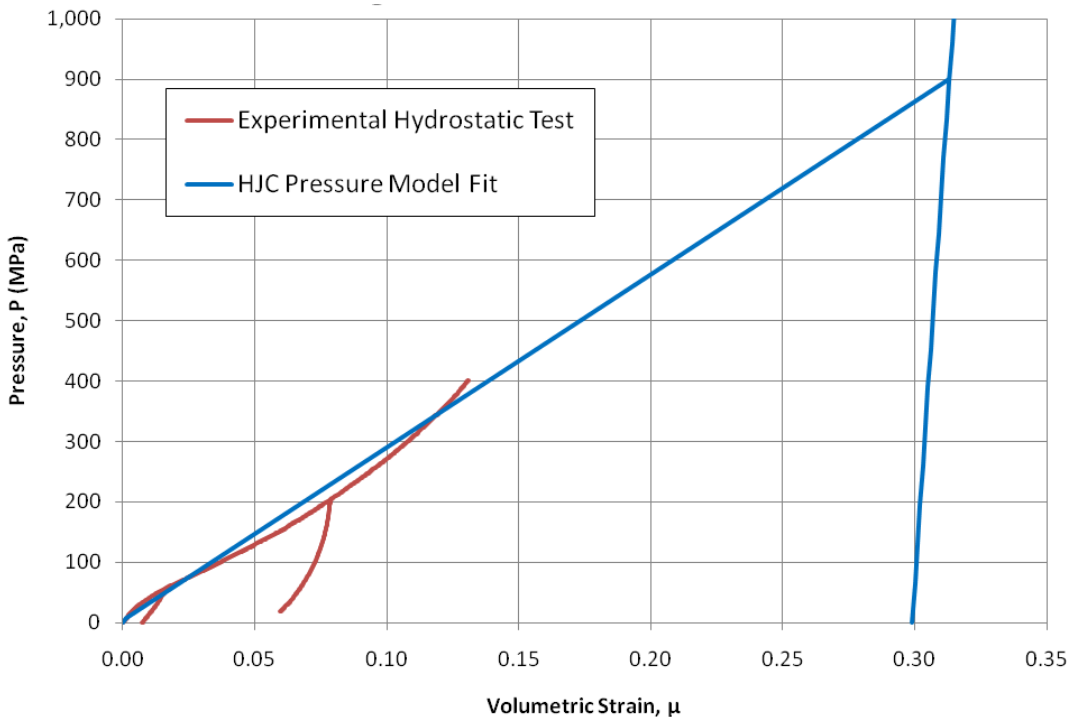

Figure 23. Fitting of HJC Pressure Model for Low Strength Concrete

Table 12. HJC Material Constants for Low and Conventional Strength Concretes

		Low Strength	Conventional Strength
Mass / Thermal			
Density	(lb*s^2/in^4)	1.91E-04	2.10E-04
Specific Heat		5.63E+05	5.36E+05
Strength			
A		0.79	0.79
B		1.602	1.769
N		0.870	0.773
C		0.007	0.007
f'c	(psi)	3335.9	5613
SMAX		30	16
Damage			
D1		0.036	0.02
D2		1	1
EFMIN		0.01	0.005
Pressure			
Pcrush	(psi)	1112	1871
µcrush		0.00128	0.00115
K1	(psi)	1.23E+07	1.23E+07
K2	(psi)	-2.48E+07	-2.48E+07
K3	(psi)	3.02E+07	3.02E+07
Plock	(psi)	1.31E+05	7.25E+04
µlock		0.2990	0.1778
T	(psi)	377	487.3

To calibrate the Osborn and HJC models in the EPIC code, an ultimate failure strain is used in conjunction with the material model to define an equivalent or volumetric strain at

which a concrete element fails and can contribute no pressure or stress to the analysis. The failure strain value for each material model is determined iteratively using the penetration depth of an individual impact test as validation. This, in addition with the contact definition, prevents highly distorted meshes in impact problems with large deformations.

4.1.3. Contact Definition

For FEM analysis of impact problems using the EPIC code, a contact definition, also referred to as a sliding interface, must be defined. The contact definition options for three-dimensional analysis in EPIC include element erosion with or without mass retention, erosion with particles, and kinetic friction. Eroding contact definitions are a common method in FEM analysis to avoid highly distorted, numerically unstable mesh elements. While erosion with particles was attempted in this research with some success, it is a newer, less validated option; and the more common element erosion option was used for the presented results. For the common element erosion contact, the master elements are given a value of equivalent or volumetric strain at which the element will erode and the eroded mass will be retained at the remaining nodes. For this research, all the elements of the projectile are defined as master elements. An erosion strain of 5.0 is iteratively determined for the 4340 steel material by matching projectile mass loss to that of the experimental impact test, SNL-16, used for validation in the preliminary evaluation and applied consistently in all later analysis.

4.1.4. Output Data

Output data is post processed by the two EPIC postprocessors to make state plots and time plots. State plots include two-dimensional and three-dimensional plots of material geometries with optional contours of pressure, stress, equivalent strain, damage, and internal energy. Time plots can also be made for energy, plastic work, maximum coordinates, momentum, velocity, and acceleration of the projectile, target, or entire system. The EPIC postprocessors output postscript files which require a postscript viewer and can make exporting data difficult. Alternative means of post processing are provided with optional output in a form readable by other third-party postprocessors including Tecplot.

4.1.5. Code Use

The short form graphical user interface does provide many options for three dimensional FEM analysis that can serve as helpful templates; however, as with any template, the range of detailed problems that fit the template is limited. In this research, projectile and target geometries, refinement levels, and boundary conditions could not be adequately applied through the short form interface, and manually created input was required. In general, the EPIC code produced reasonable results for the impact validation tests in this research. The recommended method for handling contact for concrete impact and penetration was followed in this research where erosion of the projectile is handled by the contact definition and the

erosion of the concrete target is determined by a failure strain value associated with the material model. It is unclear why erosion for both materials is not handled by the contact definition. An attempt was made to model contact for both materials through the eroding contact feature; it was observed the code neglected the erosion strain input for the concrete material. It was also noticed that as failure strain for the concrete material model is iteratively determined for accurate penetration depths, the ability to predict damage is reduced significantly. High erosion strain values input for the concrete result in target damage that closely models the observed crater region, but analysis penetration depths are much lower than experimental values. Failure strain values for the concrete corresponding to accurate levels of penetration depth show very limited damage to the target.

The EPIC code is a user-friendly analysis code with many useful features for modeling and post processing impact and penetration problems. The short form user interface and numerous library materials are helpful in analyses where there is limited knowledge about the material properties, and where geometries can be approximated. While the methods for manual creation of input can be cumbersome, the capability to specify detailed target and projectile geometries and properties is useful in scenarios where data is available such as in this research. Much of the tools and options are tailored to impact problems, hence features including projectile deceleration can be easily retrieved. Contact for concrete impact and penetration could be improved if the dependency of erosion on a constant strain value were removed. Concrete failure is additionally dependent upon pressure which is demonstrated in

many material models. The application of a constant failure strain value limits the usefulness of the material models. Ideally failure would be determined by a factor integrated into the material models allowing the inclusion of pressure and possibly other factors on failure or erosion.

4.2. LS-DYNA

The 2007 version of LS-DYNA used in this research provides theory and user manuals (Hallquist, 2006; Livermore Software Technology Corporation, 2007), numerous material models, and various contact options useful for concrete impact and penetration analysis. Of the available material models, three are used in LS-DYNA simulations: Johnson Cook (JC) is used for the projectile, Holmquist Johnson Cook (HJC) and Karagozian and Case (K&C) are used to characterize the concrete target. The code includes an advanced and separate pre- and post-processor, called LS-PrePost, for efficient input creation and output management. The 2007 version can be run in parallel; however, the three-dimensional FEM calculations for this research are performed in series.

4.2.1. Input Data

While a single comprehensive input file can be created through LS-PrePost, input was segmented into separate files according to material geometry, concrete material properties, and steel material properties, and then linked by a main input file passed to the main LS-

DYNA routine. This input file organization was used because it was discovered during this research that certain material model inputs were erroneously changed by LS-PrePost upon saving the file. The separation of the input files made manual input creation and editing more efficient. The three-dimensional hexahedron meshes for the targets and projectiles were created with the aid of a Matlab routine to apply gradient mesh scaling along the length of the target as well as to the target cross section, shown in Figure 24. The mesh geometries were created to limit initial element skew and approximately match the element width of the target to the projectile at the point of impact. LS-PrePost was then used to modify the mesh geometries, where necessary, and apply initial and boundary conditions. The eight-node hexahedron elements with one-point Gaussian quadrature used in this research were recommended by the LS-DYNA user manual for their accuracy and efficiency as previously mentioned in Section 2.2.2. While the main file links the mesh file and material property files, it also defines the contact definition, main routine settings, and output options.

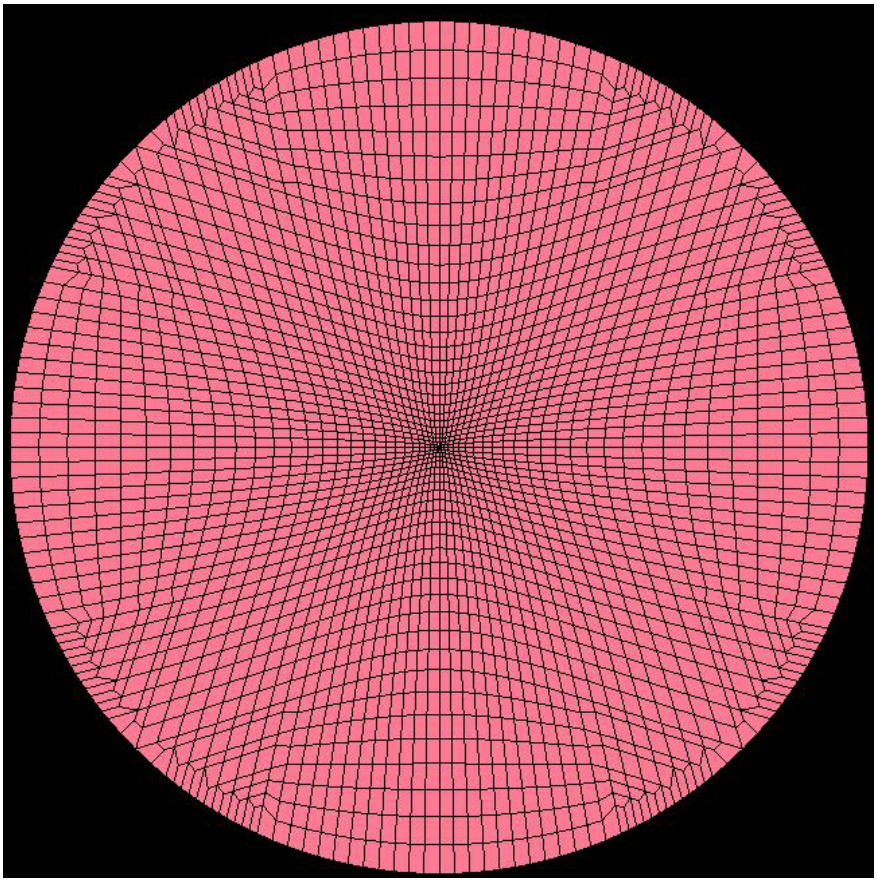

Figure 24. Example LS-DYNA Target Mesh

4.2.2. Material Models

For the JC model used for the steel projectile, constants were obtained from the EPIC library model for 4340 steel with an RC value of 49 in order to isolate the projectile material input between analysis codes. However, in LS-DYNA, the JC model requires an independent equation of state unlike the EPIC JC model which includes a Mie-Gruneisen equation of

state. The LS-DYNA equation of state referred to as Linear Polynomial was fit to the Mie-Gruneisen equation of state for the EPIC material model; this required that heat conduction be neglected. Also, the failure strain term that exists in the EPIC library model is determined internally by a failure strain equation and was not an external variable to be modified as in the LS-DYNA JC model. The failure strain equation is given in terms of five "D" material constants from the EPIC library model, pressure p, effective stress σ_{eff}, normalized strain rate $\dot{\varepsilon}^*$, and homologous temperature T^*:

$$\varepsilon^f = \left[D_1 + D_2 \exp\left(D_3 p/\sigma_{eff}\right)\right]\left[1 + D_4 \ln\left(\dot{\varepsilon}^*\right)\right]\left[1 + D_5 T^*\right] \qquad \textbf{Equation 2.12}$$

Two concrete constitutive models were used to characterize the concrete in LS-DYNA. The HJC model implementation in LS-DYNA was consistent with that of EPIC in Section 4.1.2. The K&C model was implemented for the concrete materials in LS-DYNA. The K&C strength and damage models were fit to experimental concrete compression data from Sandia. The eight strength model constants, defining curves of yield, maximum, and residual strength, were determined according to triaxial compression tests. The selection of yield points was unclear; so values for yield were taken as 45% of maximum, as was recommended by Malvar et al. (1997). The damage model pairs of λ and η were determined by a medium confinement triaxial test to define interpolation between yield, maximum, and residual curves. The "tabulated compaction" equation of state in LS-DYNA was fit to hydrostatic test data by points of volumetric strain, pressure, and unloading/reloading

modulus. Numerical instabilities were exhibited in calculations using manually fit K&C strength models. As an alternative, the automatic scaling method was used to fit the K&C strength and damage models to the experimental concretes. The scaling method, detailed in the work by Noble et al. (2005), proportions data from a well characterized 6600 psi concrete to specific concrete by f'c and concrete density. A recommended table of strain rate enhancement factors was included from the LS-DYNA user manual. The K&C material parameters are displayed in Table 13, Table 14, and Table 15.

Table 13. Summary of K&C Strength Material Parameters

	User Low Strength	Auto Low Strength	User Conv. Str.	Auto Conv. Str.
RO (lb*s^2/in^4)	1.91E-04	1.91E-04	2.10E-04	2.10E-04
Poisson's Ratio	0.20	0.19	0.20	0.19
F'T (psi)	377	353	487	499
A0	1.76E+03	9.86E+02	1.60E+03	1.66E+03
A1	7.48E-01	4.46E-01	5.81E-01	4.46E-01
A2	2.94E-06	2.42E-05	6.03E-06	1.44E-05
A0Y	7.93E+02	7.45E+02	7.20E+02	1.25E+03
A1Y	1.66E+00	6.25E-01	1.29E+00	6.25E-01
A2Y	6.54E-06	7.72E-05	1.34E-05	4.59E-05
A1F	6.97E-01	4.17E-01	5.55E-01	4.42E-01
A2F	3.32E-06	3.55E-05	6.10E-06	2.11E-05
OMEGA	0.6	0.5	0.6	0.5
Sλ	1	1	1	1
NOUT	2	2	2	2
EDROP	1	1	1	1
RSIZE	1	1	1	1
UCF	1	1	1	1
LOCWID	1.122	1	1.122	1

Table 14. Summary of K&C Equation of State Material Parameters

	User Low Strength	Auto Low Strength	User Conv. Str.	Auto Conv. Str.
EOS ID	8	8	8	8
GAMA	0	0	0	0
E0	0	0	0	0
V0	1	1	1	1
EV1 (in/in)	0	0	0	0
EV2	-2.77E-03	-2.77E-03	-5.34E-03	-5.34E-03
EV3	-1.41E-02	-1.41E-02	-2.53E-02	-2.53E-02
EV4	-4.39E-02	-4.39E-02	-4.53E-02	-4.53E-02
EV5	-9.03E-02	-9.03E-02	-6.53E-02	-6.53E-02
EV6	-1.48E-01	-1.48E-01	-8.26E-02	-8.26E-02
C1 (psi)	0	0	0	0
C2	846367	846367	1382957	1382957
C3	485835	485835	746537	746537
C4	311603	311603	649885	649885
C5	313057	313057	663137	663137
C6	391740	391740	702457	702457
K1 (psi)	1060035	1060035	1357824	1357824
K2	1153102	1153102	1567020	1567020
K3	1533336	1533336	2349233	2349233
K4	2074687	2074687	3131445	3131445
K5	2917516	2917516	3913658	3913658
K6	3965521	3965521	4593148	4593148

Table 15. Summary of K&C Damage Material Parameters

	User Low Strength	Auto Low Strength	User Conv. Str.	Auto Conv. Str.
λ01 (%)	2.41E-02	0	2.66E-02	0
λ02	5.06E-02	8.00E-06	4.57E-02	8.00E-06
λ03	7.60E-02	2.40E-05	6.55E-02	2.40E-05
λ04	1.02E-01	4.00E-05	8.54E-02	4.00E-05
λ05	1.28E-01	5.60E-05	1.05E-01	5.60E-05
λ06	1.54E-01	7.20E-05	1.25E-01	7.20E-05
λ07	1.86E-01	8.80E-05	1.47E-01	8.80E-05
λ08	2.16E-01	3.20E-04	2.35E-01	3.20E-04
λ09	2.45E-01	5.20E-04	3.23E-01	5.20E-04
λ10	2.73E-01	5.70E-04	4.10E-01	5.70E-04
λ11	3.02E-01	1.00E+00	4.96E-01	1.00E+00
λ12	3.31E-01	1.00E+01	5.84E-01	1.00E+01
λ13	3.69E-01	1.00E+10	6.78E-01	1.00E+10
η01	0	0	0	0
η02	6.60E-01	8.50E-01	3.22E-01	8.50E-01
η03	9.15E-01	9.70E-01	5.90E-01	9.70E-01
η04	9.25E-01	9.90E-01	7.97E-01	9.90E-01
η05	9.81E-01	1	9.15E-01	1
η06	9.95E-01	9.90E-01	9.63E-01	9.90E-01
η07	1	9.70E-01	1	9.70E-01
η08	8.60E-01	5.00E-01	8.00E-01	5.00E-01
η09	7.67E-01	1.00E-01	6.48E-01	1.00E-01
η10	5.52E-01	0	5.31E-01	0
η11	4.00E-01	0	3.78E-01	0
η12	2.73E-01	0	1.75E-01	0
η13	0	0	0	0
B1	1.15	1.60	1.00	1.60
B2	1.35	1.35	1.35	1.35
B3	1.15	1.15	1.15	1.15

To fit the HJC and K&C models to the LS-DYNA code, an ultimate failure strain is specified for each material model to define an equivalent or volumetric strain at which the concrete element fails and can produce no pressures or stresses. The failure strain value for each material model is determined iteratively using the penetration depth of an individual impact test as validation.

4.2.3. Contact Definition

LS-DYNA contains numerous methods and options associated with the definition of contact. Eroding contact was selected to avoid high distortions and numerically instabilities due to large material deformations. Erosion strain values are defined outside of the contact definition with the material models, but the use of the eroding contact definition allows contact to remain after surface elements are eroded. Additionally, due to the large differences between the stiffness values of the concrete and steel materials, a penalty stiffness method is used by setting contact variable “SOFT” equal to two; without this measure the contact between the two bodies was lost after surface elements were eroded.

4.2.4. Output Data

LS-PrePost has extensive capabilities for viewing and managing results from three-dimensional FEM analyses. Three-dimensional state plots can be easily generated with cross-sections and contours of stress, strain, pressure, internal energy and other field variables.

Time plots of energy, displacement, velocity, acceleration, stress, and other results can also be generated per material, element, and/or node.

4.2.5. Code Use

In the analyses of the Sandia validation tests, the projectile mass loss in LS-DYNA was typically much higher than the experimental values; this is most likely because the value of the failure strain was an internally calculated variable in the JC model and could not be altered. LS-PrePost is a powerful tool, but issues exist in the preprocessing of material property data. It was unclear how to set more frequent output data for acceleration without increasing the output of all state and time plot data which resulted in longer run times for the calculations and much slower post processing. Numerical instabilities were exhibited by concrete targets using manually fit K&C models, which may have been due to user error in the determination of the material constants. Therefore, the K&C scaling method was used to generate material parameters.

LS-DYNA is a highly capable analysis code for analyzing concrete impact and penetration and includes a powerful pre- and post-processor. Although the code is well documented and supported, it contains so many features and options the most difficult task for the user can be deciding exactly which settings and options to select. Developments in the contact definitions including advanced means to determine erosion could significantly

improve results in LS-DYNA. Also, other material models for concrete available in LS-DYNA involve higher levels of detail and could improve analysis.

4.3. CTH

CTH version 8.1, used in this research, is an FDM analysis code designed for a wide range of shock wave propagation and material motion problems in three-dimensions. The code includes a thorough user manual (Crawford, et al., 2007), several material models, and multiple post-processing options useful for impact and penetration problems. The code receives a single ASCII text input file and creates multiple output files. The material models in CTH used in this research are the Johnson Cook (JC), Holmquist Johnson Cook (HJC), and Brittle Failure Kinetics (BFK). Contact between materials is handled internally and boundary condition options are limited. In this research, CTH was run in parallel on up to four processors.

4.3.1. Input Data

No preprocessor is available with CTH version 8.1. Input is organized manually in a single text file according to six sections: calculation control, mesh, material properties, material geometries, boundary conditions, and output settings. Calculation control selects system parameters for the execution of the main routine including specified simulation time or cycle number at which to end calculation. The three-dimensional mesh is defined in the

quantity and spacing of grid cells in the x, y, and z directions; multiple regions of different grid spacing can be specified in each direction. In this research, grid spacing along the impact direction was held constant at two in. while the spacing in the other directions ranged from one to 10 in., with smallest spacing at the point of impact. The material bodies are specified using an assortment of commands that create and edit geometries within the region specified by the previously defined grid. Along with the material geometries, initial conditions can be specified. The normal boundary conditions in CTH can only be applied to the extreme bounds of the grid; however, rigid materials given constant zero velocities can alternatively be used to apply boundary conditions. The alternative boundary conditions were required for the cylindrical target constraints in this research, but even this method was limited to planar geometries and could only be applied at tangent points along the length of the target and not uniformly to the curved surface, as shown by the diagram in Figure 25. Additionally, due to the mixing of cells in CTH, even at the tangent contact points the target and rigid materials could not be fully constrained.

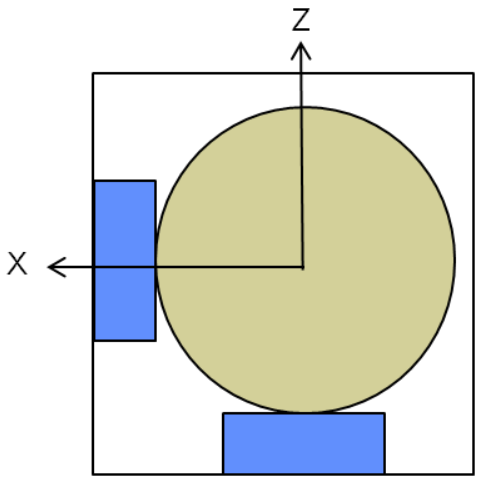

Figure 25. CTH Boundary Condition Diagram

4.3.2. Material Models

The JC model was used for the steel projectile in CTH. The JC model constants were obtained from the EPIC library model for 4340 steel to isolate the projectile material parameters between analysis codes. However, in CTH, similar to LS-DYNA, the JC model requires a separate equation of state. A predefined Sesame equation of state for 4340 Steel available in CTH was used.

The HJC model implementation in LS-DYNA was consistent with that of EPIC in Section 4.1.2. The BFK model was also used in CTH, and, because the full model fitting procedures were not available, the scaling method is detailed by Silling (2001) was used. The BFK scaling method is similar to that of the K&C model of LS-DYNA. The ratio of

unconfined compressive strength to a well characterized 6000 psi concrete is used to scale the strength model.

Table 16. BFK Material Constants

		6000 psi Reference Concrete
Strength		
Instantaneous f'c	(psi)	11,600
Instantaneous f't	(psi)	6,290
Brittle Ductile Transition	(psi)	14,800
f'c	(psi)	6,000
f't	(psi)	348
YMAX	(psi)	72,500
Pressure		
Initial Bulk Modulus	(psi)	4.09E+06
Limiting Bulk Modulus	(psi)	6.76E+06
Failed Bulk Modulus	(psi)	1.45E+05
Volumetric Recovery Strain		0.1
Volumetric Crushing Strain		0.2

Table 17. BFK Reference Equation of State Values

Volumetric Strain	Pressure (psi)
4.00E-03	1.09E+04
1.09E-02	1.95E+04
1.50E-02	2.40E+04
3.02E-02	4.17E+04
6.18E-02	8.05E+04
1.03E-01	1.39E+05
1.49E-01	2.31E+05
1.80E-01	3.42E+05
2.00E-01	4.89E+05
3.55E-01	2.22E+06
5.63E-01	3.63E+06

4.3.3. Output Data

Output for CTH is processed during and after the main routine. Output data processed during calculation is specified in the input text file and consists of state plots with optional contours of stress, pressure, and damage, and other field variables. Time plots of yield stress, pressure, damage, velocity, position, and other variables can be processed after the main routine by including tracer points in the input file.

4.3.4. Code Use

Results for CTH analyses of the Sandia impact tests generally resulted in less penetration than observed experimentally, and the code was limited in its ability to constrain the concrete target. Fixed, rigid material constraints could only be applied tangent to the curved surface of the target, and due to the mixing of cells, even at the contact between the target and constraints points could not be fully constrained. Also, projectile deceleration was one desired result which was not readily available; this required that acceleration be derived from velocity data which involves a loss of accuracy.

CTH provides an alternative to FEM analysis codes that requires much attention to contact definition; however, boundary conditions can be difficult to implement especially with curved material geometries. CTH could benefit from additional means to modify contact, and developing contact models for Eulerian codes like CTH have been found in

literature (Silling, 1993). Also a preprocessor and more advanced postprocessor for CTH would be significantly helpful in analysis and data export.

4.4. Material Point Method (MPM)

The MPM code used in this research is a developmental version. The modeling procedures do not include a graphical user interface, and no user manual or guide is currently available. In this work, the MPM FORTRAN code is run in series using a development environment (Microsoft Visual Studio), but can be run from an executable. The code receives an ASCII text input file and is capable of outputting multiple files of results.

4.4.1. Input Data

The analysis data is input by two sections: analysis control information, and material information. The analysis control information includes the grid discretization, rectangular geometric bounds, output settings, and limits involving time and tolerance of constitutive routines. Grid discretization is defined in two ways: the number of stationary grid cells in the x and y directions, and the number of material points that will be initialized per grid cell, in square numbers only due to algorithm requirements. The stationary grid cells are spaced evenly throughout the global geometric bounds. The boundary conditions are specified to the global bounds by setting the appropriate flag; the conditions include free-flow, rigid slip-free, and rigid no-slip. The maximum simulation time is input to determine the calculation

termination, and unlike the other codes in this research restart is not currently available. The material geometries are input as tabular points for x and y defining regions inside which to initiate material points. The maximum number of points to define a region is limited to 12; however, multiple regions can be used to define a complete material body. The material models are implemented though a maximum of 10 input parameters. Of the four available material models in the MPM code, von Mises (VM) and Drucker-Prager (DP) are used in this research.

4.4.2. Material Models

The von Mises model used for the steel projectile was implemented as linear-elastic, perfectly-plastic by an elastic modulus, Poisson's ratio, density, and yield stress. The Sandia test data for the 4340 Steel was limited to its Rockwell C hardness (RC) number of 45. The values for the von Mises material parameters were collected from a library material model for 4340 steel with an RC of 49, available in the EPIC code.

The DP model was implemented following the method demonstrated by Lopez-Cela (2002) previously mentioned in Section 2.3.1. The two yield surface parameters, α and k, were determined using the first yield strength in tension and compression from the material testing data provided by Sandia. The elastic modulus, E, was determined using the ACI standard, $33{w_c}^{1.5}\sqrt{f'c}$ (in psi), where w_c is the weight of concrete and *f'c* is the unconfined

compressive strength. The values for w_c and *f'c* were provided in the Sandia test data. A Poisson's ratio of 0.2 was selected which is common for concrete, and density was given in the Sandia material test data. For the flow rule and hardening rule of the model, values for β as well as hardening (E_h) and softening (E_s) moduli are required. Lopez-Cela recommended a value for β between zero and α. The experimental test case SNL-16 was modeled iteratively in the MPM code to find appropriate values for the final three constants. These initial tests exhibited abnormalities with both standard dimensioned and normalized input that warranted further investigations into code behavior in the area of discretization and convergence. Input data was normalized with alternate measures for length, mass, and time in order to use density and stiffness values for both materials as close to 1.0 as possible with the goal of reducing the effect of any numerical error within the calculation. With standard dimensioned input data the DP constitutive subroutine would consistently diverge; normalized input data would allow the subroutine to converge, but generally with concrete response much stronger and stiffer than experimental results. The DP model implementation in the MPM code is comparable to that of other codes with the exception of hardening and softening which are not used in the same manner in other DP implementations (Lopez-Cela, 2002; Hallquist, 2006).

Table 18. DP Material Constants

		Conventional Strength
Mass		
Density	(lb*s^2/in^4)	2.04E+03
Strength		
E	(psi)	4.12E+06
Yield Stress	(psi)	2.57E+03
Ultimate Stress	(psi)	5.70E+03
α		0.78
β		0.77
Strain at f'c		0.002

4.4.3. Output Data

The output settings control which results files are activated and how often (in simulation time) those files are updated. Tabular output file options include position, velocity, acceleration, and stresses for material points and forces, momentum, and stresses over the grid. Many of these output options are difficult to interpret and apply to the impact and penetration problem, because region-specific data cannot be specified to inspect for example the acceleration of the projectile points separate from nearby target points. A separate position output can be produced at multiple timesteps in a format readable by the postprocessor, Tecplot, shown in Figure 26.

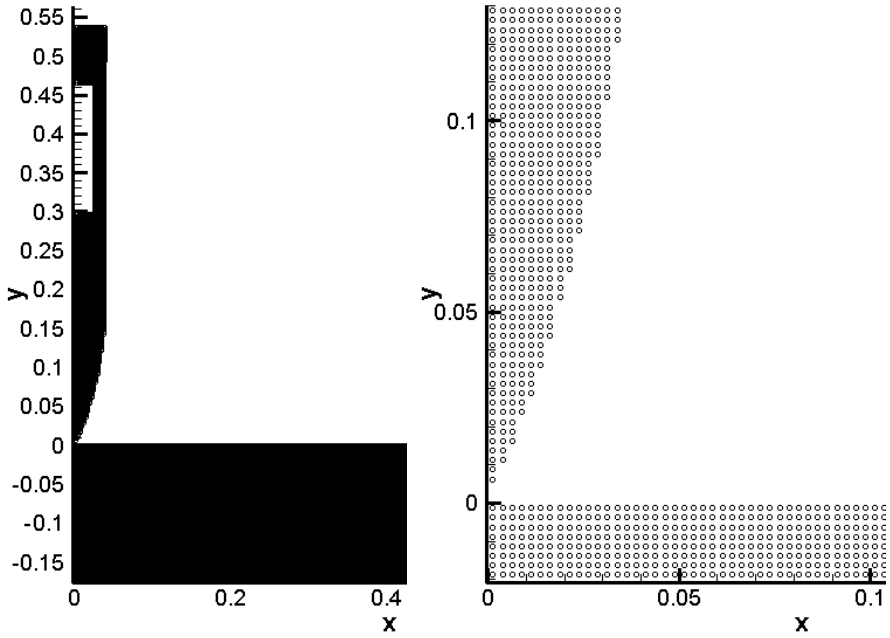

Figure 26. Tecplot Output Example: a) Full, b) Zoomed

4.4.4. Code Use

The abnormal results of the impact and penetration tests included decreases in material strength and elasticity with increased refinement and sticking of dissimilar material points. To further investigate these responses the Taylor Impact validation problem was run in MPM. The Taylor Impact problem is conducted by directly impacting a perfectly rigid boundary with a cylindrical bar of ductile material, typically metals, at a velocity resulting in partial plastic deformation to the bar, shown in Figure 27. The right side of the figure shows experimental results with plastic strain values ranging from 0.1 to 1.5, and the right side

shows the MPM results with highlighted material points with plastic strain values higher than 0.1.

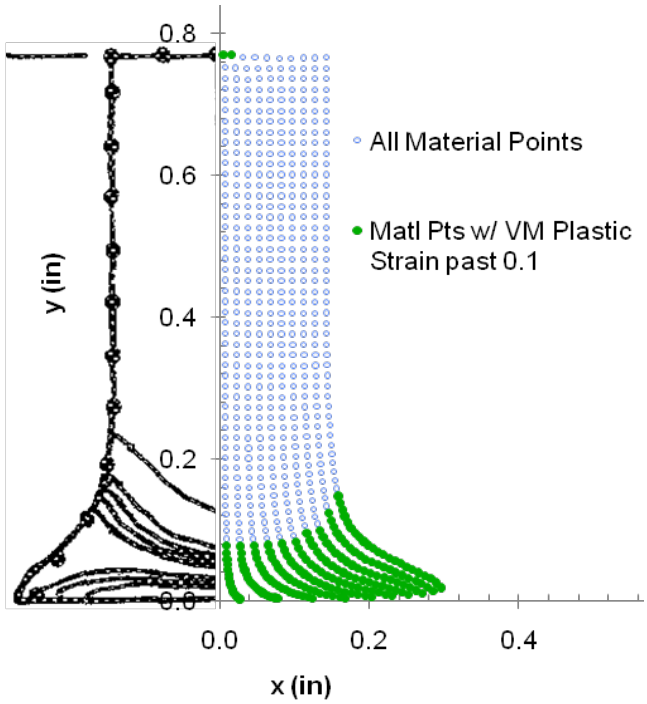

Figure 27. MPM Taylor Impact Example Results: Experimental (left)(Johnson & Holmquist, 1988) and Analytical (right)

The study compared an experimental final length and mushroom radius of an aluminum 6061 bar to MPM results with varying grid spacing, between 0.05 and 0.0056 in., and points per cell, between one and 36. The validation study, shown in Figure 28, found that while the MPM code could produce reasonable results for final length and mushroom radius, 1.8% and 3% average percent differences, respectively; the results were not convergent. As grid size

was decreased or points per cell were increased, the percent difference for the mushroom radius increased, instead of the solution approaching the experimental results. The final length appeared convergent for points per cell refinement, but reduction in grid size resulted in calculated final lengths above and then eventually below the experimental length. Irregular responses were observed such as sticking and strain accumulation in material points adjacent to the slip-free boundary condition which can be seen at the center of the top surface in Figure 27.

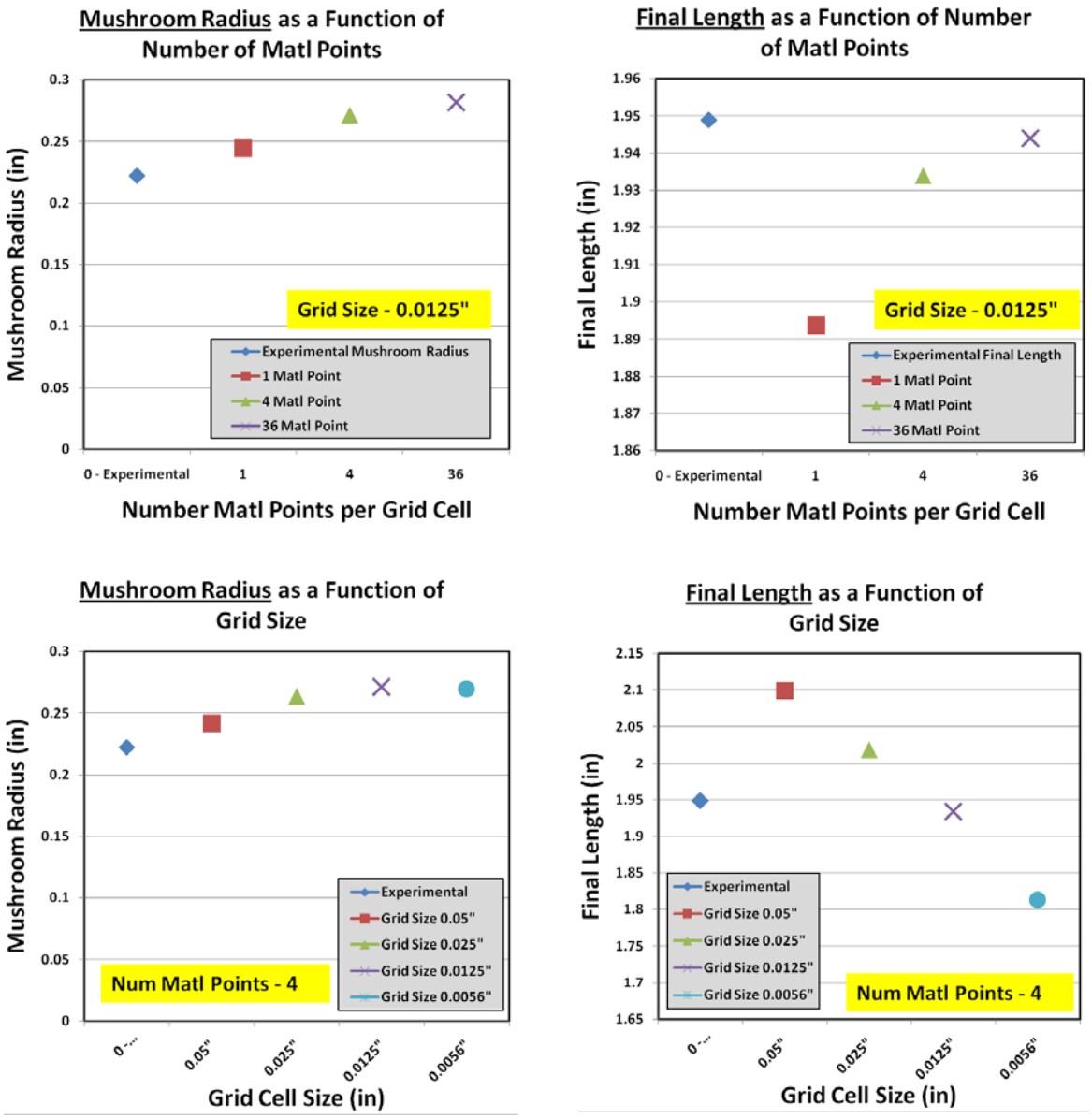

Figure 28. MPM Taylor Impact Validation Results

The developmental version of MPM used in this research provided the least user guidance and produced the most erroneous results of the analysis packages used. The MPM code is implemented in only two dimensions limiting calculations to symmetric boundary conditions and normal impact without inclination angles, and limited availability of material models. The specific implementation of the DP model in MPM produced erroneous results. The addition of advanced material models could improve the MPM code, but there seems to weakness with the main routine in this version. These problems are emphasized by the Taylor impact validation study where divergent results and odd behavior with boundary conditions were observed. The MPM code is still under development and currently exhibits abnormal response in concrete penetration problems, but was at least an order of magnitude faster in obtaining a solution than any other code tested.

5. Analysis Pairing Comparison Results

A two phase study was conducted to evaluate the pairings of analysis codes and concrete material models of this research, as shown in Table 19. A preliminary evaluation compared all analysis pairings against a single experimental validation impact test. A subsequent method comparison was conducted with the highest performing pairings of the preliminary evaluation with four experimental impact tests as validation.

Table 19. Analysis Matrix for Target Material Models

Analysis Program	Target Material Model				
	DP	HJC	KC	Osborn	BFK
EPIC		E-1		E-2	
LS-DYNA		L-1	L-2		
CTH		C-1			C-2
MPM	M-1				

DP - Drucker-Prager, HJC – Holmquist Johnson Cook,
KC – Karagozian and Case, BFK – Brittle Failure Kinetics

5.1. Preliminary Evaluation

Test SNL-16 of the Sandia experimental impact test series was used as validation in the preliminary evaluation. The test involved a 6.0 CRH projectile and a six ft. thick conventional strength target. The impact velocity of 1471 ft/sec resulted in a 39.02 in. penetration, 14,154 G peak deceleration, and 1.21% mass loss of the projectile. The validation test was chosen from the 15 test series because it represents an intermediate penetration depth with limited inclination angles. Additionally, no significant errors were experienced with experimental test conditions or data collection during test SNL-16.

The EPIC analysis code was used with three-dimensional tetrahedral meshes for the target and projectile consisting of 909,114 and 115,852 elements, respectively. Equivalent erosion strains were determined iteratively as 0.24 for HJC and 0.34 for Osborn. For the target boundary condition, 1871 nodes on the target were constrained in a saddle-type configuration.

LS-DYNA was run with three-dimensional hexahedron meshes for the target and projectile consisting of 151,592 and 8,160 elements, respectively. Equivalent erosion strains were determined iteratively as 0.15 and 0.10 for the HJC and K&C models, respectively. 5768 nodes on the target were constrained in a saddle-type configuration.

CTH was run with a three-dimensional Eulerian mesh containing 452,530 grid cells. For the target boundary condition, two rigid, static, rectangular prisms were fixed tangent to the surface of the target.

The MPM code was run in two dimensions with normalized input using alternate units for mass and time equal to 4.630E-4 lb-mass and 4831 seconds, respectively. The grid spacing for the x and y directions were 0.197 in., with four material points for each of 23,901 grid cells, totaling to 270,241 material points.

5.1.1. Penetration Depth

Penetration depth results showed significant disparity between EPIC and LS-DYNA versus the other methods, as shown in Figure 29. Penetration depth varied significantly between the two CTH material models; HJC (C-1) under predicted concrete resistance to penetration while BFK (C-2) only slightly over predicted it. The MPM code exhibited the most significant error percentage in penetration depth at 88.9%. The general success of the FEM codes at predicting penetration depth may be misleading as the iterative process by which erosion strains were determined was directly reliant on penetration depth of test SNL-16. As erosion is not necessary to avoid large mesh distortion in the remaining codes, CTH and MPM, they do not include such erosion methods and actual material models must be altered to fit them for the use with concrete impact and penetration.

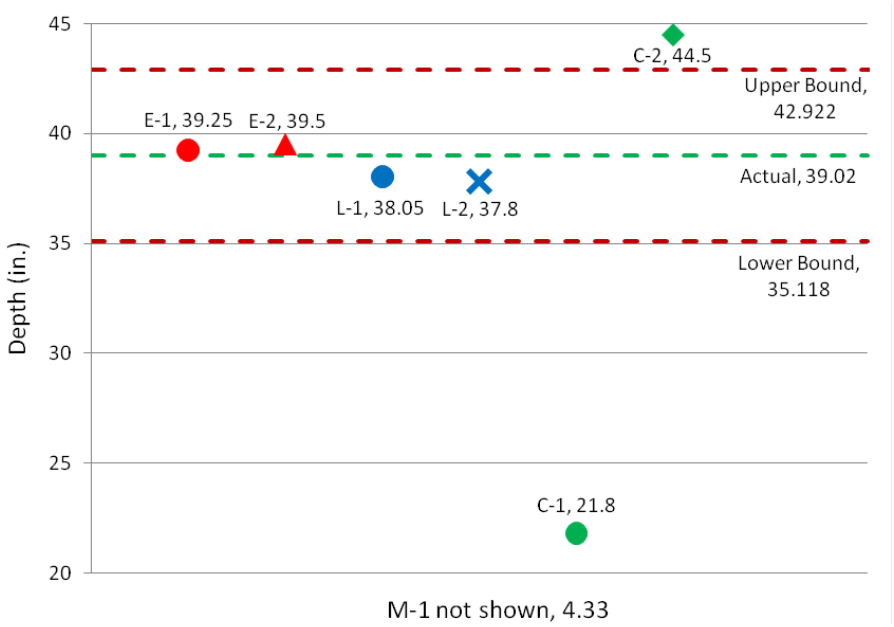

Figure 29. Penetration Depth for Preliminary Evaluation

5.1.2. Projectile Mass Loss

Projectile mass loss is not available in the CTH and MPM codes, and could not be extracted from other analysis results data. Between the remaining codes, projectile mass loss was most successfully predicted by the EPIC models, especially E-1 which fell within 35% of the experimental value. The LS-DYNA Johnson Cook (JC) model used for the steel projectile contained an internal erosion strain term which could not be modified and resulted in values higher than the experimental results.

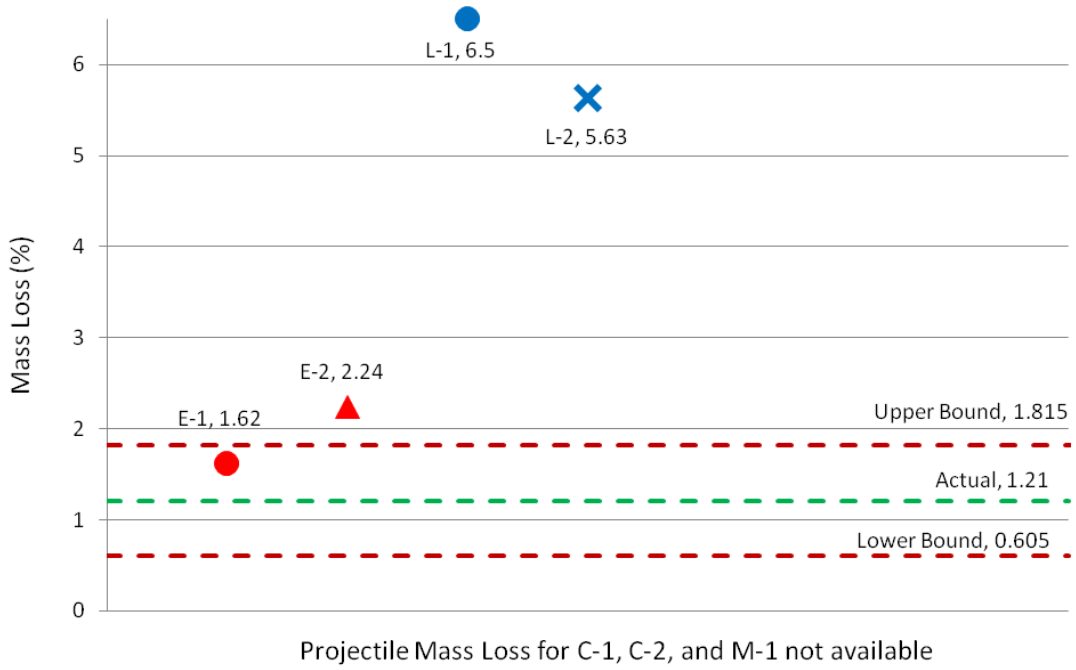

Figure 30. Projectile Mass Loss for Preliminary Evaluation

5.1.3. Deceleration

As previously mentioned in Section 3.3.4, the decelerations filtered by 5.0 kHz moving averages were compared by three features of the curve shown in Figure 31: peak deceleration, descending curve slope, and deceleration end time.

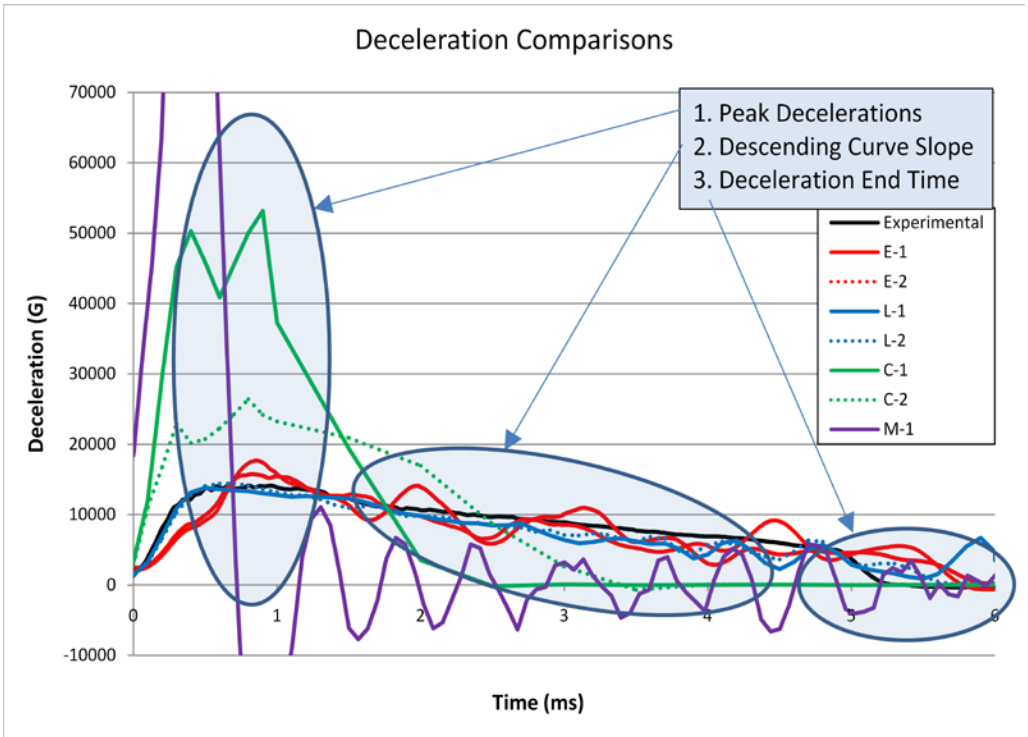

Figure 31. Deceleration Comparisons for Preliminary Evaluation

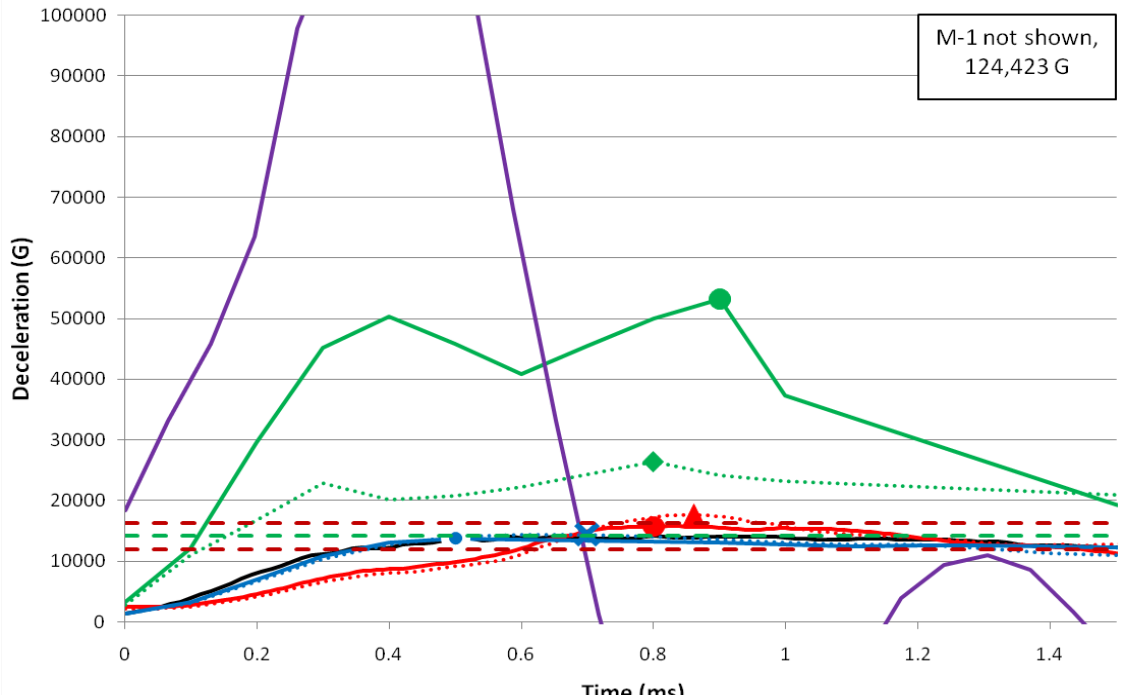

Figure 32. Peak Decelerations of the Preliminary Evaluation

The peak decelerations show significant distinction between the FEM and remaining codes. Figure 32 shows that the MPM code and both CTH models over predict peak deceleration. Interestingly, despite the fact that C-2 over predicted the penetration depth, it also over predicted the peak deceleration.

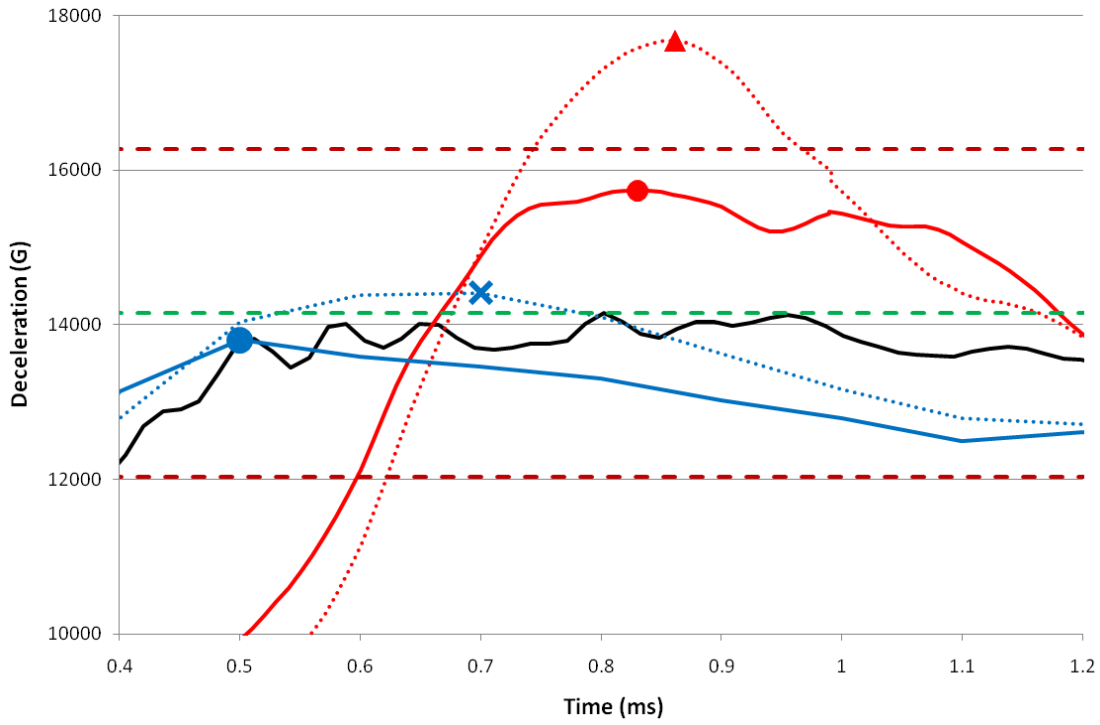

Figure 33. Peak Deceleration of FEM codes for Preliminary Evaluation

Figure 34 shows a closer view of the peak decelerations of the FEM codes. While the two EPIC models showed similar results for penetration depth, the Osborn model over predicted the peak deceleration by 24.9% compared to 11.2% over prediction for the HJC model. The LS-DYNA models provided highly accurate predictions for peak deceleration despite having less accurate predictions for penetration depth.

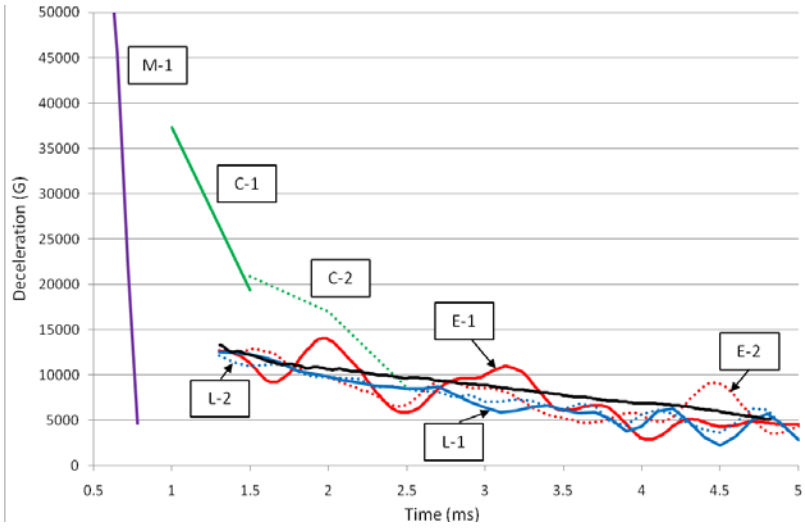

(a) Descending Slopes

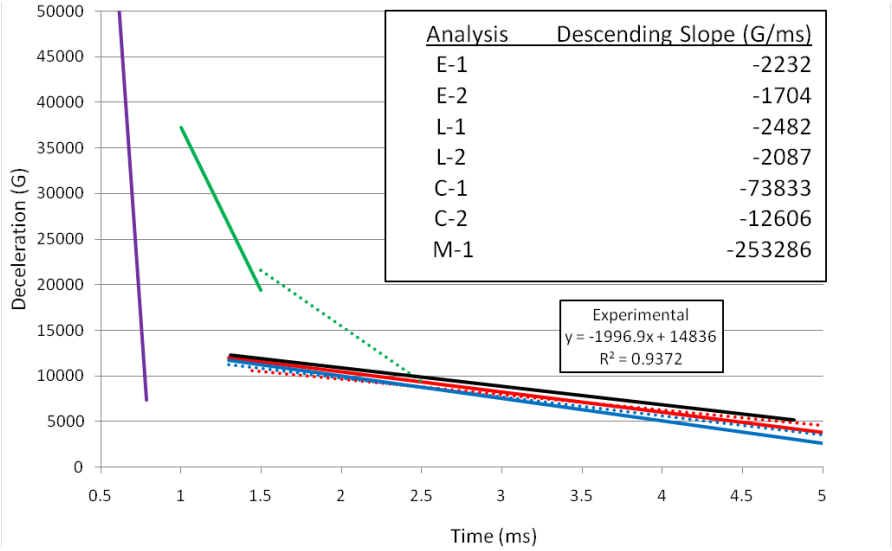

(b)Linear Trend Lines

Figure 34. Preliminary Evaluation Deceleration

Analysis Pairing Comparison Results

The experimental deceleration of this test featured a consistent, nearly linear descending slope following the peak deceleration. The CTH and MPM codes failed to capture this slope partially due to the extreme over predictions of the peak decelerations. Figure 34 a) shows that while the EPIC and LS-DYNA codes show some non-linearity for the descending curve, they generally follow the experimental results.

The linear trend lines in Figure 34 b) further demonstrate the dissimilarity in the deceleration descending slopes between the FEM and other codes. E-1, E-2, and L-2 exhibit the only linear fit slopes that fall within 20% of the experimental.

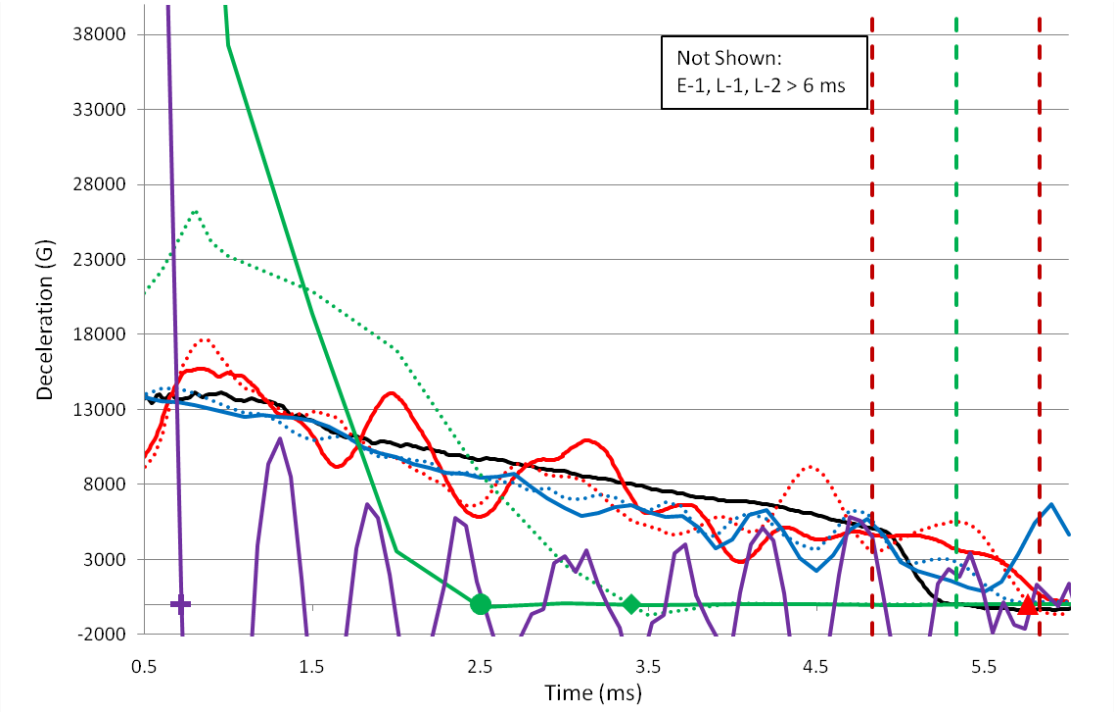

Figure 35. Deceleration End Time for Preliminary Evaluation

Analysis Pairing Comparison Results

The FEM codes predicted slightly greater, but generally more accurate deceleration end times than did MPM and CTH. The end of the deceleration curve for MPM shows a reverberation also observed in analytical plots as an indication that the concrete material was too ductile. This resulted in sticking of the projectile to the target so that contact was maintained when the projectile was exiting the target.

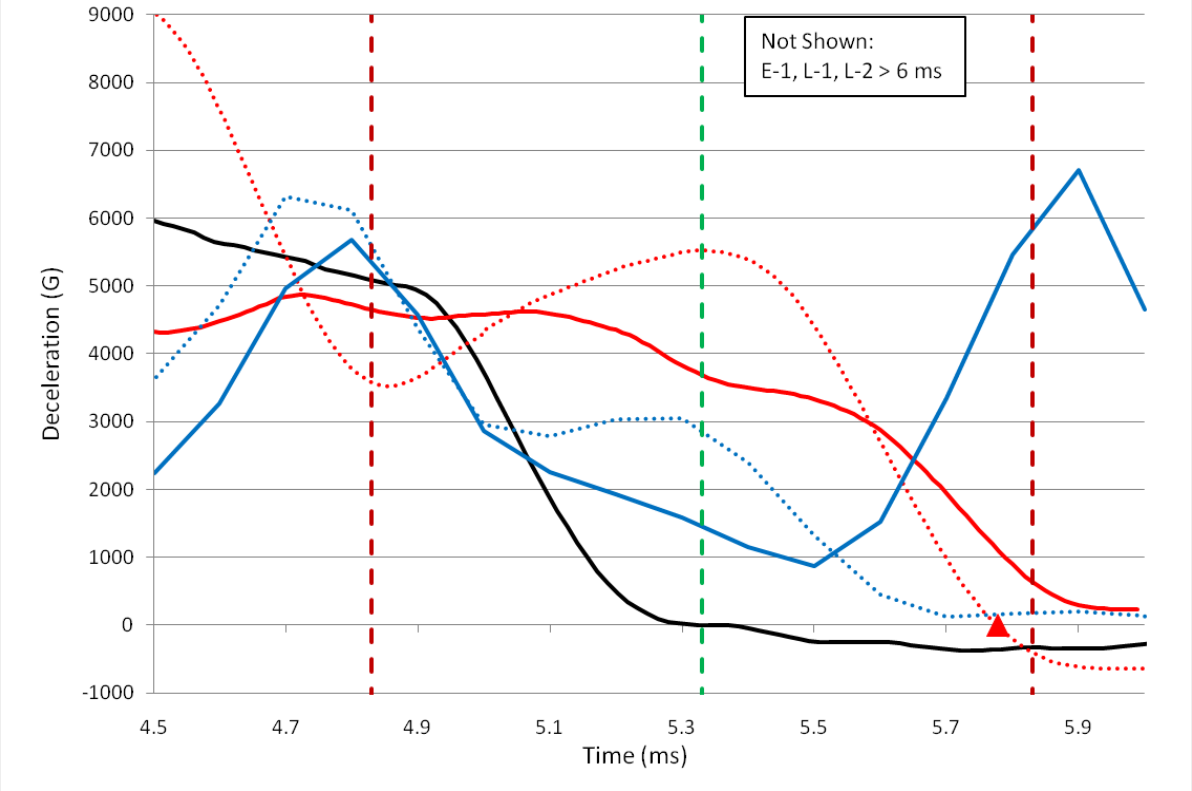

Figure 36. Deceleration End Times of FEM Codes for Preliminary Evaluation

Analysis Pairing Comparison Results

EPIC and LS-DYNA over predict the experimental deceleration end time, and three of the four ran longer than the allotted simulation time equal to 0.5 ms beyond the experimental time. However, it does appear the deceleration end times for the FEM codes falls much nearer to the experimental results than do the much shorter MPM and CTH calculations. E-2 is the only model that falls within 0.5 ms of the experimental results.

Table 20. Deceleration Grading for Preliminary Evaluation

Model	Effective Maximum (G)	Descending Curve Slope (G/ms)	End Time (ms)	Maximum Deceleration Grade	Descending Curve Grade	End Time Grade	Total Deceleration Grade
E-1	15738	-2232	>6	1	1	0	**2**
E-2	17673	-1704	5.8	0	1	1	**2**
L-1	13800	-2482	>6	1	0	0	**1**
L-2	14411	-2087	>6	1	1	0	**2**
C-1	53164	-73833	2.5	0	0	0	**0**
C-2	26393	-12606	3.4	0	0	0	**0**
M-1	124490	-253286	0.7	0	0	0	**0**
Upper	16274	-2404.1	5.8	-	-	-	**-**
Exp.	14151	-2003	5.3	-	-	-	**-**
Lower	12029	-1602.7	4.8	-	-	-	**-**

The analytical deceleration curves revealed significant advantages with the four FEM codes. While no model perfectly matched the experimental deceleration curve, only the CTH and MPM models were unable to match any of the three deceleration features.

5.1.4. Modeling Feature Capabilities

The ability of each analysis pairing to account for the damage, apply accurate boundary conditions, and specify accurate inclination angles through three-dimensional analysis were considered in the preliminary evaluation. Absence of these features limits the overall quality of the results and comparisons. Damage is included in all but two concrete models in the preliminary evaluation, Osborn (E-2) and DP (M-1). The application of accurate boundary conditions to the target is not available in CTH and MPM. Only EPIC and LS-DYNA allow for the saddle-type constraint from the experimental tests to be applied. The limitation of the MPM code to two-dimensions reduces all impact analyses to perfectly direct without inclination.

5.1.5. CPU Run Time

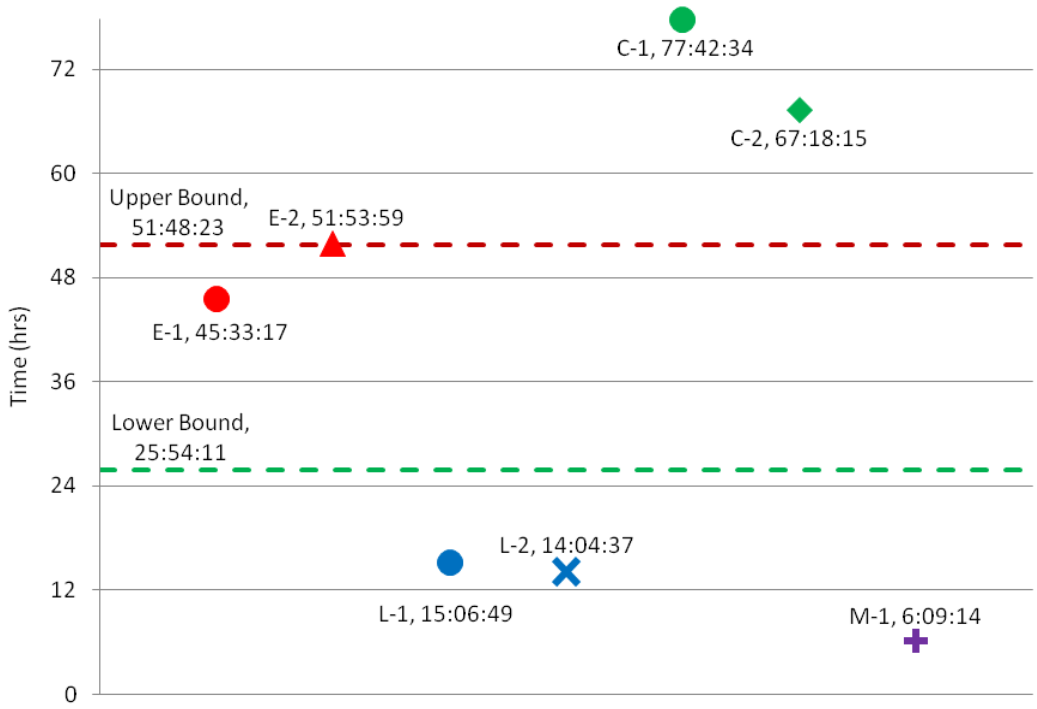

Figure 37. CPU Run Time for Preliminary Evaluation

EPIC and LS-DYNA calculations were each performed in series on a single 2.6 GHz processor, and MPM calculations were performed in series on a single 3.0 GHz processor. Calculations of CTH were performed in parallel on four 2.6 GHz processors. By ratios of processor size and number, CPU run times were normalized to a single 2.6 GHz processor for the comparison shown in Figure 37. The MPM code performed in the shortest time, largely because it is a two-dimensional code, and further refinement did not show improvements in results.

5.1.6. Conclusions

Table 21. Preliminary Evaluation Grading

Model	Penetration Depth	Projectile Mass Loss	Deceleration	Damage	Boundary Condition	Dimensions	RunTime	Total
E-1	1	1	2	1	1	1	1	**8**
E-2	1	0	2	0	1	1	0	**5**
L-1	1	0	1	1	1	1	2	**7**
L-2	1	0	2	1	1	1	2	**8**
C-1	0	0	0	1	0	1	0	**2**
C-2	0	0	0	1	0	1	0	**2**
M-1	0	0	0	0	0	0	2	**2**
Total Possible	**1**	**1**	**3**	**1**	**1**	**1**	**2**	**10**

Based on the grading system shown in Table 21, EPIC and LS-DYNA performed significantly better than CTH and MPM in the analysis of SNL-16. MPM was not found to be convergent and the Drucker-Prager (DP) model could not be adequately fit for the concrete material constants. These two factors limited the use of the developmental code and caused the significantly erroneous results. However, it should be considered that if CTH and MPM contained features similar to element erosion to fit appropriate levels of penetration, then much more accurate results may be achieved. Additionally the MPM implementation used in this preliminary evaluation is in the early stages of development, and exhibited abnormalities that might not be seen in further developed MPM codes.

5.2. Method Comparison

In order to further evaluate the four most successful analysis configurations in the preliminary evaluation, a second method comparison was conducted. The performance of analysis pairs was evaluated based on the analysis of four experimental impact tests using the same grading system as the preliminary study. The validation tests were selected to vary the concrete strength, projectile shape, and impact velocity in order to observe trends in analytical accuracy.

The EPIC analysis code was run with three-dimensional tetrahedral meshes containing 909,114 target elements; the 3.0 CRH and 6.0 CRH projectiles contained 121,347 and 115,852 elements, respectively. Erosion strains that were determined for the concrete material models in the preliminary evaluation were used for both concrete strengths in the second method comparison. For the target boundary condition, 1871 nodes on the target were constrained in a saddle-type configuration.

The LS-DYNA analysis code was run with three-dimensional tetrahedral meshes containing 151,592 target elements; the 3.0 CRH and 6.0 CRH projectiles contained 15,392 and 8,160 elements, respectively. Again, the erosion strains that were determined for the concrete material models in the preliminary evaluation were used for both concrete strengths in the second method comparison. 5768 nodes on the target were constrained in a saddle-type configuration.

5.2.1. Penetration Depth

The penetration depth results in Figure 38 show that both L-1 and L-2 more accurately predict penetration depth for the four tests. All four codes reasonably modeled penetration in the conventional strength tests, but the tests with lower strength concrete showed more error in analytical results. For the low strength concrete tests, the LS-DYNA analyses produced penetration depth with a 12.9% error average while E-1 and E-2 averaged 29.6% error. LS-DYNA models reasonably predict all four tests with the exception of SNL-7 which involved a low strength concrete and the more slender 6.0 CRH nose shape projectile. Within the analysis codes material model results varied slightly. The HJC pairs, E-1 and L-1, performed better than the alternate material models with 15.7% and 7.5% respective error versus the 16.3% and 9.0% error of E-2 and L-2, respectively. It is possible to suggest from the penetration depth results that the analysis pairs only performed well for experimental tests that resulted in penetration depths similar to that of SNL-16, by which the material model erosion strains were determined.

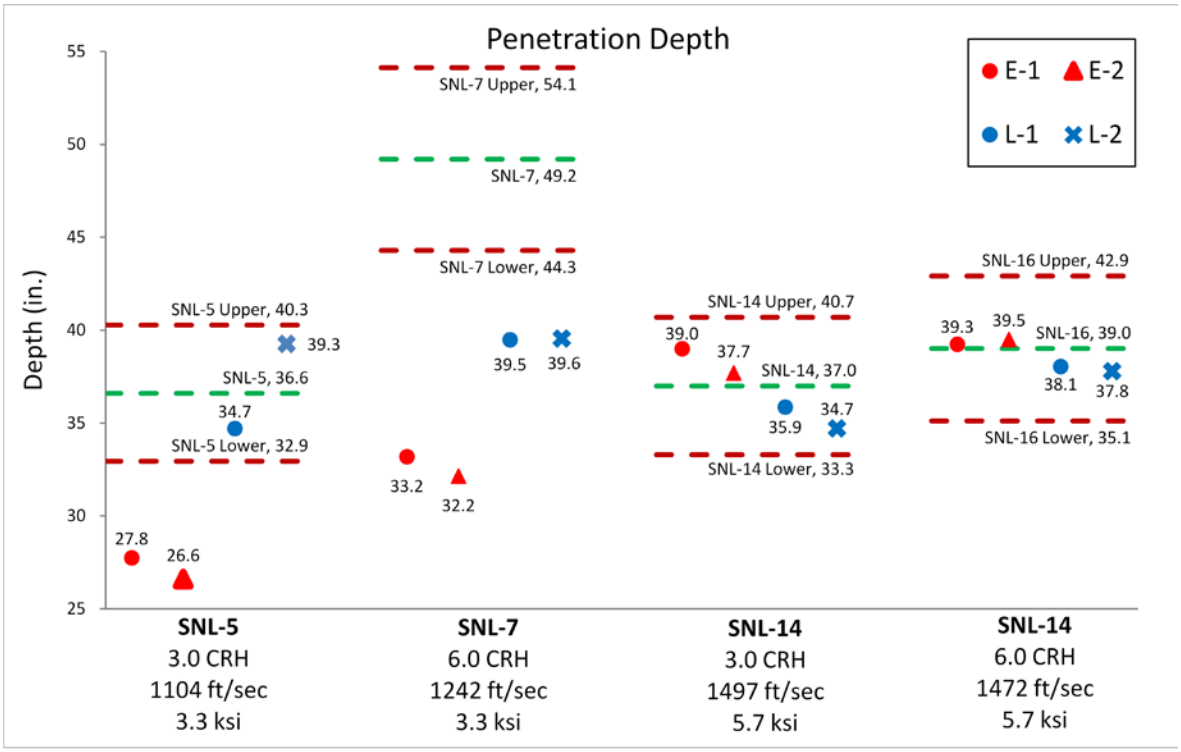

Figure 38. Penetration Depth for Method Comparison

5.2.2. Projectile Mass Loss

Projectile mass loss for the method comparison maintains observations of the EPIC and LS-DYNA pairings in the preliminary evaluation. LS-DYNA was less able to predict accurate levels of projectile mass loss possibly due to the internal calculation of failure strain in the JC model. This calculation is possibly erroneous or, more likely, not designed specifically for impact forces in this experimental range. Within each code, values for projectile mass loss only varied slightly between the material models, likely because the

erosion of the projectile is heavily dependent upon the projectile material model which was the same for analyses within each code. The EPIC results show more accurate values for projectile mass loss in the tests with low strength concrete and lower impact velocities.

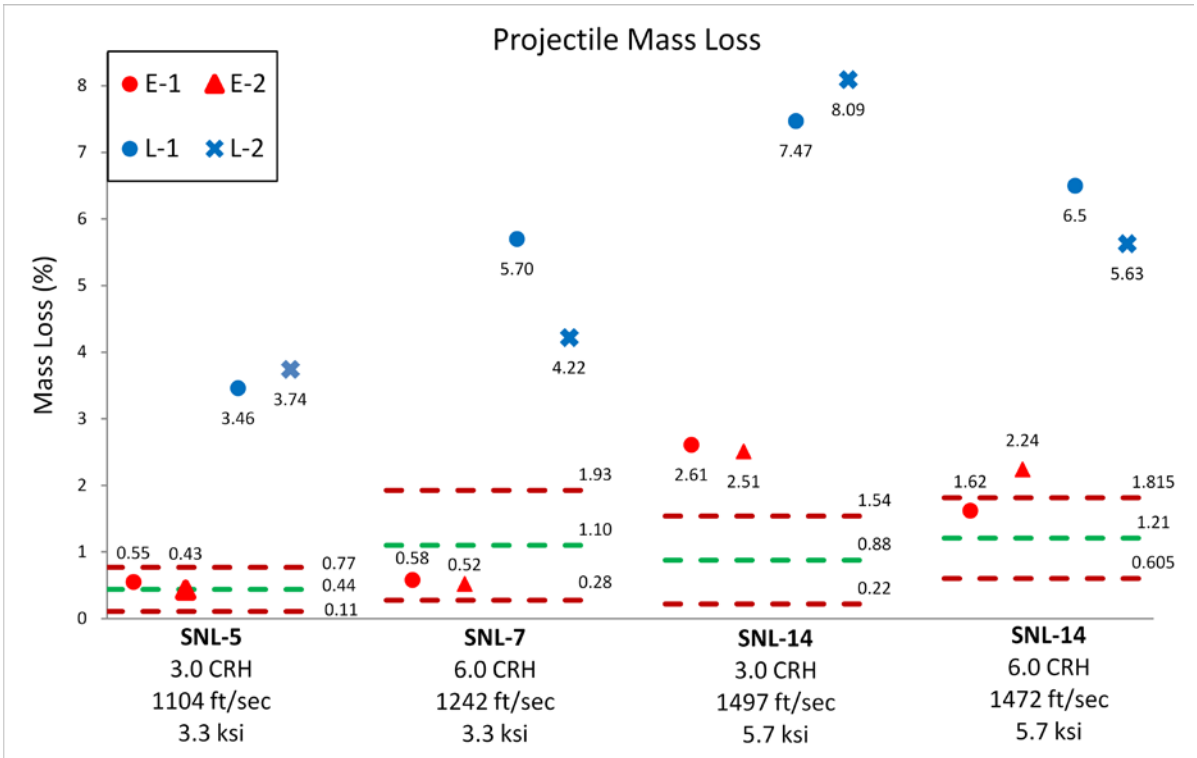

Figure 39. Projectile Mass Loss for Method Comparison

5.2.3. Deceleration

Experimentally, the two impact tests with lower strength concrete, SNL-5 and SNL-7, show different deceleration curve features than the conventional strength concrete tests in

Figure 40. In the conventional strength concrete tests, deceleration curves exhibit distinct maximum points and descending slopes; however, this distinction is not observed with the low strength concrete tests which exhibit nearly constant deceleration. For consistency of grading, the deceleration will be treated by the three regions of peak, descending slope and end time as in the preliminary study. However, for the low strength concrete the peak deceleration will be determined only from values in the first two ms, and, while the slope of the experimental curves may not actually descend, it will be determined in the same manner as previously described in Section 3.3.4.

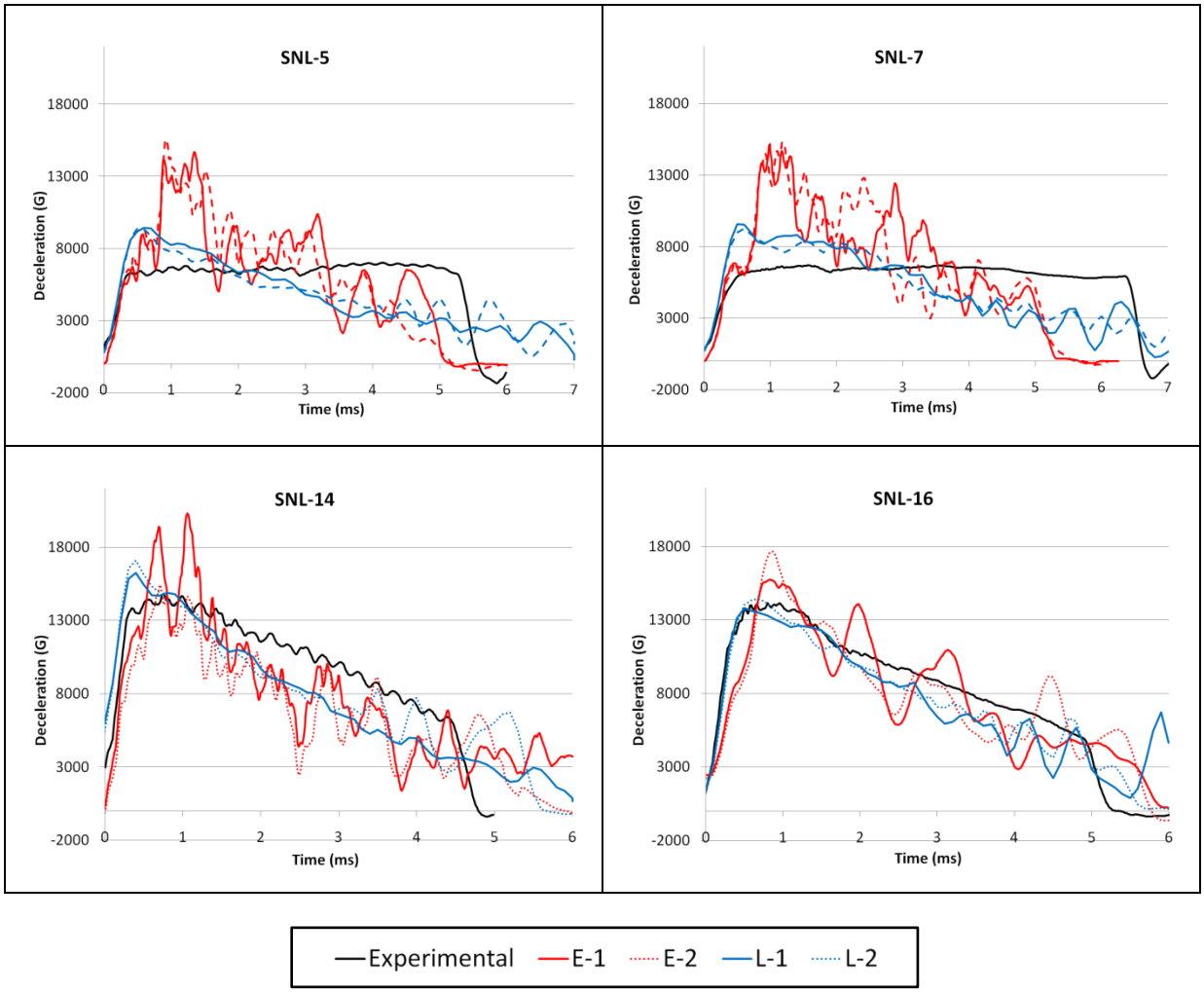

Figure 40. Decelerations for the Method Comparison

The peak deceleration plots in Figure 41 show that the numerical results, especially E-1 and E-2, generally contain a higher intital peak deceleration than the experimental results. While the high initial peak is an observed feature in the experimental decelerations with conventional strength concrete, it absent in the low strength concrete tests. LS-DYNA

models do not show the high initial peak as definitively as EPIC pairings, but the feature is still present. For all four tests, LS-DYNA more closely reproduces the initial levels of deceleration.

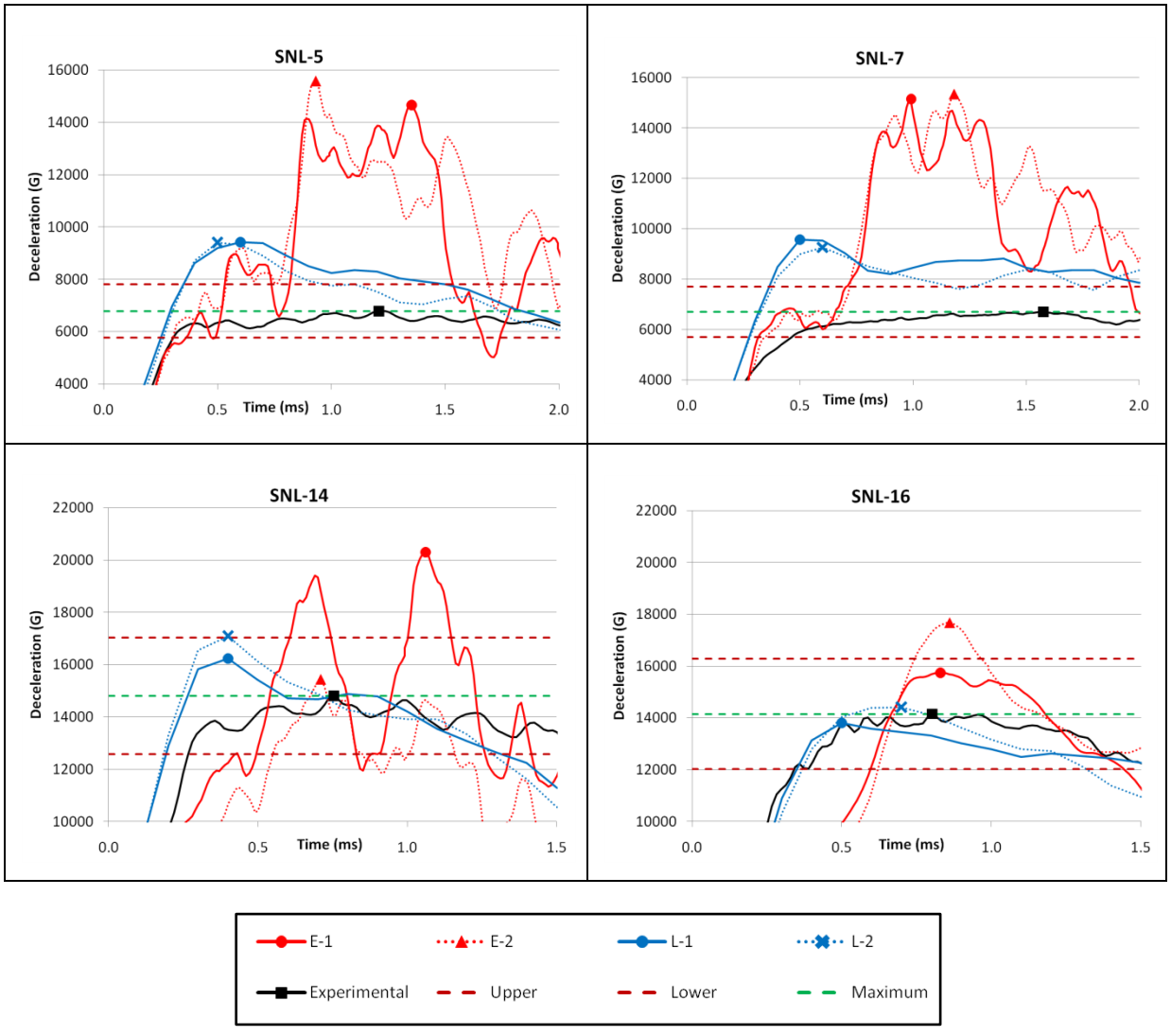

Figure 41. Peak Deceleration for the Method Comparison

Analysis Pairing Comparison Results

The descending curve portions of the decelerations are shown in Figure 42 without the linear trend lines. Experimentally, dramatic difference exists between the low and conventional strength concrete test descending slopes. These distinct responses indicate that as strength of concrete target reduces the resistance to penetration more closely resembles that of a fluid where drag is applied to the projectile. This response would especially be true as the ratio between impact pressures and concrete strength increases beyond the range of the experimental test series. Analytically, the four analysis pairings reasonably match the descending slopes of the two experimental tests with conventional strength concrete but failed to predict the flatter slopes of the low strength concrete tests.



Figure 42. Deceleration Descending Slopes for Method Comparison

The trend line slopes and bounding values are given in Table 22. The experimental low strength concrete tests are both nearly constant while the conventional strength slopes are on the order of -2000 G/ms. The linear trend slope of test SNL-7 is even a positive value of 158 G/ms. The analytical descending slopes for the low strength concrete tests show that the LS-

DYNA pairs exhibit descending slopes that more closely match the experimental curves, but, in general, all four models produce descending curves with too much inclination.

Table 22. Deceleration Descending Slope Linear Trend Lines for Method Comparison

Analysis	Bounding Region (ms)		Slope (G/ms)
	Beginning	End	
SNL-5			
E-1	1.85	4.66	-1576
E-2	1.43	4.74	-2576
L-1	1.10	6.50	-1167
L-2	1.00	6.50	-1050
Actual	**1.71**	**5.07**	**158**
SNL-7			
E-1	1.49	5.15	-1806
E-2	1.68	5.10	-2111
L-1	1.00	7.00	-1599
L-2	1.20	7.00	-1414
Actual	**2.07**	**6.13**	**-188**
SNL-14			
E-1	1.56	5.50	-1966
E-2	1.21	5.42	-1806
L-1	1.00	5.50	-2549
L-2	0.90	4.90	-2348
Actual	**1.26**	**4.30**	**-2346**
SNL-16			
E-1	1.30	5.41	-2230
E-2	1.44	5.26	-1702
L-1	1.30	5.50	-2472
L-2	1.30	5.40	-2098
Actual	**1.31**	**4.82**	**-2003**

Figure 43 shows that all four analysis pairings over predict the deceleration end times for conventional strength concrete tests. Compared to the low strength concrete tests, E-1 and E-

2 exhibit early deceleration end times while L-1 and L-2 show much longer decelerations. All analyses were allowed to run at least 0.5 ms beyond the experimental, and some results showed decelations that extended past the experimental deceleration end. The early EPIC deceleration end times may indicate that the concrete material is being modeled too strong, which could possbily stem from the selection of erosion strain by a conventional strength test. However, the LS-DYNA erosion strain values for the low strength concrete were also obtained using a conventional strength test, and the L-1 and L-2 end times extend beyond the experimental results for the low strength concrete tests. The different analytical respsonse between EPIC and LS-DYNA deceleration end time could be dependent upon different element types or mesh configurations.

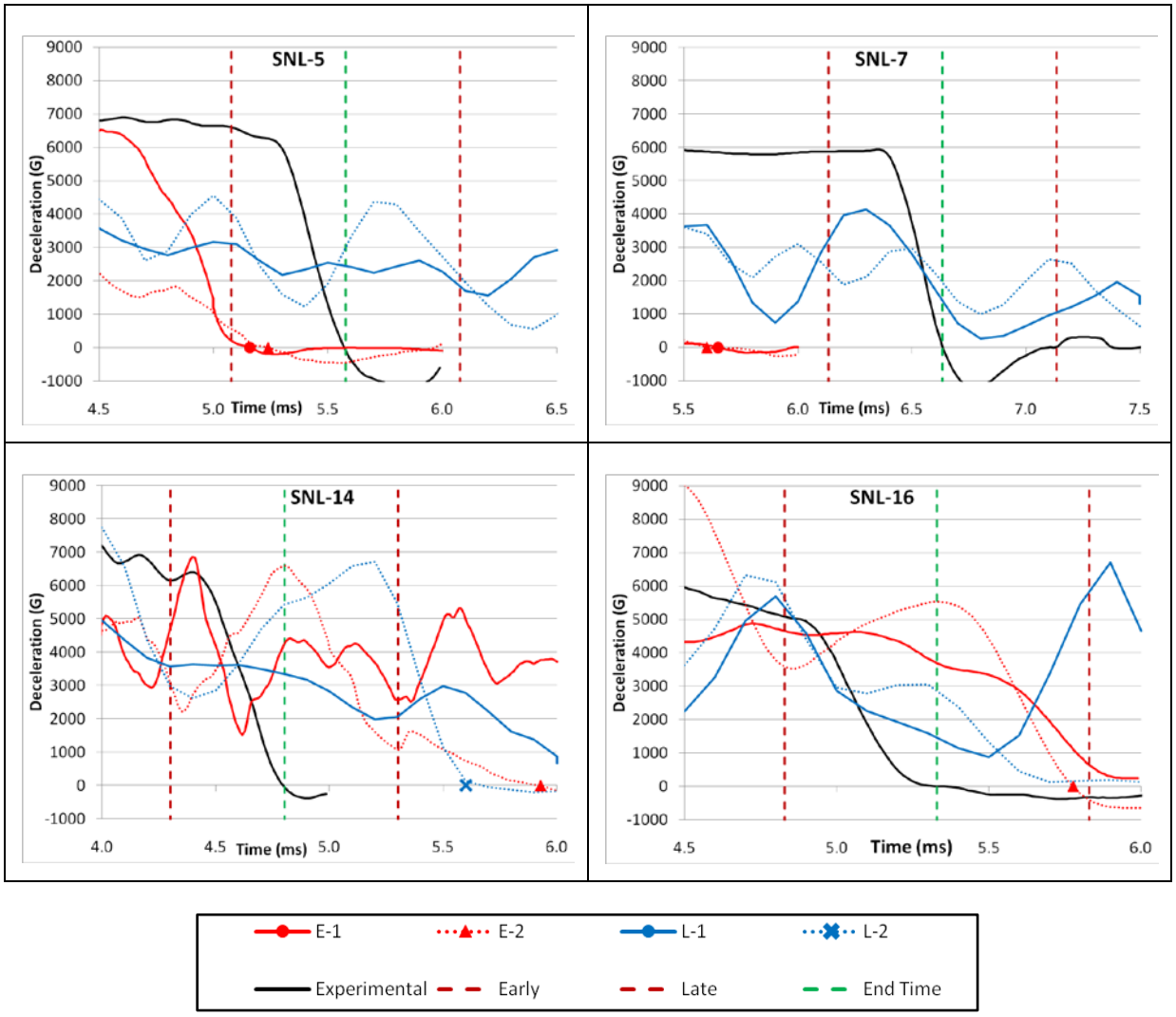

Figure 43. Deceleration End Times for the Method Comparison

Table 23. Deceleration Grading for the Method Comparison

Analysis	Maximum Deceleration (G)	Descending Curve Slope (G/ms)	Deceleration End (ms)	Maximum Deceleration Grade	Descending Curve Grade	Deceleration End Grade	Total Deceleration Grade
SNL-5							
E-1	14663	-1576	5.16	0	0	1	**1**
E-2	15573	-2576	5.24	0	0	1	**1**
L-1	9413	-1167	>6.50	0	0	0	**0**
L-2	9401	-1050	>6.50	0	0	0	**0**
Actual	**6783**	**158**	**5.58**	-	-	-	-
SNL-7							
E-1	15153	-1806	5.65	0	0	0	**0**
E-2	15338	-2111	5.60	0	0	0	**0**
L-1	9562	-1599	>7.50	0	0	0	**0**
L-2	9259	-1414	>7.50	0	0	0	**0**
Actual	**6692**	**-188**	**6.63**	-	-	-	-
SNL-14							
E-1	20302	-1966	>6.00	0	1	0	**1**
E-2	15422	-1806	5.91	1	0	0	**1**
L-1	16238	-2549	>6.00	1	1	0	**2**
L-2	17091	-2348	5.60	0	1	0	**1**
Actual	**14807**	**-2346**	**4.80**	-	-	-	-
SNL-16							
E-1	15738	-2230	>6.00	1	1	0	**2**
E-2	17673	-1702	5.78	0	1	1	**2**
L-1	13800	-2472	>6.00	1	0	0	**1**
L-2	14411	-2098	>6.00	1	1	0	**2**
Actual	**14154**	**-2003**	**5.33**	-	-	-	-

Table 23 further summarizes the deceleration data for the grading system. Analysis pairs with deceleration end times not reached within the alloted time were shown to be greater than

the limiting simulation time. The overall observation from the deceleration table is the dificiency of the four analysis pairings to predict the deceleration curves for the low strength concrete tests.

5.2.4. Modeling Feature Capabilities

All four analysis pairings used in the method comparison are three-dimensional with the ability to accurately input impact inclination and saddle-type boundary constraint of the target. Only E-2 had no availability of damage modeling for the concrete material.

5.2.5. Run Time

The computational run times are summarized in Table 24. EPIC calculations consistently run longer than LS-DYNA with little difference between the HJC and Osborn model run times. LS-DYNA run times were more variable between the test curves and the HJC model calculations finish significantly quicker than that of the K&C model with the exception of SNL-16. The LS-DYNA calculation times for SNL-7 are particularly interesting in that they represent the shortest L-1 run time and longest L-2 run time.

Table 24. Method Comparison Run Times

Analysis	SNL-5	SNL-7	SNL-14	SNL-16	Average
E-1	59:07:41	51:52:01	61:55:36	45:33:17	**54:37:09**
E-2	47:36:00	52:44:32	62:00:23	51:53:59	**53:33:43**
L-1	20:32:46	9:05:40	12:40:24	15:06:49	**14:21:25**
L-2	52:43:23	61:31:27	24:57:24	14:04:37	**38:19:13**

5.2.6. Conclusions

Using the grading system from the preliminary evaluation, the method comparison showed that the HJC analysis pairings are slightly more effective than the other options in each analysis code. Between the codes, LS-DYNA is shown to outperform EPIC particularly in the areas of run time and penetration depth prediction. The L-1 pairing performed best out of the four configurations and received the grade of 25 out of a possible 40.

Table 25. Method Comparison Grading

Model	Penetration Depth	Projectile Mass Loss	Deceleration	Damage	Boundary Condition	Dimensions	RunTime	Total
E-1	2	3	4	4	4	4	0	**21**
E-2	2	2	4	0	4	4	0	**16**
L-1	3	0	3	4	4	4	7	**25**
L-2	3	0	3	4	4	4	3	**21**
Total Possible	**4**	**4**	**12**	**4**	**4**	**4**	**8**	**40**

The method comparison showed a significant deficiency of all pairings to accurately model low strength concrete impact tests. One possible cause for the inaccurate response was

the implementation of eroding contact for the concrete models. The method used to iteratively determine the erosion strain for both low and conventional strength material models was based upon the penetration depth of a single conventional strength experimental test, SNL-16. Therefore, it was reasonable to suspect that the primary cause for the poor analytical results for the low strength concrete was the improper determination of erosion strain. For the experimental parameter study a new erosion strain was determined for the low strength concrete material model based upon the penetration depth from a low strength experimental test, SNL-7.

Due to the availability of multiple licenses for the EPIC analysis code, the E-1 analysis pairing was selected to perform the experimental parameter evaluation. While license availability was not a measure used in the grading system, it did allow for multiple analyses to be run simultaneously which was particularly important to iteratively determine the new value of erosion strain for the low strength concrete material model and to run the additional 12 test cases for the experimental parameter study.

6. Experimental Parameter Study

The sensitivity study of a single analysis pairing to various experimental parameters was studied using the full series of Sandia impact tests. The goal of the study was to understand the ability of the analytical method to capture trends apparent in the experimental test series results. The EPIC code and HJC model were selected for the experimental parameter study because this code-model combination was shown to be proficient in the preliminary evaluation and method comparison, and because of the availability of a floating license for the EPIC code, allowing for multiple analyses to be performed simultaneously on multiple processors. Also, as discussed in Section 5.2.6, the analytical performance for low strength concrete impact tests could be reassessed with a revised erosion strain for the low strength concrete implementation of the HJC model.

The EPIC analysis code was run with three-dimensional tetrahedral meshes containing 458,621 and 909,114 elements for the four ft. and six ft. thick targets, respectively; the 3.0 CRH and 6.0 CRH projectiles contained 121,347 and 115,852 elements, respectively. Erosion strain for the conventional strength concrete model was determined in the preliminary evaluation study to be 0.240 using penetration depths from experimental test SNL-16. For the experimental parameter study, a revised erosion strain for the low strength concrete model was determined to be 0.168 using experimental test SNL-7. Figure 44 shows a subset of trial analyses used to find the appropriate low strength concrete erosion strain. For

the target boundary condition, 4143 and 1871 nodes on the target were constrained in a saddle-type configuration for the four ft. and six ft. thick targets, respectively.

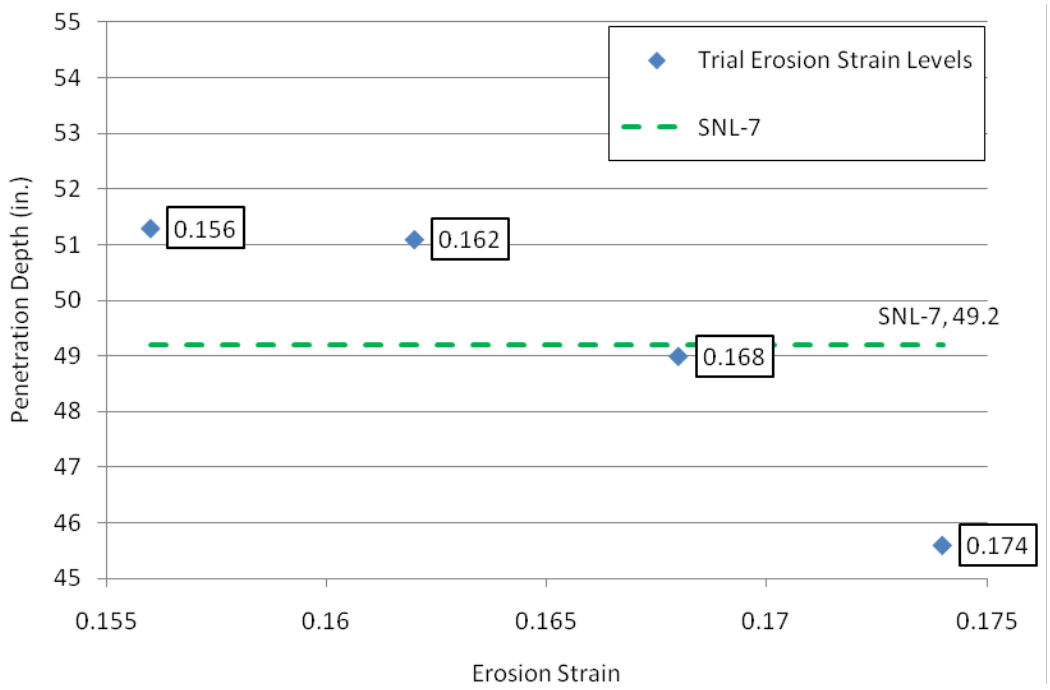

Figure 44. HJC Low Strength Erosion Strain Determination

6.1. Penetration Depth

Initial observations of penetration results in Figure 45 and Figure 46 show that overall the E-1 analysis pairing calculates accurate values of penetration depth throughout the velocity range of the experimental test series. The largest percent error is 33% for low strength concrete tests and 34% for the conventional strength concrete tests. The test cases, SNL-7 and SNL-16, used for erosion strain determination are exceptionally accurate due to the

iterative procedure to calibrate the concrete material models for the E-1 analysis pairing. Generally, test cases with the largest penetration depths were best modeled by the E-1 code. This is because the two test cases used for determining erosion strain, SNL-7 and SNL-16, represented the largest penetration depths in the low and conventional strength concrete tests, respectively.

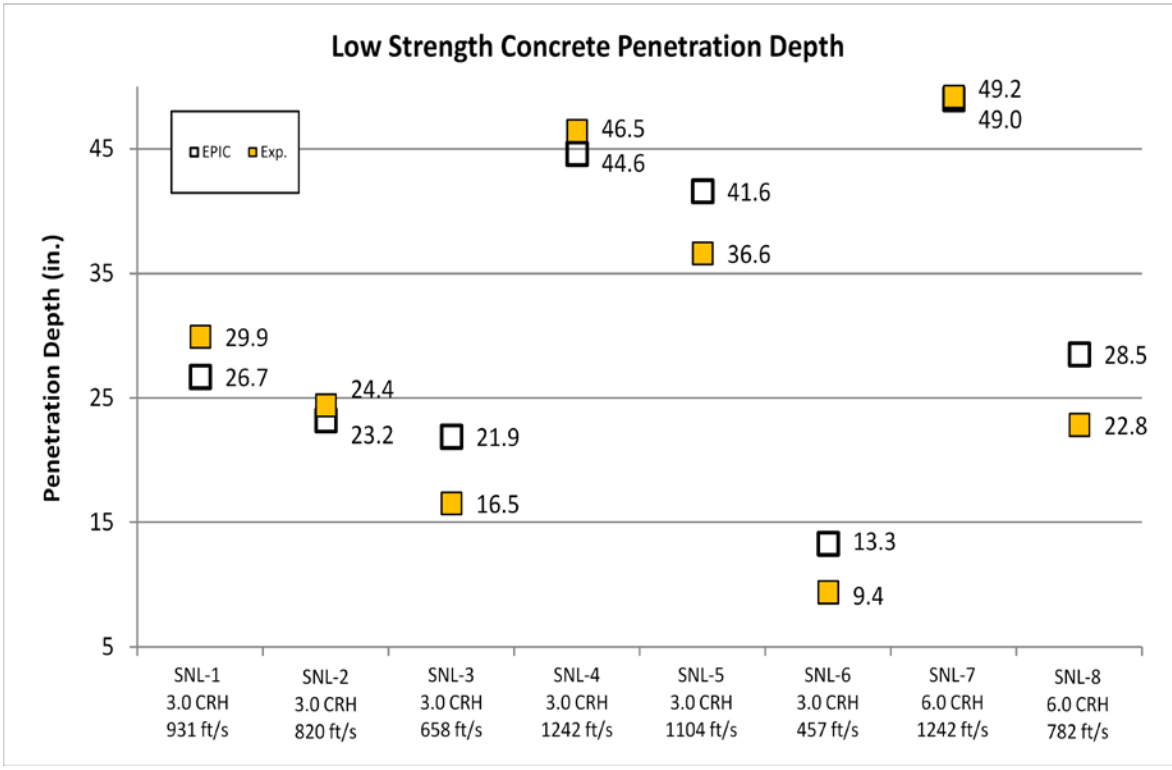

Figure 45. Penetration Depth for Low Strength Concrete Targets

Different analytical trends were observed between low and conventional strength concrete targets with respect to target depth. Low strength concrete analyses for the four ft.

target tests, SNL-1 and SNL-2, contained only 7.9% error for penetration depth compared to the 19.5% error for the six foot targets. Analytical penetration depth results for conventional strength concrete showed 31.0% error for four ft. target tests, SNL-9, SNL-10, and SNL-11, and only 11.2% for the six ft. target tests. The difference in the effect of target thickness on analytical penetration depth accuracy shows that accuracy is highest for low strength HJC implementations in thinner targets and for conventional strength HJC implementations in thicker targets. This trend may be linked to the lower impact velocities and subsequent shorter duration penetration events that are required in experimental testing for thinner targets. The low strength HJC implementation may perform better in cases where the event is shorter and less elements are eroded or inaccuracies in penetration depth may not be as obviously observed for the shorter duration events.

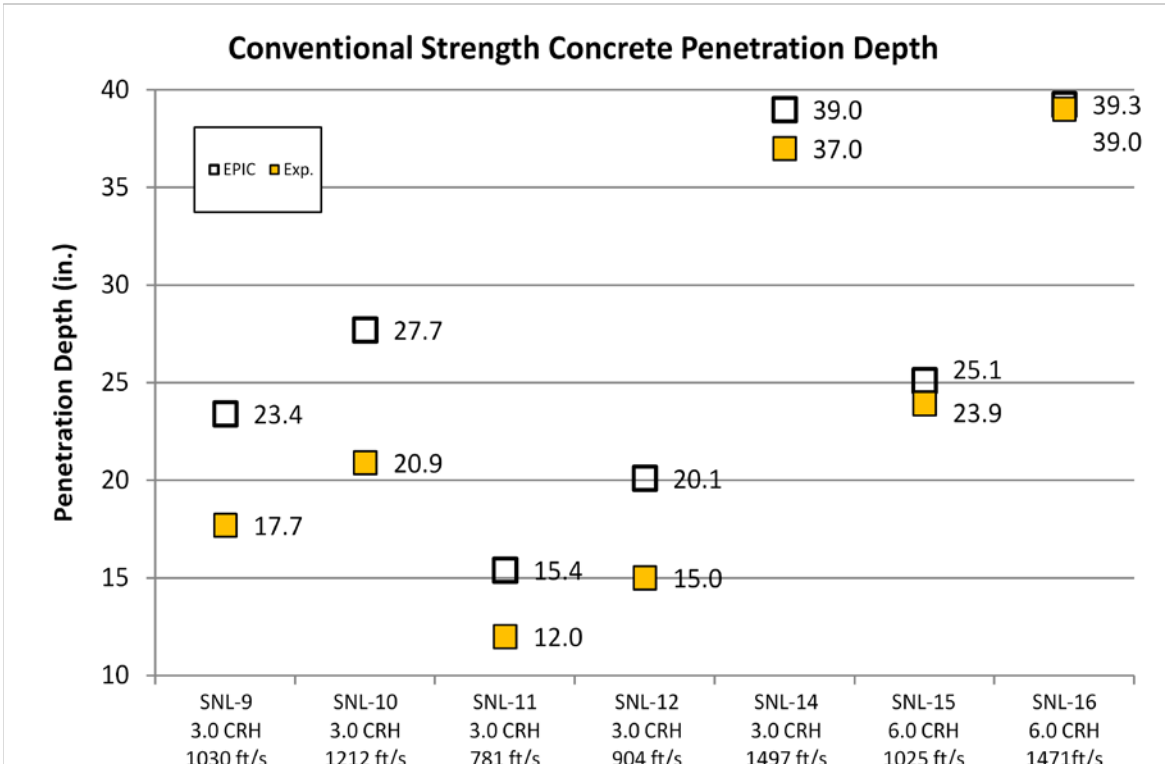

Figure 46. Penetration Depth for Conventional Strength Targets

Initial kinetic energy is an alternate method for comparing the results for penetration depth. Two distinct experimental trends are shown in Figure 47 for the low and conventional strength concrete target penetration depths with increasing kinetic energy. Low strength concrete targets show a steeper increase than conventional strength targets in penetration depth with increasing initial kinetic energy. The analytical results are able to capture the two distinct trends while generally over predicting penetration depths possibly because the two

tests used to determine failure strains, SNL-7 and SNL-16, used the more slender 6.0 CRH projectile nose shape which typically penetrate deeper than the 3.0 CRH projectile.

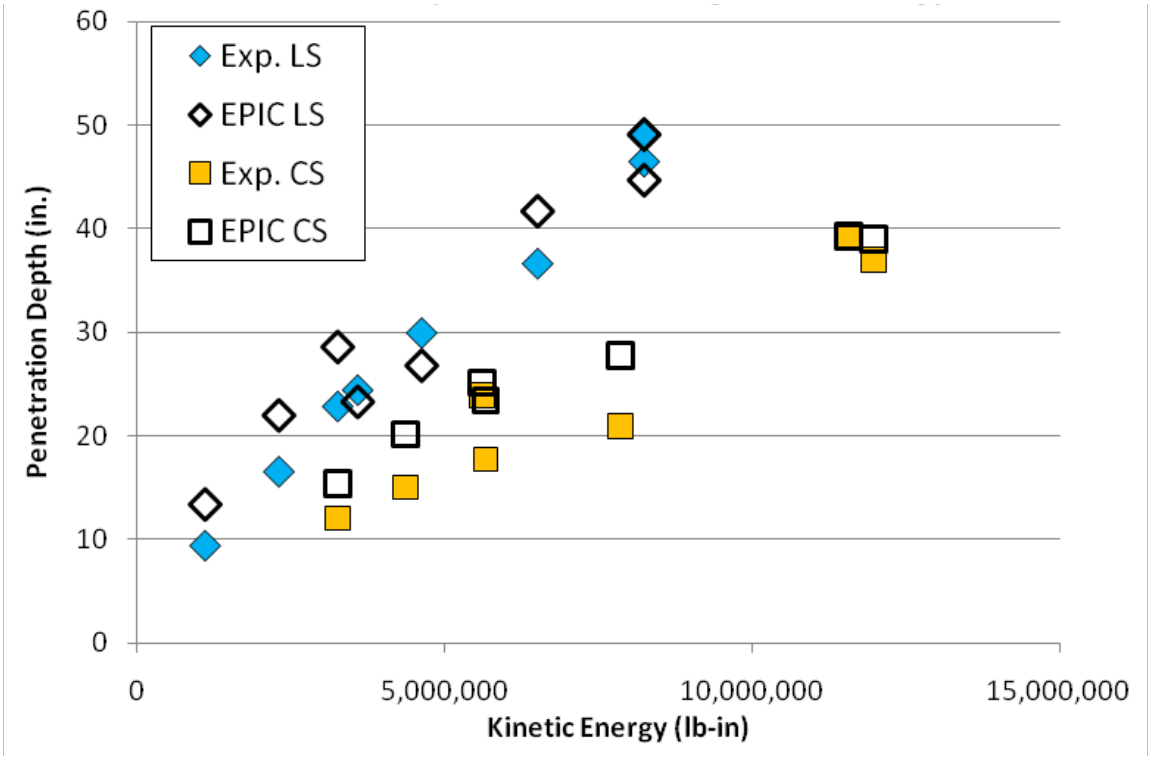

Figure 47. Penetration Depth with Increasing Initial Kinetic Energy for Low (LS) and Conventional Strength (CS) Concrete Targets

6.2. Projectile Mass Loss

Figure 48 and Figure 49 compare the projectile mass loss for analytical and experimental results. Cases for analytical solutions containing no projectile mass loss are not shown, such as in SNL-3 and SNL-6.

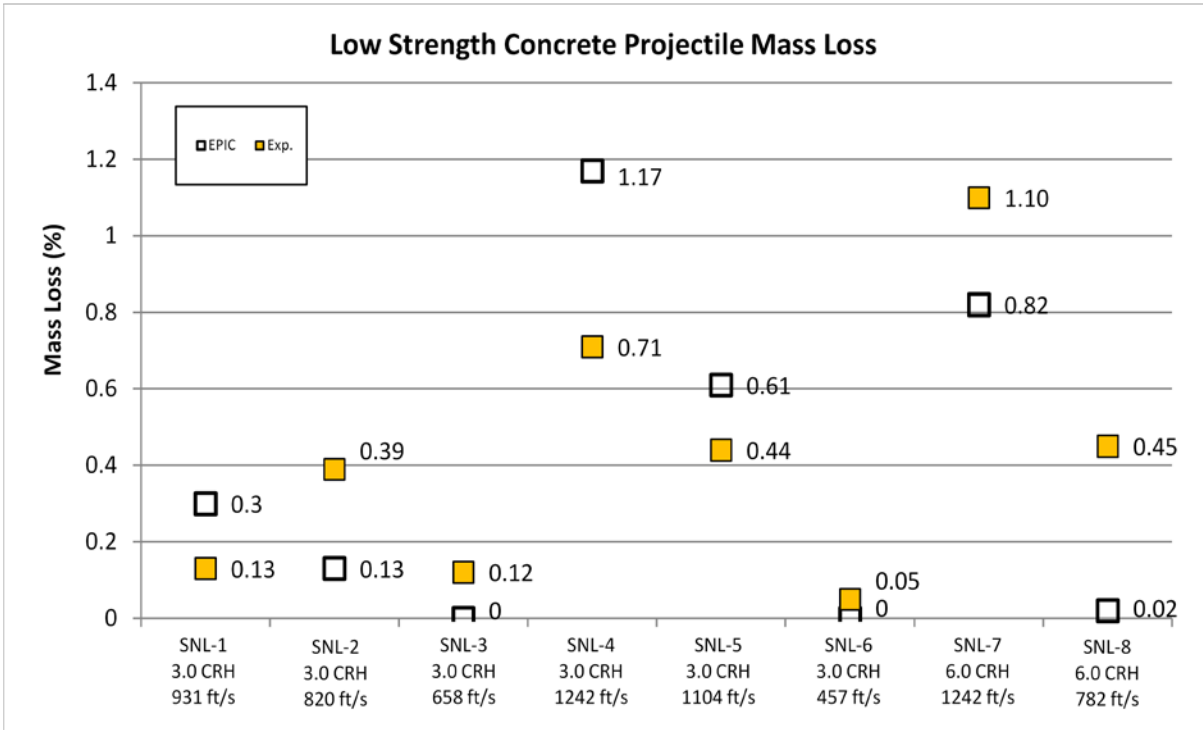

Figure 48. Projectile Mass Loss for Low Strength Concrete Targets

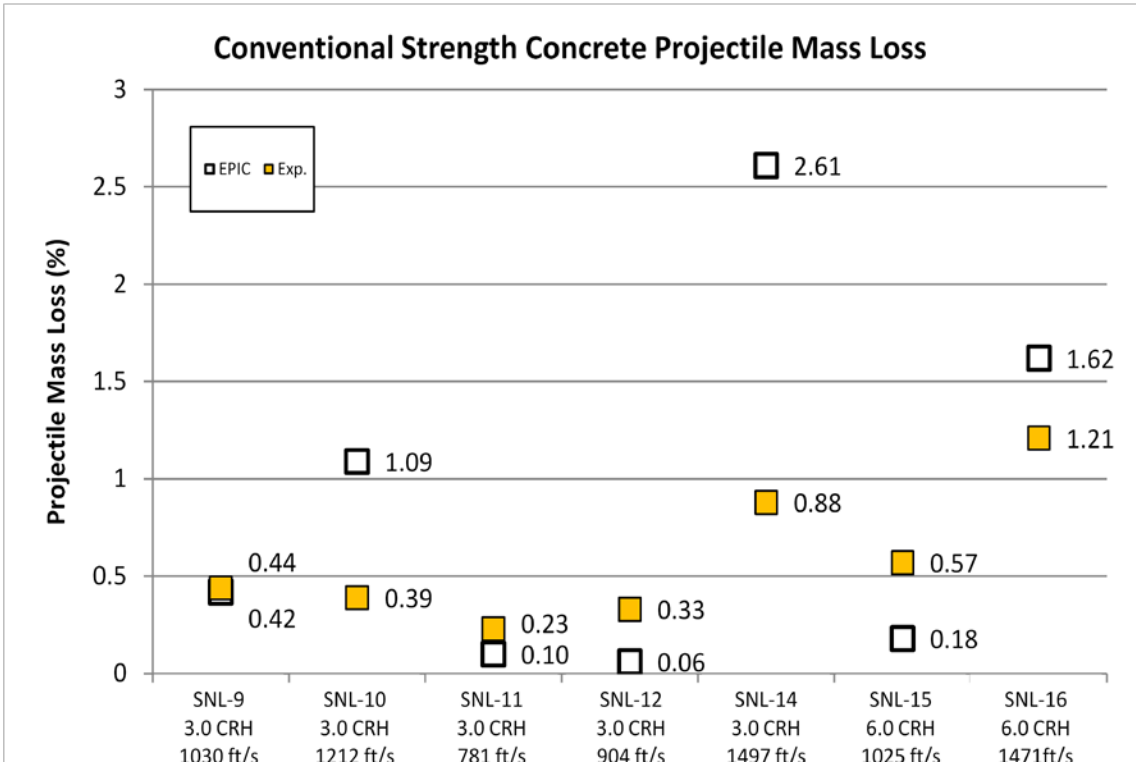

Figure 49. Projectile Mass Loss for Conventional Strength Targets

In general, the E-1 analysis pairing effectively predicted levels of projectile mass loss. The analysis results predicted values that were on average 0.24% and 0.52% away from experimental projectile mass loss (in terms of total mass) for low and conventional strength tests, respectively. The largest errors were shown in test cases SNL-4 and SNL-14 which represented the largest impact velocities for the 3.0 CRH projectiles for the low and conventional strength targets, respectively. This indicates a possible weakness in the JC

material model to calculate mass loss for penetrating projectiles with less slender nose shapes especially as impact velocity increases.

Results for projectile mass loss are compared against initial kinetic energy in Figure 50. No obvious difference in trend is shown for experimental projectile mass loss in low and conventional strength concrete targets. The analytical results for both concrete target strengths under estimate projectile mass loss at lower kinetic energies and over predict the projectile mass loss at higher kinetic energies. This comparison further suggests that the E-1 JC and HJC model pairings over predict at an increasing rate as impact velocity increases, especially shown in the conventional strength concrete test cases. The erroneous analytical trend seen for projectile mass loss indicates that erosion strains for the projectile and target material models are specific to impact velocity ranges. The erosion strain values for the E-1 implemented HJC models were determined for velocities of 1242 and 1471 ft/sec for low and conventional strength concretes respectively; the JC model for the projectile was implemented with erosion strain determined at 1471 ft/sec. As initial kinetic energies fall outside of the range that is used to determine the material model erosion strains, analysis produces increasingly erroneous results for projectile mass loss.

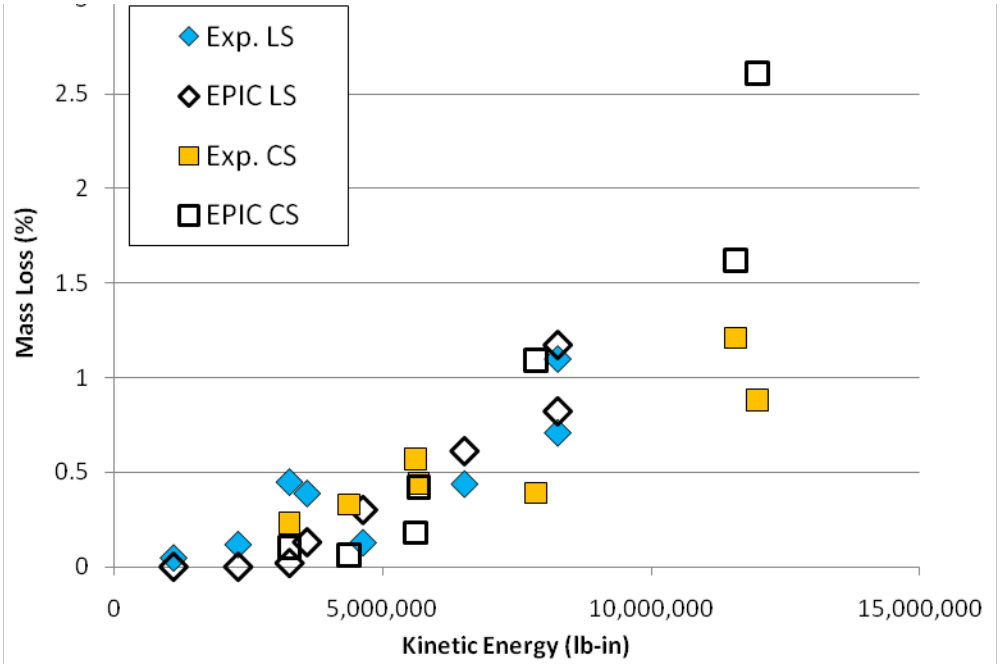

Figure 50. Projectile Mass Loss with Increasing Initial Kinetic Energy for Low (LS) and Conventional Strength (CS) Targets

6.3. Deceleration

Deceleration curve comparisons for the all 15 experimental and analytical tests cases are provided in Appendix 1. Figure 51 shows the comparison for test SNL-5. The experimental deceleration curve is shown as a solid line and the E-1 analysis deceleration is dashed. This convention is used throughout this section, and consistent with the previous method comparison, deceleration results are compared by peak, descending slope, and deceleration

end time. Experimental decelerations results were not available for SNL-1 and SNL-8 and the analytical decelerations will be omitted for the comparisons.

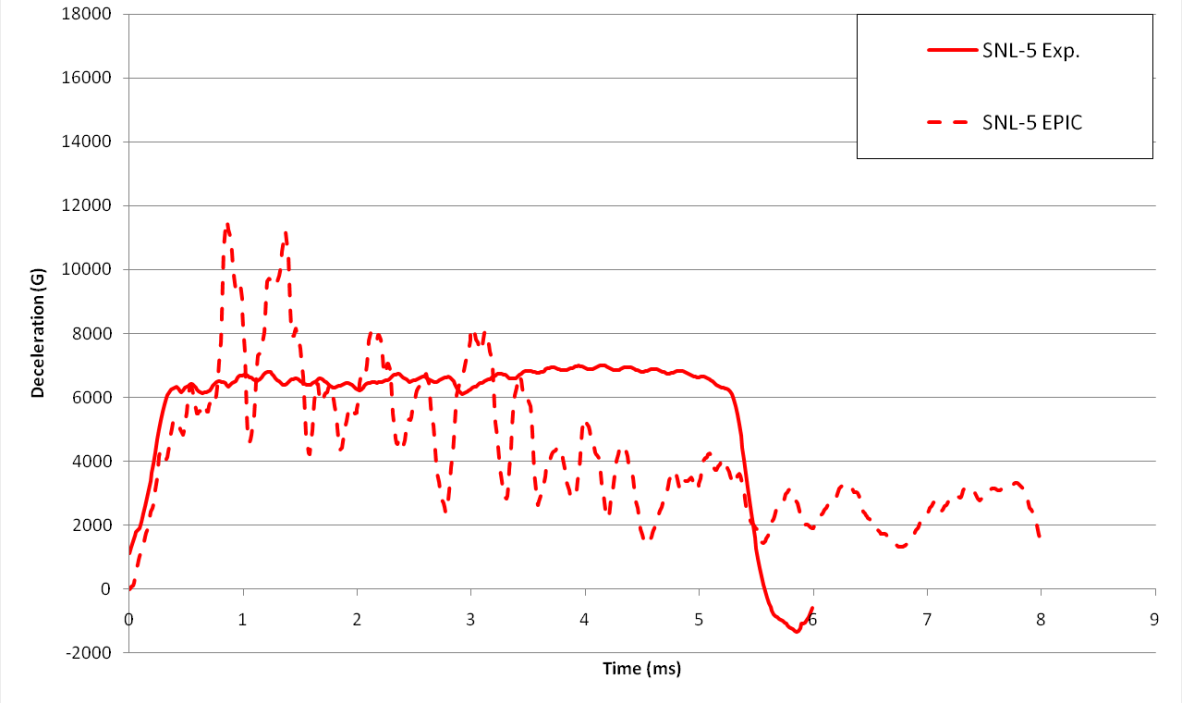

Figure 51. Experimental and E-1 Comparison for Test SNL-5

Experimental peak decelerations for low strength concrete targets, shown as solid lines in Figure 52, all approach a similar maximum value of around 6,500 G. While increases in impact velocity result in slightly higher peak decelerations for low strength concretes, it also causes peak deceleration to be reached earlier. Although not as obvious, these two trends are also observed in the analytical peak decelerations. The low strength analytical peak

decelerations generally over predict the experimental values, especially as impact velocity increases.

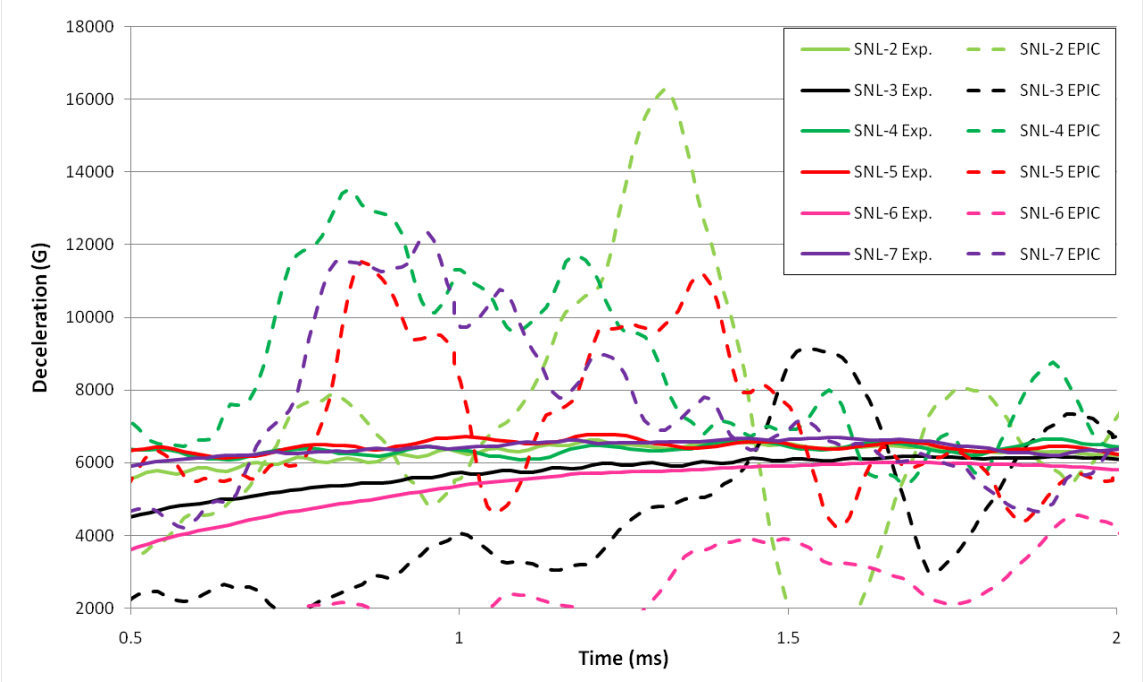

Figure 52. Peak Decelerations for Low Strength Concrete Targets

Similar to that observed for low strength concrete targets, experimental peak decelerations for conventional concrete targets, shown as solid lines in Figure 53 and Figure 54, all approach a similar maximum value between 11,000 and 15,000 G. While increases in impact velocity result in slightly higher peak decelerations for conventional strength concretes, it also causes peak deceleration to be reached earlier. These two trends are also seen in the analytical peak decelerations for conventional strength concrete targets.

Generally, the analytical peak decelerations are slightly higher than the experimental values, and over prediction increases for test cases with higher impact velocities.

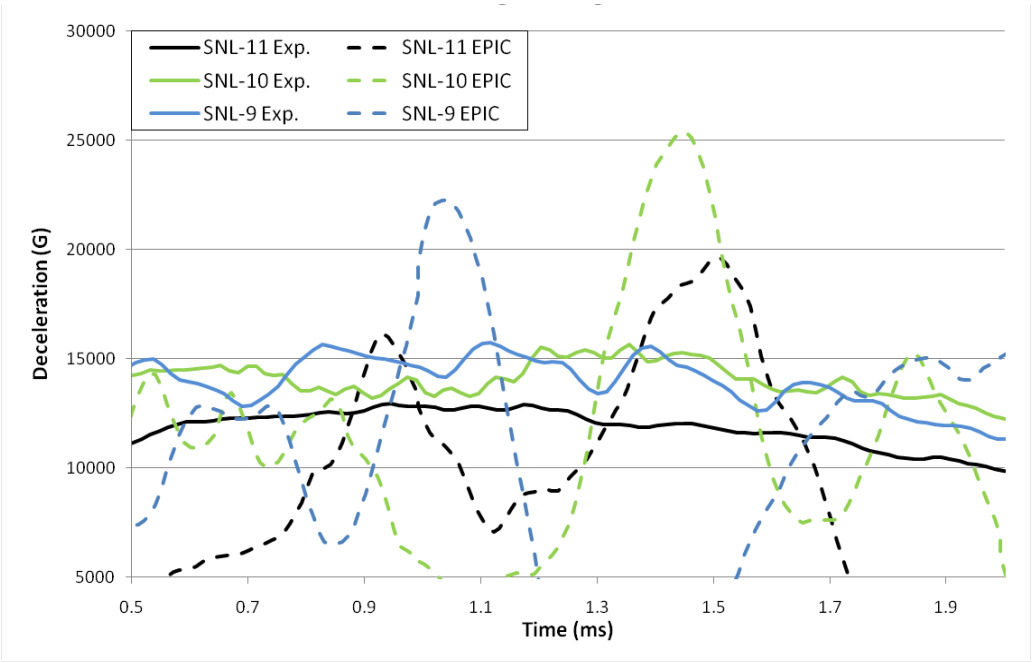

Figure 53. Peak Decelerations for Four ft. Thick Conventional Strength Targets

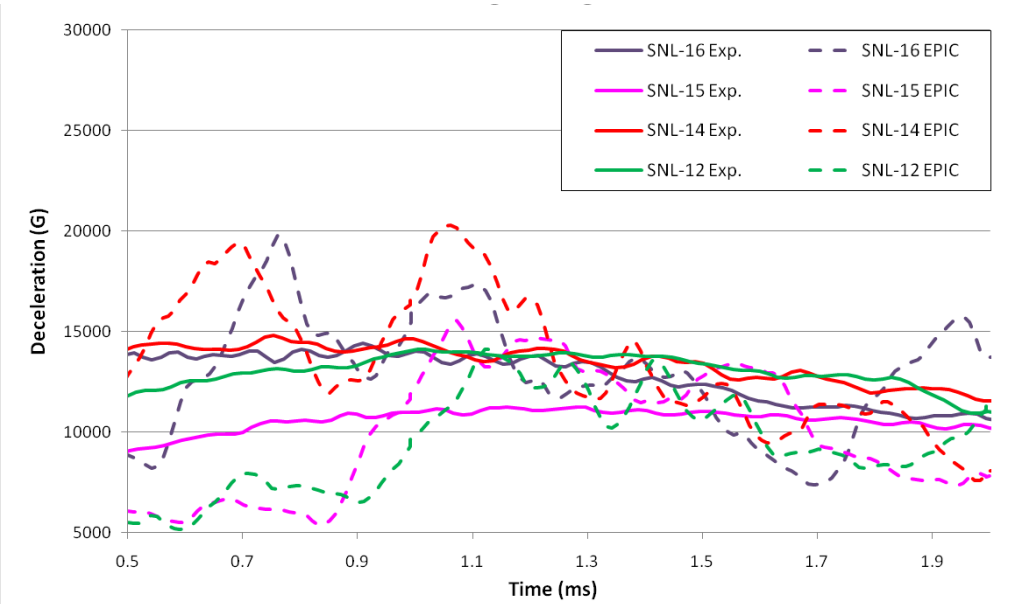

Figure 54. Peak Decelerations for Six ft. Thick Conventional Strength Targets

The influence of projectile nose shape on peak decelerations is observed in the experimental decelerations of conventional strength concrete targets; this was not observed in the low strength concrete tests. This may be most evident with the test cases, SNL-12 (shown as green in Figure 54) and SNL-15 (shown as pink in Figure 54), with experimental impact velocities 904 and 1025 ft/sec, respectively. Although SNL-12 has a smaller impact velocity experimental results show higher peak deceleration than that of SNL-15. The general trend of slightly increasing peak deceleration with increasing impact velocity is not followed by this pair of tests most likely due to the difference in projectile nose shapes; SNL-12 is a 3.0 CRH projectile test and SNL-15 is a 6.0 CRH projectile test.

Figure 55 and Figure 56 compare the affect of nose shape on peak deceleration for low and conventional strength targets, respectively. The figures show a slight increase in experimental peak deceleration with increasing impact velocity for low strength concrete tests. The conventional strength concrete tests show that experimental peak decelerations reach a maximum at impact velocities around 1,500 ft/sec and begin decreasing with increased impact velocity. As for the effect of projectile nose shape, the low strength concrete tests SNL-4 and SNL-7, both with impact velocities of 1242 ft/sec, result in similar experimental peak decelerations. For conventional strength concrete tests, one of the 6.0 CRH projectile tests, SNL-16 (with impact velocity of 1471 ft/sec) followed the 3.0 CRH trend, but the other 6.0 CRH test, SNL-15 (with impact velocity of 1025) resulted in a peak deceleration much lower than the 3.0 CRH tests with similar velocities. It cannot be confidently concluded that slenderness of projectile is more influential in conventional strength concrete tests from the small data set for 6.0 CRH projectiles, but indication of such an influence is observed.

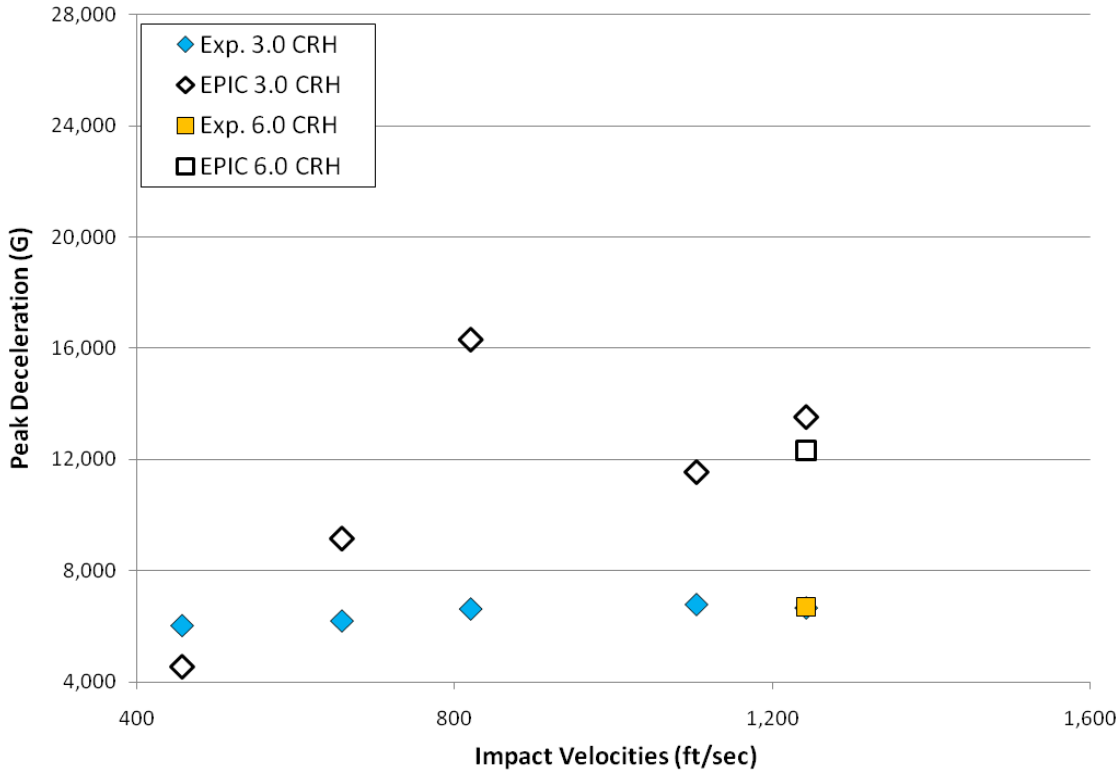

Figure 55. Peak Decelerations for Low Strength Concrete Tests with Increasing Impact Velocity

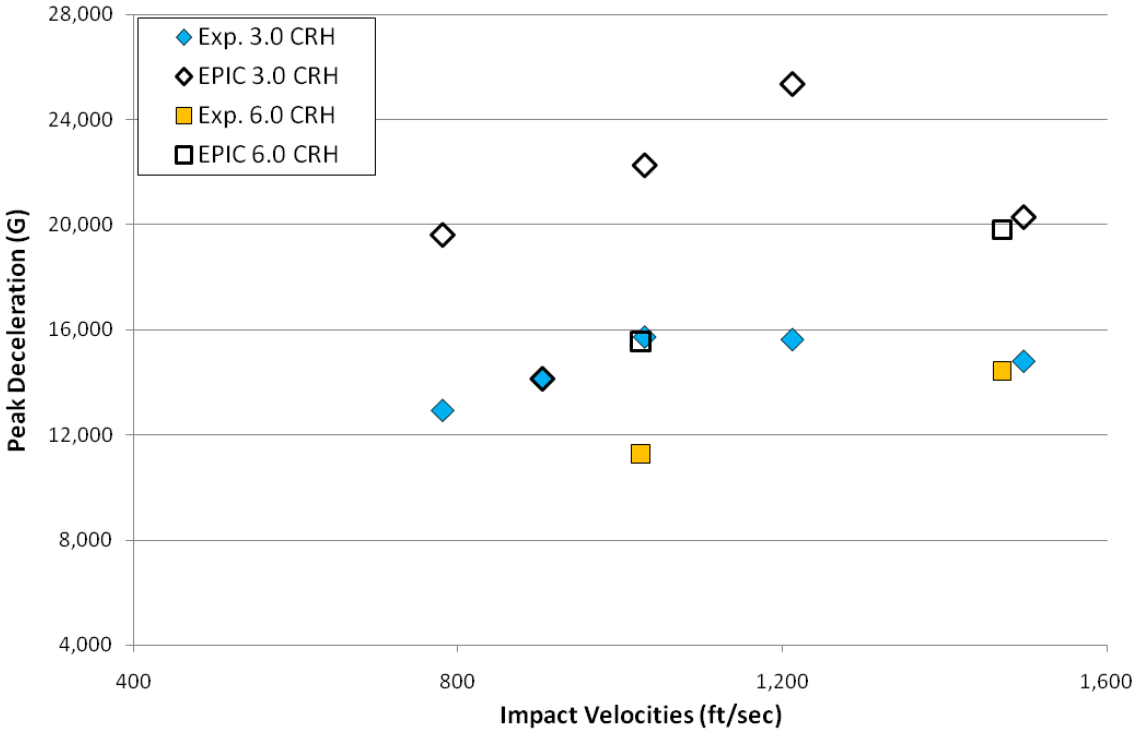

Figure 56. Peak Deceleration for Conventional Strength Concrete Tests with Increasing Impact Velocity

The trends in analytical results for peak deceleration are not as consistent as the experimental results, but they do capture some of the observed tendencies such as those involving impact velocity and nose shape. With the exception of SNL-6 and SNL-12 test cases, the E-1 analysis pairing over predicted values for peak deceleration. Influence of higher frequency output was observed to influence these over predicted analytical values for nearly all of the tests cases.

As was observed in the method comparison, the low strength concrete tests typically showed flat slopes after reaching approximate peak deceleration. The experimental deceleration descending slopes of the low strength concrete targets are compared to analytical results in Figure 57 and Figure 58. Experimental descending slopes change from significantly negative to nearly zero slopes as impact velocities are increased from 457 to 1242 ft/sec. The analytical descending slopes are more accurate for tests with low impact velocities and are unable to capture the decrease in slope observed experimentally as impact velocities are increased.

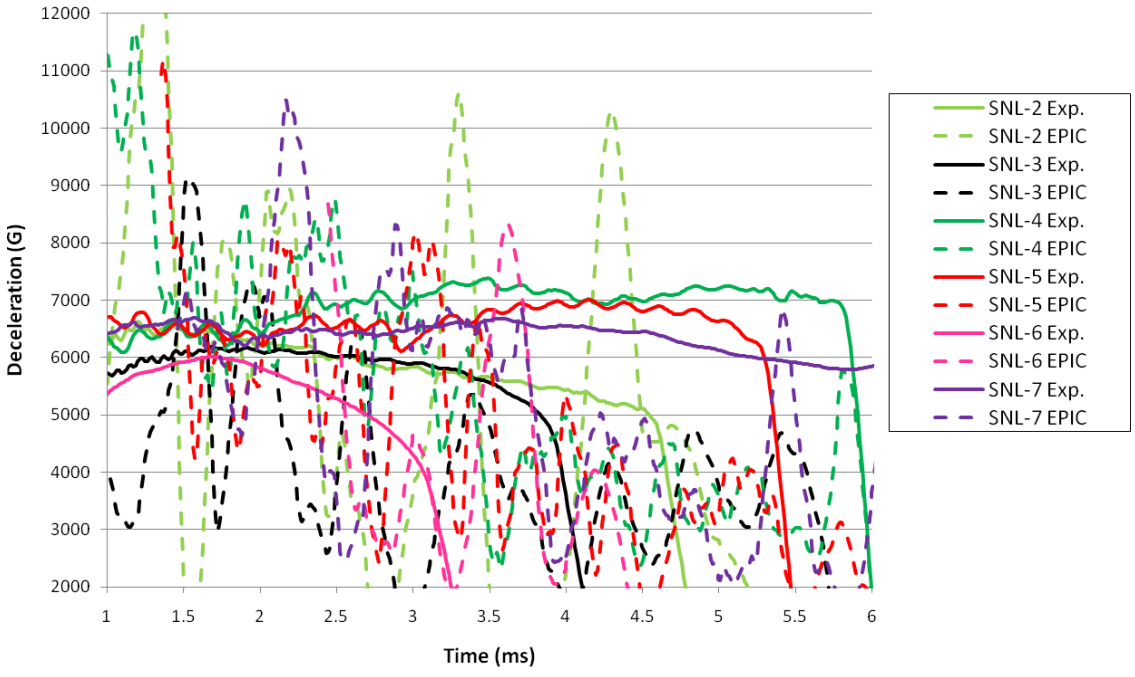

Figure 57. Low Strength Concrete Descending Slopes

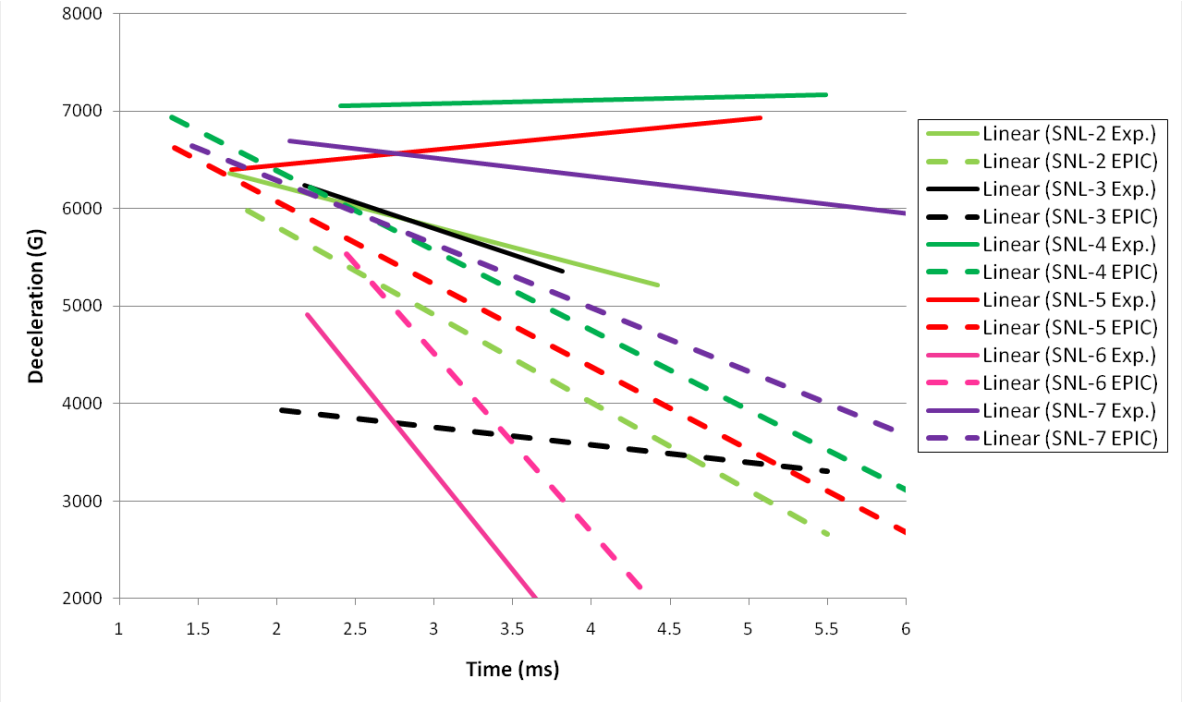

Figure 58. Low Strength Concrete Linear Fit Descending Slopes

Figure 59 and Figure 60 compare the deceleration descending slopes for the four ft. thick conventional strength concrete tests. The test cases resulted in a consistent experimental deceleration slope between -6000 and -7000 G/ms, which were not shown in the analytical slopes. Although consistent measures were used to compare the deceleration curves involving the one ms moving average, the influence of significant high frequency output was observed in the analytical descending slopes and was shown in the linear fit trend lines. While the E-1 results showed a reasonably accurate descending curve for test case SNL-9 (shown in blue in Figure 59), the other two tests showed slopes much different than

experimentally observed. The high frequency interfering output of the E-1 descending slopes is possibly linked to the experimental test case parameters. SNL-11 (shown in black in Figure 59) was the lowest impact velocity test case for the conventional strength concrete tests and resulted in the shortest duration of deceleration. This shorter duration may have been more difficult for the analysis to capture. Also, the linear fit measure used to compare descending slopes may pick up higher frequency interference for shorter duration problems in the output forcing the analytical descending slopes to appear less accurate.

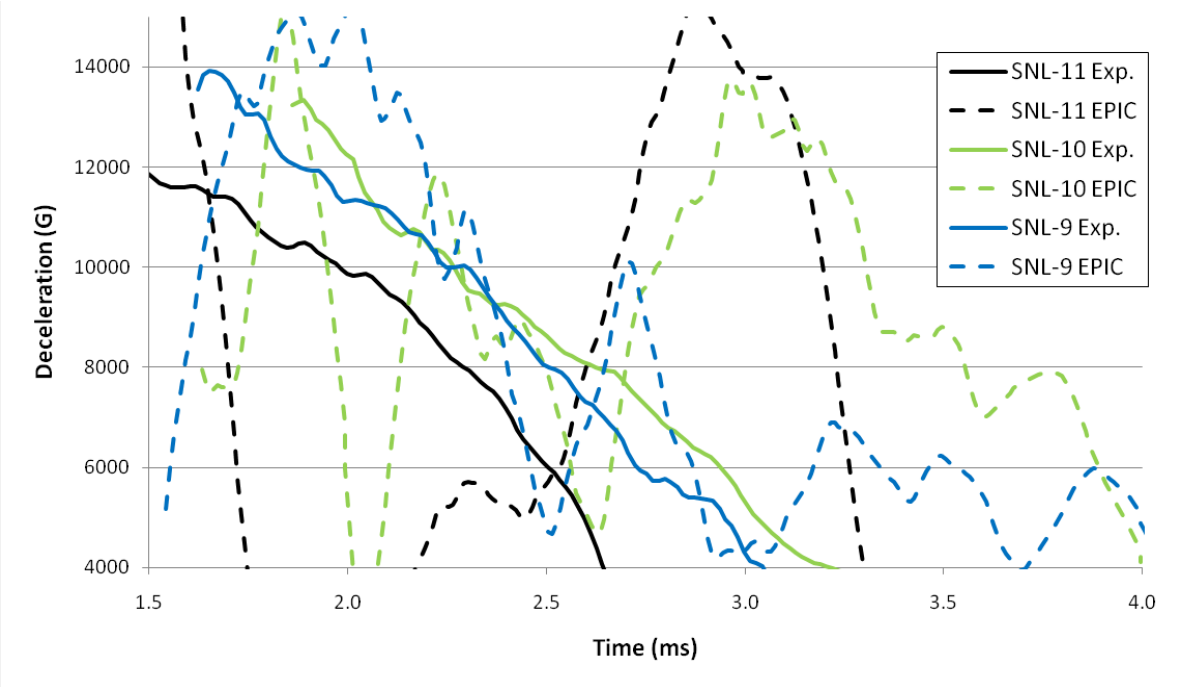

Figure 59. Four ft. Thick Conventional Strength Target Descending Slopes

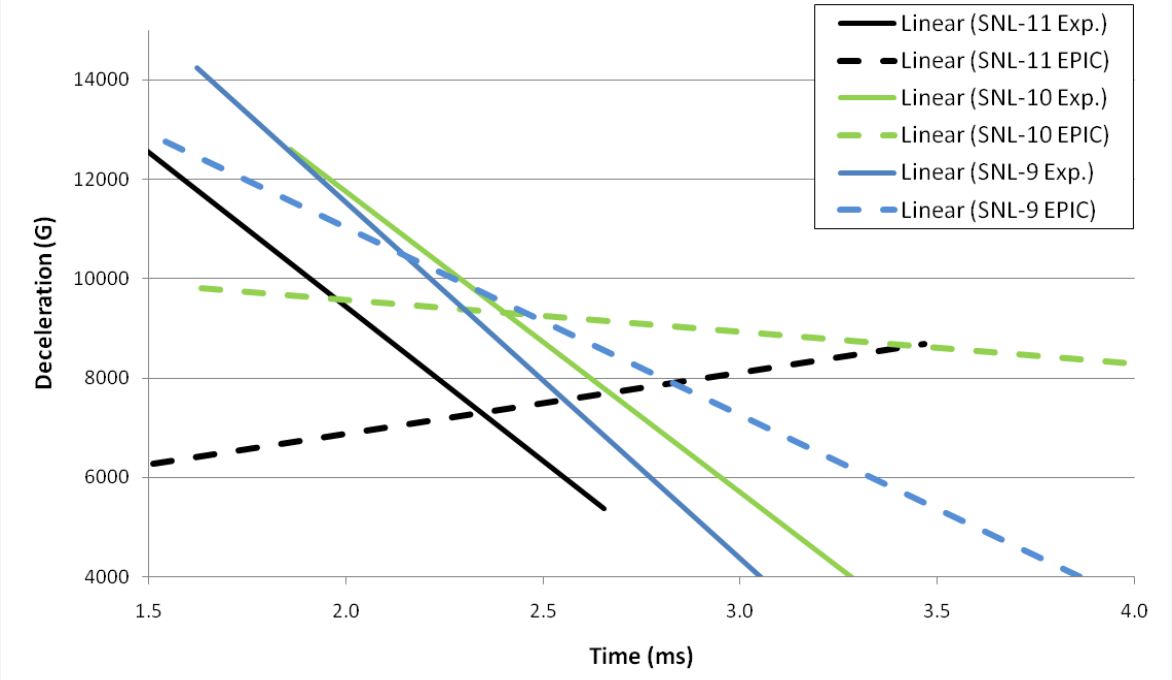

Figure 60. Deceleration Descending Slopes for Four ft. Thick Conventional Strength Concrete Targets

Generally the experimental descending slopes for the six ft. thick conventional target tests shown in Figure 61 and Figure 62 were well capture by the E-1 analysis results. Experimentally, the SNL-12 (shown in blue in Figure 61) test case exhibited an exceptionally low descending slope among the four tests. The impact velocity for SNL-12 was the smallest of the four at 904 ft/sec, but the next highest velocity of 1025 ft/sec for SNL-15 (shown in pink in Figure 61) was not significantly higher. It is possible that SNL-15 exhibited longer, flatter descending slope due to the combination of high impact velocity and slender projectile

nose shape; SNL-12 used a 3.0 CRH projectile and SNL-15 used a 6.0 CRH. This would be consistent with the results from the four ft. target tests, where descending slopes were much steeper with 3.0 CRH projectiles and impact velocities ranging from 781 to 1212 ft/sec. For the six ft. target tests the analytical descending slopes were able to be modeled reasonably well, except for the SNL-12 test case which was predicted be much flatter than the experimental results show. Similar to the four ft. thick target analyses, the SNL-12 shorter duration deceleration may have been more difficult for the E-1 analysis to model or the descending slope measurement more susceptible to erroneous high frequency influence.

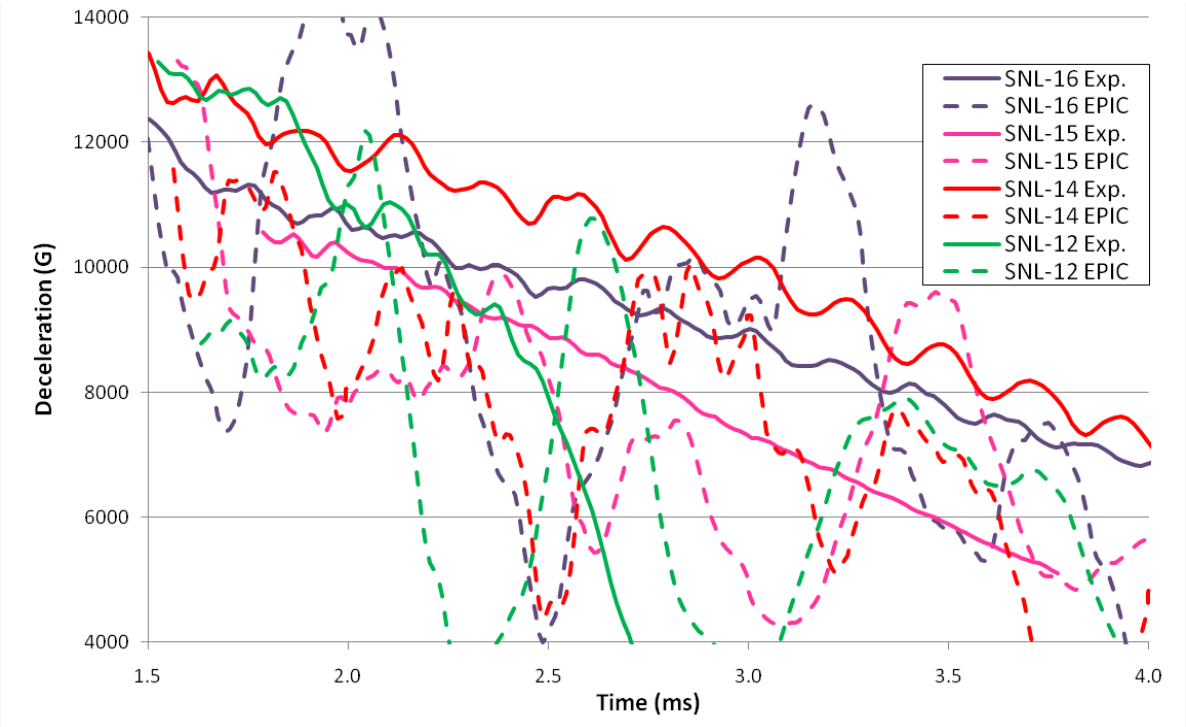

Figure 61. Deceleration Descending Slopes for Six ft. Thick Conventional Strength Concrete Targets

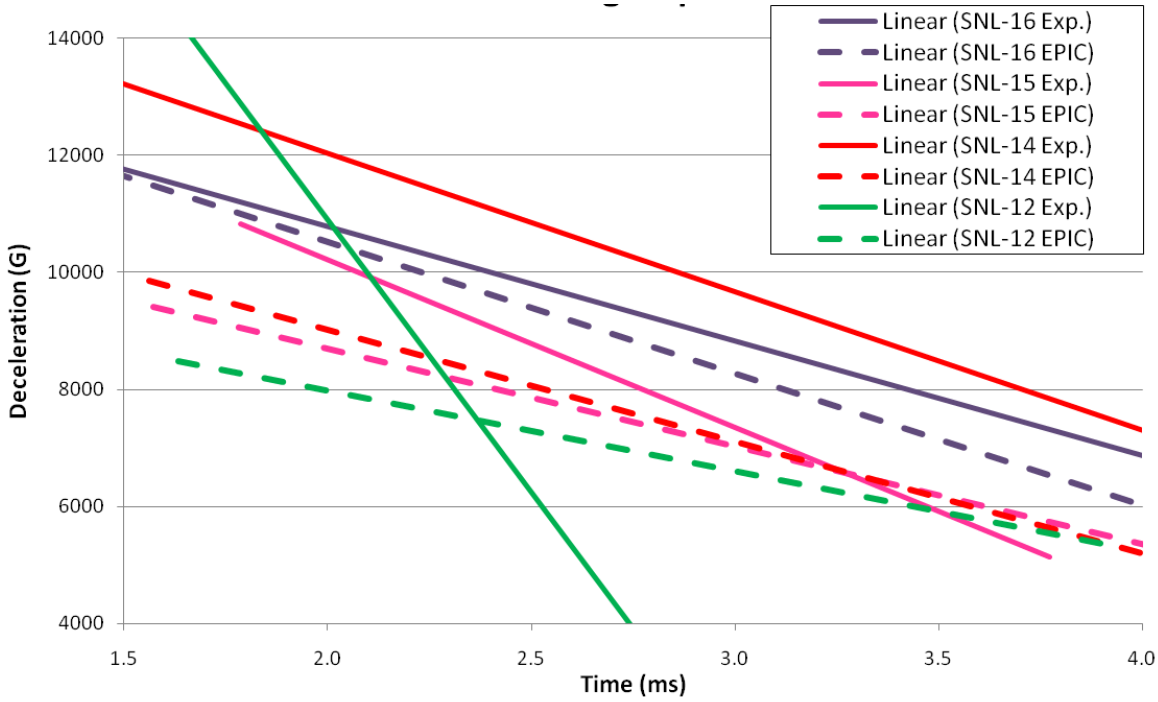

Figure 62. Linear Fit Deceleration Descending Slopes for Six ft. Thick Conventional Strength Concrete Targets

Experimental and analytical deceleration end times for low strength concrete targets are compared in Figure 63. Experimental end times are shown to increase with increasing velocity. While the analytical deceleration end times generally follow the experimental velocity trend, the results consistently over predict the end time by at least one millisecond. Several analytical runs did not even reach deceleration end within the simulation time limits, which were set beyond experimental end times by at least 0.5 ms. The influence of projectile nose shape can also be seen on deceleration end time; tests SNL-4 (shown in dark green in Figure 63) and SNL-7 (shown in purple in Figure 63) have the same impact velocity, but

with the 6.0 CRH projectile used in SNL-7, experimental deceleration end time was greater by roughly 0.5 ms. Additionally, experimental deceleration results include a significant negative deceleration feature observed following the end of positive deceleration. This response increases and becomes more evident as test impact velocity increases, and can be seen best in tests SNL-4, SNL-5 (shown in red in Figure 63), and SNL-7. This response is possibly linked to the frictional resistance applied to the projectile sides after maximum penetration is reached. The ability of E-1 analyses to capture this response is not observed, and would require extended simulation run times for the higher velocity tests.

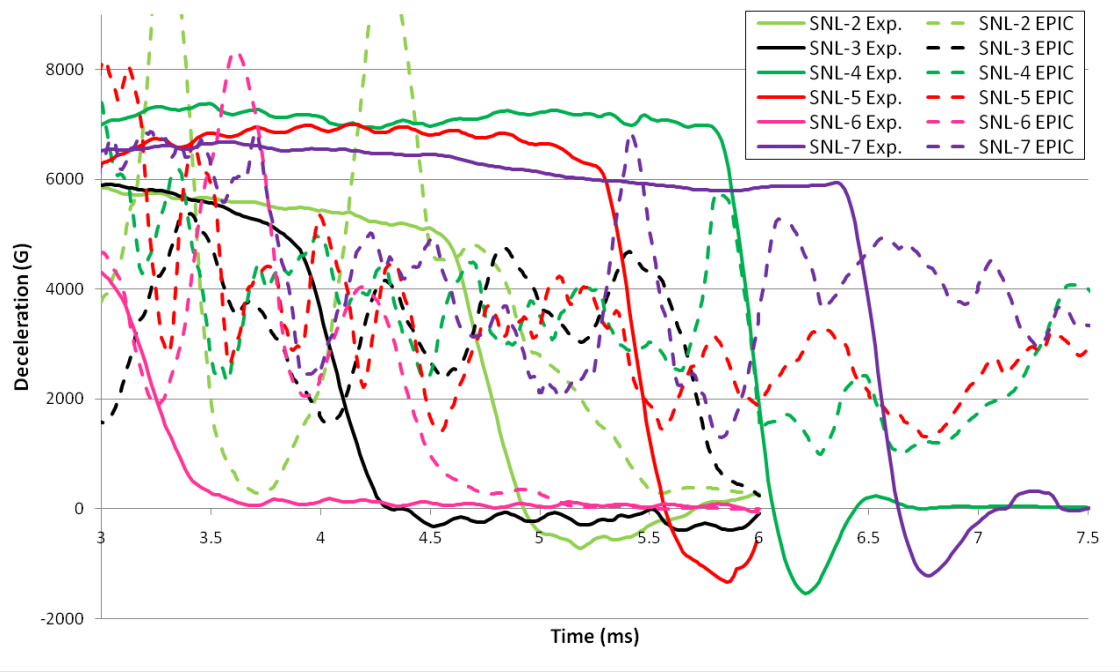

Figure 63. Deceleration End Times for Low Strength Concrete Targets

Figure 64 shows the comparison of experimental and analytical deceleration end times for tests with four ft. thick conventional strength concrete targets. Similar to the low strength concrete results, experimental end times are shown to increase with increasing velocity. The end times for the analytical results were higher than the experimental with the exception of SNL-10 (shown in green in Figure 64) in which the experimental end time was exceptionally accurate.

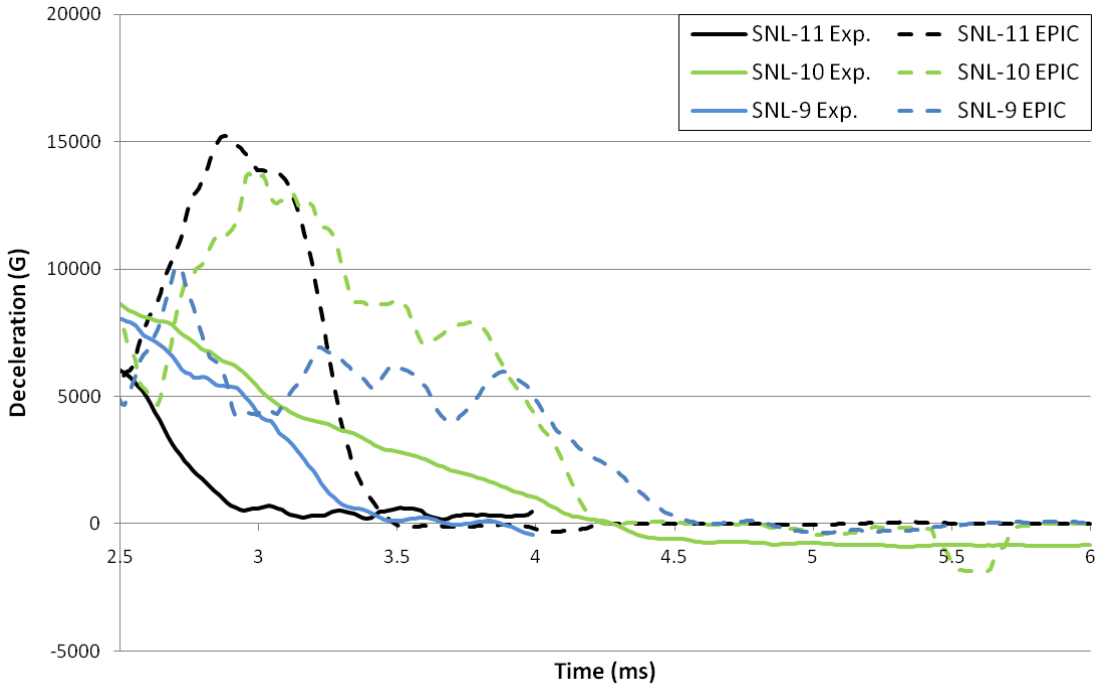

Figure 64. Deceleration End Times for Four ft. Thick Conventional Strength Concrete Targets

Figure 65 shows the comparison of experimental and analytical deceleration end times for six ft. thick conventional strength concrete targets. The influence of projectile nose shape on deceleration end time was observed in comparisons of SNL-12 and SNL-15, as well as SNL-14 and SNL-16 which demonstrate that tests with 6.0 CRH projectiles incur longer experimental decelerations. The analytical deceleration end times generally follow the experiment velocity trend, but exhibit deceleration end times higher than experimental values and fail to capture the influence of projectile nose shape. One exception to the analysis deceleration tendencies is observed in SNL-14 which extends beyond even the end of SNL-16, contrary to experimental observation. This exception is most likely also linked to the general trend of the E-1 end time calculations which predict longer, less accurate values for 3.0 CRH projectile nose shapes. A possible cause of this error trend is that the cases used to find the concrete erosion strain were both cases using 6.0 CRH projectiles.

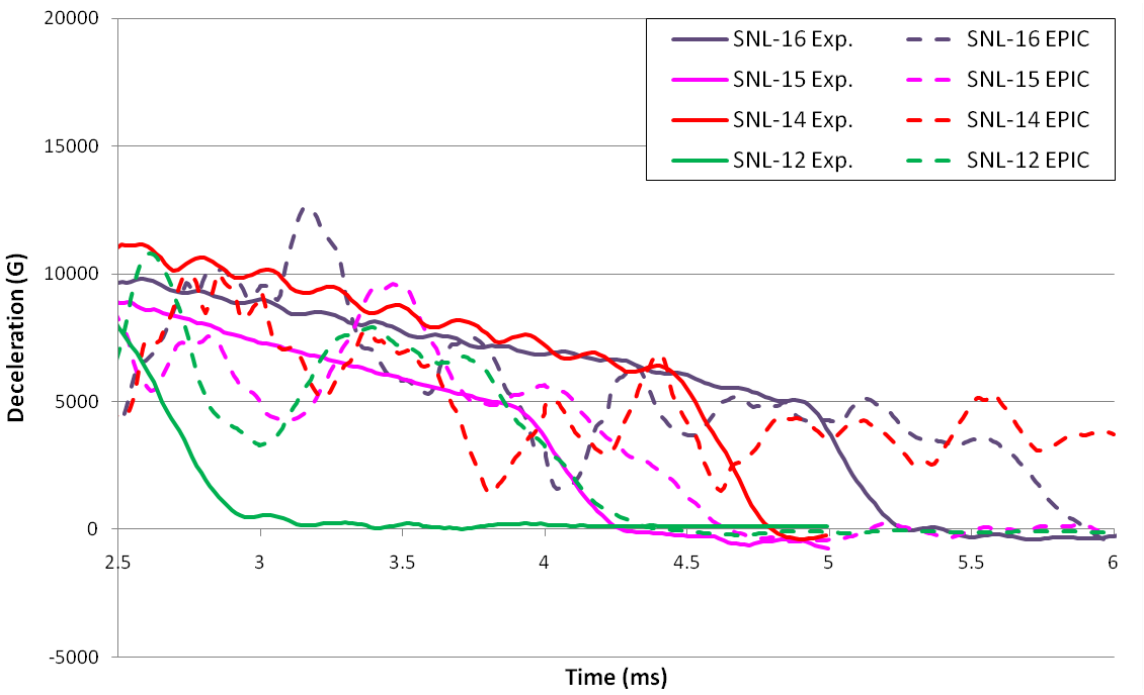

Figure 65. Deceleration End Times for Six ft. Thick Conventional Strength Concrete Targets

Generally, the analytical deceleration curves were more accurate for the conventional strength concrete targets, even after an erosion strain specific to lower strength concrete was determined independently. The defining deceleration features for the experimental tests differed significantly for the two concrete strengths; the distinct initial peak and descending slope present for tests with conventional strength concrete were not observed in the low strength concrete tests. While the analysis generally failed to capture the distinct response for the low strength concrete, results did follow experimental trends in other areas including

impact velocity. The analysis did contain more error in deceleration curves for the 3.0 CRH projectile tests which may stem from the method used to determine the concrete erosion strains. For both concretes, the analysis predicted peak deceleration more accurately than descending slope or deceleration end time. The negative deceleration feature observed in the low strength concrete tests is not observed in the results for the conventional strength tests.

6.4. Damage Plots

Comparisons of experimental and analytical damage included in the experimental parameter study for all 15 test cases are shown in Appendix 2. Figure 66 and Figure 67 demonstrate comparisons of SNL-6 damage for experimental and analytical results from the E-1 analysis. Figure 66 shows the post-test image compared to the E-1 damage contours ranging from zero to one, for undamaged (gray) to damaged (red). The black colored object in the center of the analysis image is the projectile protruding from the target. Figure 67 shows the profile view comparison where the post-test experimental profile is shown in yellow superimposed over the E-1 damage contours. Again, the black colored object is the projectile.



Figure 66. SNL-6 Damage: Experimental (left) and E-1 (right)

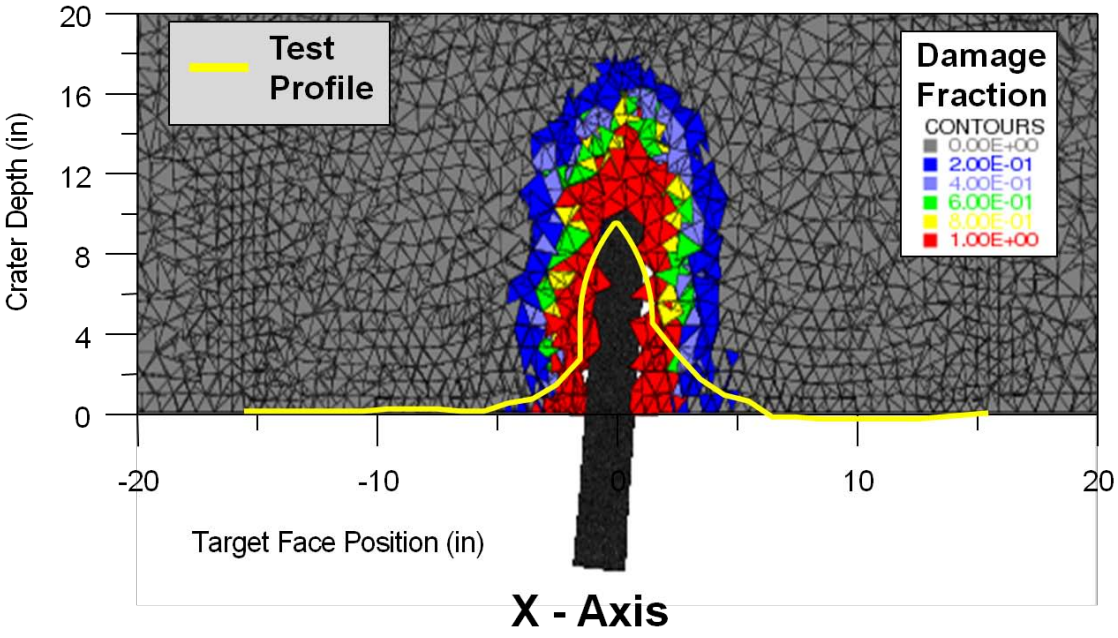

Figure 67. SNL-6 Damage Profiles: Experimental (yellow) Superimposed on E-1 Results (contour)

During the iterative determination of the concrete model erosion strains, it was observed that the spread of damage is significantly reduced as erosion strain levels reach values necessary for appropriate penetration depths. Figure 66 and Figure 67 show the results from a low strength concrete test which was modeled by E-1 with erosion strain of 0.168. Figure 68 and Figure 69 show the results from a low strength concrete test which was modeled by E-1 with erosion strain of 0.24. The analysis code failed to represent any distinct impact crater, and was only able to model the second of the two penetration phases of crater and tunneling which were common to many of the experimental tests such as SNL-16, shown in Figure 69.

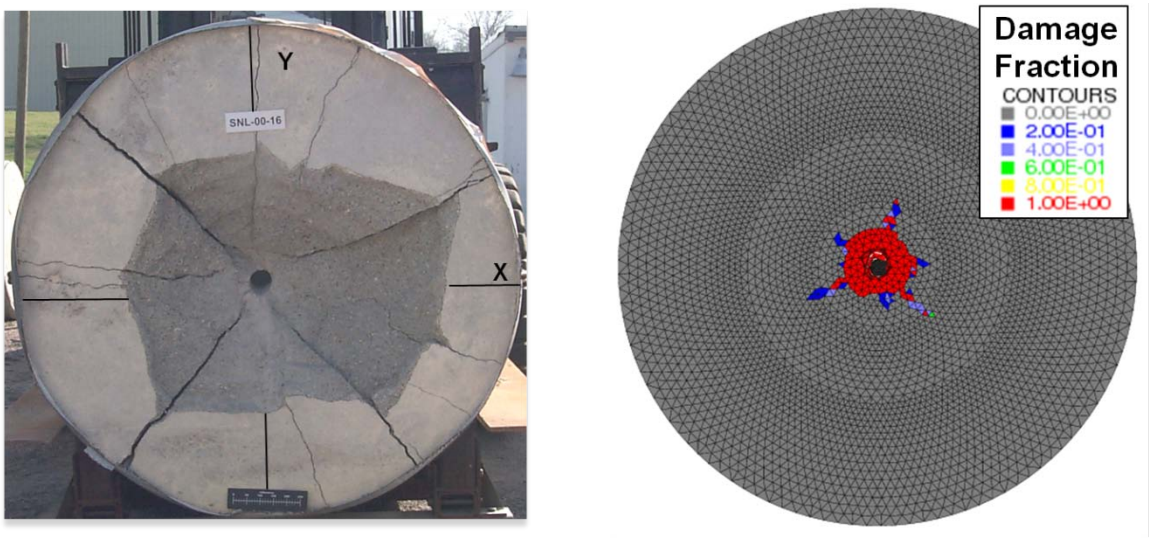

Figure 68. SNL-16 Damage: Experimental (left) and E-1 (right)

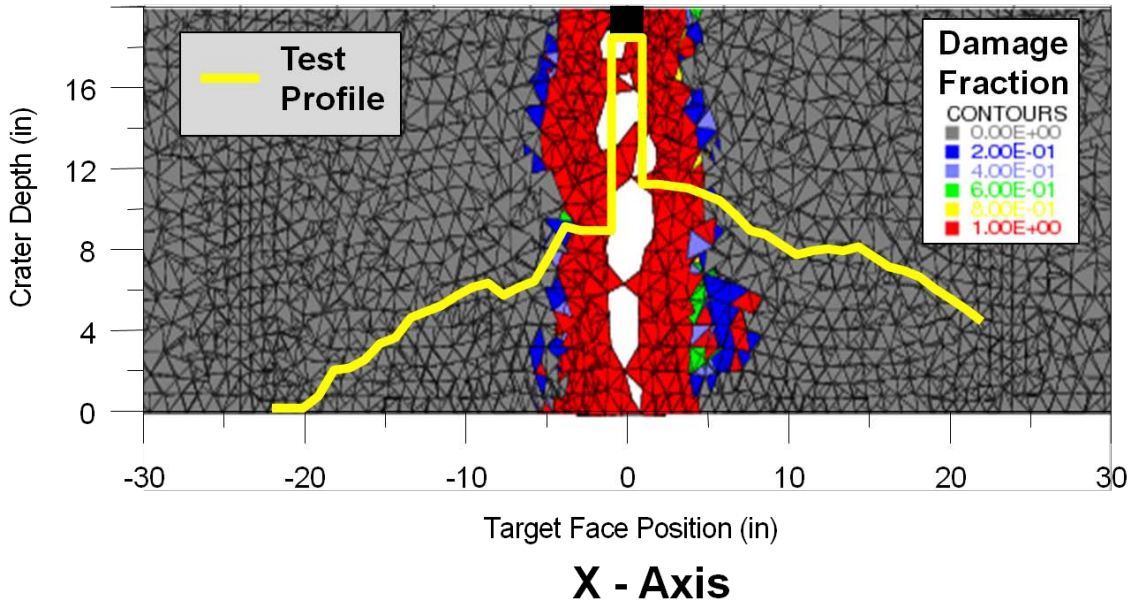

Figure 69. SNL-16 Damage Profiles: Experimental (yellow) Superimposed on E-1 Results (contour)

Experimentally, it was observed that concrete craters are not easily fit to specific trends and may not be a repeatable experimental result due to concrete heterogeneity. Figure 70 shows a comparison of the experimental impact craters for tests SNL-4 and SNL-7. While the tests contained the same concrete strengths and impact velocities with similar penetration depths and decelerations, they differed only in the projectile nose shape. Similarly, the impact craters for SNL-14 and SNL-16 are compared in Figure 71. The tests again differed significantly only in projectile nose shape, with similar impact velocities, penetration depths, and decelerations. The comparisons of impact craters show significant difference and illustrate the somewhat arbitrary nature of crater formation with a heterogeneous material like concrete under penetration.



Figure 70. Comparison of Experimental Damage for Tests SNL-4 and SNL-7



Figure 71. Comparison of Experimental Damage for Tests SNL-14 and SNL-16

6.5. Conclusions

For the experimental parameter study, all 15 test cases from the Sandia Test series were run in EPIC using the HJC concrete model. The goal of the study was to examine the influence of impact velocity, nose shape, target strength and thickness on penetration depth, projectile mass loss, deceleration characteristics, and crater shapes. The input parameters for impact angle, impact velocity, projectile nose shape, target type (low or conventional strength), and target thickness were input specific to each experimental test. Two implementations for the HJC concrete material model were created by specific material test data for the two concrete types in the experimental test series. Independent values for erosion

strain were iteratively determined for each of the two concrete models. A value of 0.168 was determined for low strength concrete and a value of 0.24 was determined for conventional strength. Observations were made for the results of penetration depth, projectile mass loss, deceleration, and damage profiles.

The penetration depth comparisons showed that the E-1 analysis pair more accurately predicted tests with higher impact velocities that resulted in larger penetration depths. The accuracy of different implementations of the HJC model for low and conventional strength showed two separate trends with respect to target thickness. The low strength concrete analyses predicted more accurate penetration depths for four ft. target tests, while the conventional strength tests were better modeled for the six ft. target. The experimental data showed distinct relationships between initial kinetic energy and resulting penetration depth that were specific to the concrete targets strengths. The E-1 analysis was significantly able to reproduce the two relationships.

The analytical results were generally accurate for the projectile mass loss in the experimental tests. Projectile mass loss for low strength concrete tests was more accurately predicted by E-1 than for conventional strength tests. The most erroneous results for projectile mass loss were shown in tests with a 3.0 CRH projectile nose shape. Experimental projectile mass loss trends with respect to initial kinetic energy were less obvious than with penetration depth. Analytically, E-1 consistently produced projectile mass loss too small for lower kinetic energies and too high for higher kinetic energies.

The experimental decelerations showed dramatically different features for low and conventional strength concretes. Low strength concrete tests had no significant initial peak, and the deceleration was generally constant throughout the event where conventional strength concrete tests showed evident initial peaks followed by a descending slope. The E-1 analysis failed to produce deceleration curves of two distinct shapes for the low and conventional strength concrete tests, and generally performed less accurately for the low strength concrete decelerations.

The E-1 analyses were not able to adequately show damage corresponding to impact cratering for the experimental test series. However, it was observed from experimental post-test comparisons that crater profiles may not be a reproducible result and therefore a poor, or less significant measure for model performance.

The EPIC and HJC analysis pairing were most sensitive to variance in impact velocity. The analytical results were most accurate for test cases which fell in a similar velocity range to those tests used to determine the erosion strains. A significant dependency on erosion is indicated; more accurate results would require that appropriate erosion strains be calibrated over multiple impact velocities ranges.

7. Conclusions

An investigation of analysis techniques for the study of concrete impact and penetration problems was completed using four dynamic analysis codes and four concrete constitutive models. The research was conducted in three phases: preliminary evaluation, method comparison, and experimental parameter study. The analysis methods were compared by a consistent grading system on a subset of experimental tests for the preliminary evaluation and method comparison. The experimental parameter study looked at trends between experimental tests and analytical simulations using the full test series. The input parameters for the material models and configuration details for each analysis code were described in Section 4. The LS-DYNA and HJC analysis pairing was found to be the most effective configuration in the preliminary evaluation and method comparison. The EPIC and HJC analysis pairing was used in the experimental parameter study due to the availability of multiple licenses.

7.1. Observations

In the preliminary evaluation, the two Finite Element Method (FEM) codes used in this research, EPIC and LS-DYNA, performed significantly better than other methods. Availability of erosion strain is considered a strong factor in the improved performance, and the absence of this feature in CTH and MPM codes may have prevented more accurate

response. The Material Point Method (MPM) implementation used in this research showed inadequate results for solid dynamics problems, especially concrete impact and penetration. The code was not found convergent for the Taylor impact validation test and erroneous results were observed with symmetrical boundary conditions and material points sticking when using the Drucker-Prager (DP) material model. Of the five concrete material models considered in this research, the Holmquist Johnson Cook (HJC) was the most proficient and provided a thorough model that can be clearly implemented for a specific concrete. The LS-DYNA analysis code was the most successful code evaluated in this research. When implementing the HJC or other concrete models, failure strain should be iteratively determined specifically according to concrete strength for best performance.

The method comparison section measured the performance of EPIC and LS-DYNA against multiple experimental tests. The same failure strain was used for low and conventional strength implementations of each of the HJC, Osborn, and K&C concrete models. The study showed that, while all four analysis pairings showed accurate results for the expanded subset of tests, the LS-DYNA and HJC model pairing performed best. Much more error was observed for low strength concrete tests suggesting that erosion strains for concrete material models are specific to concrete strengths. The erosion strain for the low strength concrete model was revised for the final phase of the study to look for improvement in analytical test results for low strength concrete.

The experimental parameter showed several trends in experimental response. The EPIC-HJC model was able to capture the independent relations between initial kinetic energy and penetration depth for different concrete target strengths. The model provided reasonable results for deceleration for tests with conventional strength concrete targets, but failed to model the near constant deceleration found in tests with low strength targets. The model failed to capture the experimental concrete damage which was typically characteristic of the crater and tunneling regimes; however the experimental damage was observed to be an inconsistent experimental result due to the nature of concrete heterogeneity and may not be an adequate measure for model accuracy.

7.2. Recommendations for Future Work

The MPM and CTH codes should be carefully considered before use in concrete impact and penetration problems. Means to specifically tailor them for such problems in methods similar to the eroding contact available in FEM codes may be highly beneficial. Further work improving and validating the MPM implementation used in this research is warranted.

In practice, it seems common for material models to be used based solely on previously implemented library models. Based on the performance of the concrete models specifically implemented with experimental materials, much caution should be taken in confidently relying upon responses predicted by existing material models. Not only do material models need to be specified to experimental concretes of particular strength, but failure strain values

should be determined specific to experimental concrete strengths. Additionally, the analytical results in this research indicated that appropriate values of erosion strain may be specific to impact velocity. Concrete models currently exist with means to specifically implement concrete materials with limited test data, or knowledge of experimental details. However, in FEM codes material model performance is just as highly dependent on appropriate constant erosion strain values. Development of an integrated, variable erosion strain could be invaluable in concrete impact and penetration modeling. Although appropriate erosion strain values are dependent on more than experimental variables such as stress and pressure; element type, size, and other analysis variables must also be considered when implementing an integrated erosion strain feature that will allow engineers and scientists to use high fidelity analysis methods in scenarios where much of the concrete material information is unknown.

REFERENCES

Akers, S., Ehrgott, J., & Rickman, D. (2005). *Numerical Simulations of Explosive Blast Pressures During Wall Breaching.* Vicksburg, MS: U.S. Army Engineer Research and Development Center.

Akers, S., Weed, R., Rickman, D., & Danielson, K. (2003). *Numerical Simulations of Explosive Wall Breaching Experiments.* Vicksburg, MS: U.S. Army Engineer Research and Development Center.

Anderson, C. E. (1987). An Overview of the Theory of Hydrocodes. *International Journal of Impact Engineering , 5*, 33-59.

Ashby, M. F., & Hallam, S. D. (1986). The Failure of Brittle Solids Containing Small Cracks Under Compressive Stress States. *Acta Metallica , 34* (No. 3), 497-510.

Averett, J. G., & Cargile, J. D. (2005). *Projectile Deceleration Due to Perforation Through Layers of Unreinforced Concrete Targets.* Vicksburg, MS: US Army Engineer Research and Development Center.

Babu, R. R., Benipal, G. S., & Singh, A. K. (2005). Constitutive Modeling of Concrete: An Overview. *Asian Journal of Civil Engineering (Building and Housing) , 6* (No. 4), 211-246.

Beissel, S. R., & Johnson, G. R. (2000). Large-deformation Triangular and Tetrahedral Element Formulations for Unstructured Meshes. *Computational Methods in Applied Mechanics and Engineering , 187*, 469-482.

Belytschko, T., Krongauz, Y., Organ, D., Fleming, M., & Krysl, P. (1996). Meshless Methods: An Overview and Recent Developments. *Computer Methods in Applied Mechanics and Engineering , 139*, 3-47.

Benson, D. J. (1992). Computational Methods in Lagrangian and Eulerian Hydrocodes. *Computer Methods in Applied Mechanics and Engineering* , 235-394.

REFERENCES

Bischoff, P. H., & Perry, S. H. (1986). Compressive Strain Rate Effects of Concrete. In S. Mindess, & S. P. Shah (Ed.), *Proceedings of the Cement-Based Composites: Strain Rate Effects on Fracture Symposium.* Boston, MA.

Bresler, B., & Pister, K. S. (1958). Strength of Concrete Under Combined Stresses. *ACI Journal , 50*, 321-345.

Cargile, D. (1998). *Development of a Constitutive Model for Numerical Simulation of Projectile Penetration into Brittle Geomaterials.* Doctoral Dissertation, Purdue University.

Cargile, J. D., & Tidwell, L. E. (1993). *Penetration of a Subscale Semi-Armor-Piercing Projectile into Conventional-Strength and High-Strength Concrete Targets.* Vicksburg, MS: US Army Corps of Engineers, Waterways Experiment Station.

Cargile, J. D., Giltrud, M. E., & Luk, V. K. (1993). *Perforation of Thin Unreinforced Concrete Slabs.* Vicksburg, MS: US Army Waterways Experiment Station.

Chen, W. F., & Han, D. J. (1988). *Plasticity for Structural Engineers.* New York: Springer-Verlag.

Cook, R. D., Malkus, D. S., Plesha, M. E., & Witt, R. J. (2002). *Concepts and Applications of Finite Element Analysis.* Madison, WS: John Wiley & Sons.

Crawford, D. A., Bell, R. L., Brundage, A. L., Bruner, C. W., Elrick, M. G., Hertel, E. S., et al. (2007). *CTH User's Manual and Input Instructions.* Albuquerque, NM: Sandia National Laboratories.

Dancygier, A. N., Yankelevsky, D. Z., & Jaegermann, C. (2007). Response of High Performance Concrete Plates to Impact of Non-deforming Projectiles. *International Journal of Impact Engineering , 34*, 1768-1779.

Dawson, A., Bless, S., Levinson, S., Pedersen, B., & Satapathy, S. (2008). Hypervelocity Penetration of Concrete. *International Journal of Impact Engineering , 35*, 1484-1489.

Donea, J., Huerta, A., Ponthot, J., & Rodriguez-Ferran, A. (2004). Arbitrary Lagrangian-Eulerian Methods. In E. Stein, R. de Borst, & T. Hughes, *Encyclopedia of Computational Mechanics* (pp. Ch. 14 1-25). John Wiley & Sons.

Ehrgott, J. Q., Cargile, J. D., & Windham, J. E. (2007). *Crater and Damage Effects and Ground Shock Loading from Standoff Detonations on Concrete Slabs with Varied Edge Fixity.* Vicksburg, MS: Geotechnical and Structures Laboratory.

Forrestal, M. J., Frew, D. J., Hickerson, J. P., & Rohwer, T. A. (2002). Penetration of Concrete Targets with Deceleration-Time Measurements. *International Journal of Impact Engineering , 28*, 479-497.

Frew, D. (2002). *Low Strength and Conventional Strength Concrete Instrumented Penetration Results.* Albuquerque, NM: Sandia National Laboratories.

Gold, V. M., Vradis, G. C., & Pearson, J. C. (1996). Concrete Penetration by Eroding Projectiles: Experiments and Analysis. *Journal of Engineering Mechanics , February*, 145-152.

Hallquist, J. O. (2006). *LS-DYNA Theory Manual.* Livermore, CA: Livermore Software Technology Corporation.

Hanchak, S. J., Forrestal, M. J., Young, E. R., & Ehrgott, J. Q. (1992). Perforation of Concrete Slabs with 48 MPa (7 ksi) and 140 MPa (20 ksi) Unconfined Compressive Strengths. *International Journal of Impact Engineering , 12*, 1-7.

Holmquist, T. J., Johnson, G. R., & Cook, W. H. (1993). A Computational Constitutive Model for Concrete Subjected to Large Strains, High Strain Rates, and High Pressures. *Fourteenth International Symposium on Ballistics.* Quebec City, Canada.

Hughes, M. L., Tedesco, J. W., & Ross, C. A. (1993). Numerical Analysis of High Strain Rate Splitting-Tensile Tests. *Computers and Structures , 47* (No. 4), 653-671.

Isenberg, J., Vaughan, D. K., & Sandler, I. S. (1978). *Nonlinear Soil-Structure Interaction.* Weidlinger Associates.

Johnson, G. R., & Holmquist, T. J. (1988). Evaluation of Cylinder-Impact Test Data for Constitutive Model Constants. *Journal of Applied Physics , 64* (No. 8), 3901-3910.

REFERENCES

Johnson, G. R., Beissel, S. R., Gerlach, C. A., Stryk, R. A., Holmquist, T. J., Johnson, A. A., et al. (2006). *User Instructions for the 2006 Version of the EPIC.* Minneapolis, MN: Network Computing Services, Inc.

Jonas, G. H., & Zukas, J. A. (1978). Mechanics of Penetration: Analysis and Experiment. *International Journal of Engineering Science , 16*, 879-903.

Joy, S., & Moxley, R. (1993). *White Sands Missile Range 5 3/4-inch Concrete Properties.* US Army Engineers Waterways Experiment Station Briefing Prepared for Defense Special Weapons Agency.

Li, S., & Liu, W. K. (2002). Meshfree and Particle Methods and Their Applications. *Applied Mechanics Reviews , 55* (No. 1), 1-34.

Lin, H., & Atluri, S. N. (2001). The Meshless Local Petrov-Galerkin (MLPG) Method for Solving Incompressible Navier-Stokes Equations. *CMES , 2* (No. 2), 117-142.

Livermore Software Technology Corporation. (2007). *LS-DYNA Keyword User's Manual, Volumes I and II.* Livermore, CA: Livermore Software Technology Corporation.

Lopez-Cela, J. J. (2002, May). Material Identification Procedure for Elastoplastic Drucker-Prager. *Journal of Engineering Mechanics* , 586-591.

Loret, B., & Prevost, J. H. (1986). Accurate Numerical Solutions for Drucker-Prager elasticplastic. *Computer Methods in Applied mechanics and Engineering , 54*, 259-277.

Ma, S., & Zhang, S. (2007). Material Point Method for Impact and Explosion Problems. *Computational Mechanics* .

Mair, H. U. (1999). Review: Hydrocodes for Structural Response to Underwater Explosions. *Shock and Vibration , 6* (No. 2), 81-96.

Malvar, J. L., & Simons, D. (1996). Concrete Material Modeling in Explicit Computations. *Workshop on Recent Advances in Computational Structural Dynamics and High Performance Computing.* USAE Waterways Experiment Station.

REFERENCES

Malvar, L. J., Crawford, J. E., Wesevich, J. W., & Simons, D. (1997). A Plasticity Concrete Material Model for DYNA3D. *International Journal of Impact Engineering , 19* (No. 9-10), 847-873.

Matuska, D. A., Durret, R. E., & Osborn, J. J. (1982). *Hull User Guide for Three-Dimensional Linking with EPIC-3.* Shalimar, FL: Orlando Technology, Inc.

Murray, Y. D. (2007). *Users Manual for LS-DYNA Concrete Material Model 159.* U.S. Department of Transportation, FHA.

Murray, Y. D., Abu-Odeh, A., & Bligh, R. (2007). *Evaluation of LS-DYNA Concrete Material Model 159.* McLean, VA: U.S. Dept. of Transportation, FHA.

Noble, C., Kokko, E., Darnell, I., Dunn, T., Hagler, L., & Leininger, L. (2005). *Concrete Model Descriptions and Summary of Benchmark Studies for Blast Effects Simulations.* Livermore, CA: Lawrence Livermore National Laboratory.

Ottosen, N. S. (1977). A Failure Criterion for Concrete. *Journal of Engineering Mechanics Division, ASCE , 103* (EM4), 527-535.

Pelessone, D. (1989). *A Modified Formulation of the Cap Model.* Defense Nuclear Agency.

Polanco-Loria, M., Hopperstad, O. S., Borvik, T., & Berstad, T. (2008). Numerical Predictions of Ballisitic Limits for Concrete Slabs Using a Modified Version of the HJC Concrete Model. *International Journal of Impact Engineering , 35*, 290-303.

Ross, C. A., Kuennen, S. T., & Tedesco, J. W. (1992). Effects of Strain Rate on Concrete Strength. *Session on Concrete Research in the Federal Government.* Washington, D.C.: ACI Spring Convention.

Rowher, T. A., Heise, J. F., & Wilder, D. J. (2001). *Waterways Experiment Station Code Validation Tests.* Albuquerque, NM: Sandia National Laboratories.

Schwer, L. E., & Malvar, L. J. (2005). *Simplified Concrete Modeling with Mat*_Concrete_Damage_Rel3.* Windsor, CA: Schwer Engineering & Consulting Services.

Schwer, L. E., & Murray, Y. D. (1994). A Three-Invariant Smooth Cap Model with Mixed Hardening. *International Journal for Numerical and Analytical Methods in Geomechanics , 18*, 657-688.

Schwer, L. E., & Murray, Y. D. (2002). Continuous Surface Cap Model for Geomaterial Modeling: A New LS-DYNA Material Type. *7th International LS-DYNA Users Conference* (pp. 16-35). Dearborn, Michigan: LSTC & ETA.

Senft, L. E., & Stewart, S. T. (2007). Modeling Impact Cratering in Layered Surfaces. *Journal of Geophysical Research , 112*, 1-18.

Silling, S. A. (1997). *Brittle Failure Kinetics Model for Concrete.* Albuquerque, NM: Sandia National Laboratories.

Silling, S. A. (2001). *CTH Reference Manual: BFK Model for Concrete.* Albuquerque, NM: Sandia National Laboratories.

Silling, S. A. (1993). Simulation of Penetration and Perforation with CTH. *Andvances in Numerical Simulation Techniques for Penetration and Perforation of Solids* , 57-66.

Sjol, H., & Teland, J. A. (2001). Boundary Effects in Penetration of Rigid Projectiles into High Performance Concrete Targets. *10th International Symposium on Interaction of the Effects of Munitions with Structures.*

Smith, G. D. (1985). *Numerical Solution of Partial Differential Equations: Finite Difference Methods.* New York, NY: Oxford Univeristy Press.

Tai, Y., & Tang, C. (2006). Numerical Simulation: The Dynamic Behavior of Reinforced Concrete Plates Under Normal Impact. *Theoretical and Applied Fracture Mechanics , 45*, 117-127.

Unosson, M., & Nilsson, L. (2006). Projectile Penetration and Perforation of High Performance Concrete. *International Journal of Impact Engineering , 32*, 1068-1085.

Wang, Z., Li, Y., Shen, R. F., & Wang, J. G. (2007). Numerical Study on Craters and Penetration of Concrete Slab by Ogive-Nose Steel Projectiles. *Computers and Geotechnics , 34*, 1-9.

Wilbeck, J. S. (1985). *Classification of Impact Regimes.* San Antonio, TX: Southwest Research Institute.

William, K. J., & Warnke, E. P. (1974). Constitutive Model for the Triaxial Behavior of Concrete. *IABSE Proc* (pp. Paper II-1). Bergamo, Italy: International Association of Bridge and Structural Engineers, Seminar on Concrete Structure Subjected to Triaxial Stresses.

Yonten, K., Manzari, M. T., Eskandarian, A., & Marzougui, D. (2002). An Evaluation of Concrete in LS-DYNA Finite Element Code. *15th ASCE Engineering Mechanics Conference.* New York, NY: Columbia University.

York, A. R. (1997). *Development of Modifications to the Material Point Method for the Simulation of Thin Membranes, Compressible Fluids, and Their Interactions.* Albuquerque, NM: Sandia National Laboratories.

Zienkiewicz, O. C. (1979). *The Finite Element Method.* London: McGraw-Hill.

Zukas, J. A. (1980). *Impact Dynamics: Theory and Experiment.* Aberdeen Proving Ground, MD: U.S. Army Armament Research and Development Command.

BUSH, BLAKE MARSHALL. Analytical Evaluation of Concrete Penetration Modeling Techniques.
REFERENCES

APPENDICES

Appendix A

1. Experimental Parameter Study Deceleration Plots

This section contains the experimental (where available) and analytical decelerations for the experimental parameter study using the E-1 analysis pairing for the 15 experimental impact tests.

1.1. SNL-1

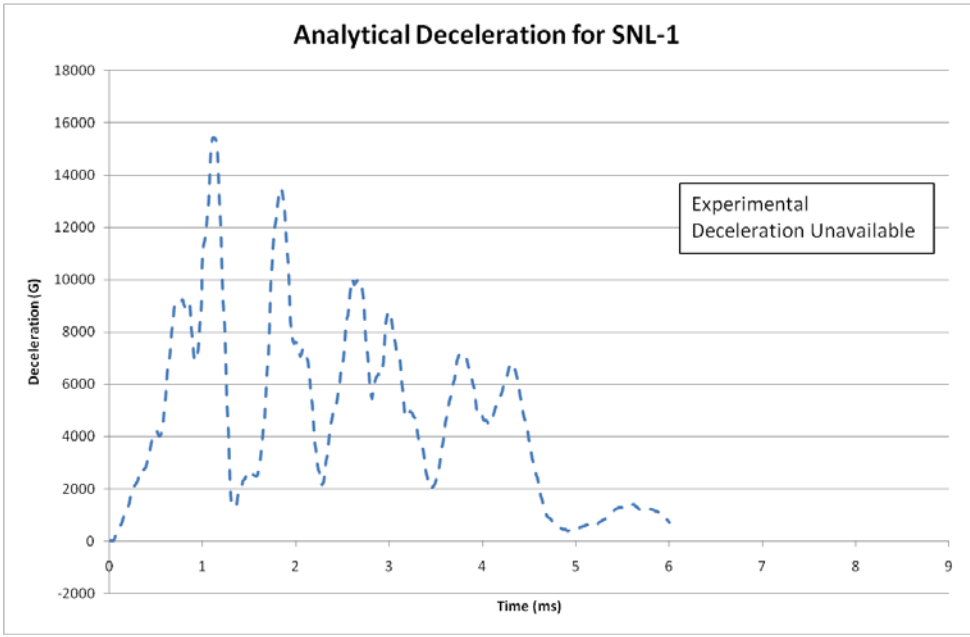

1.2. SNL-2

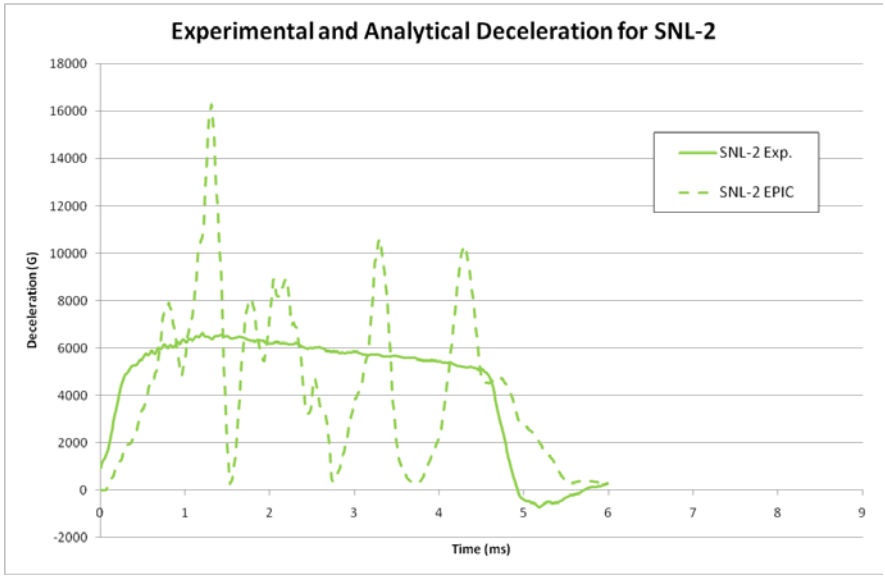

1.3. SNL-3

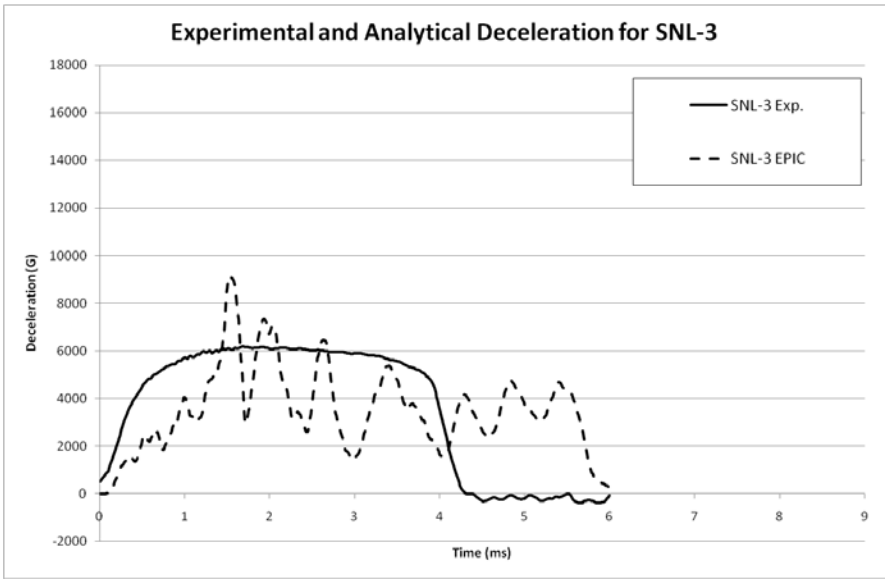

1.4. SNL-4

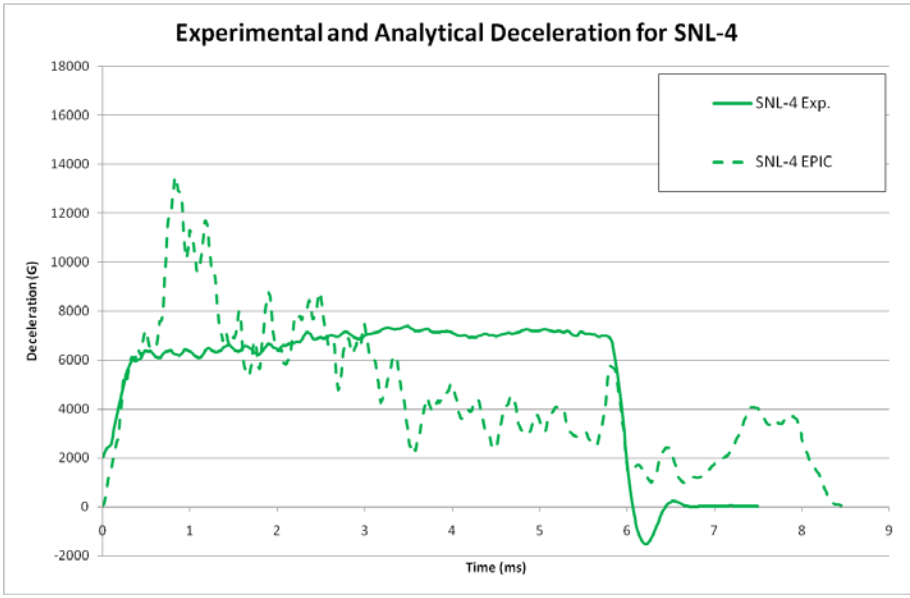

1.5. SNL-5

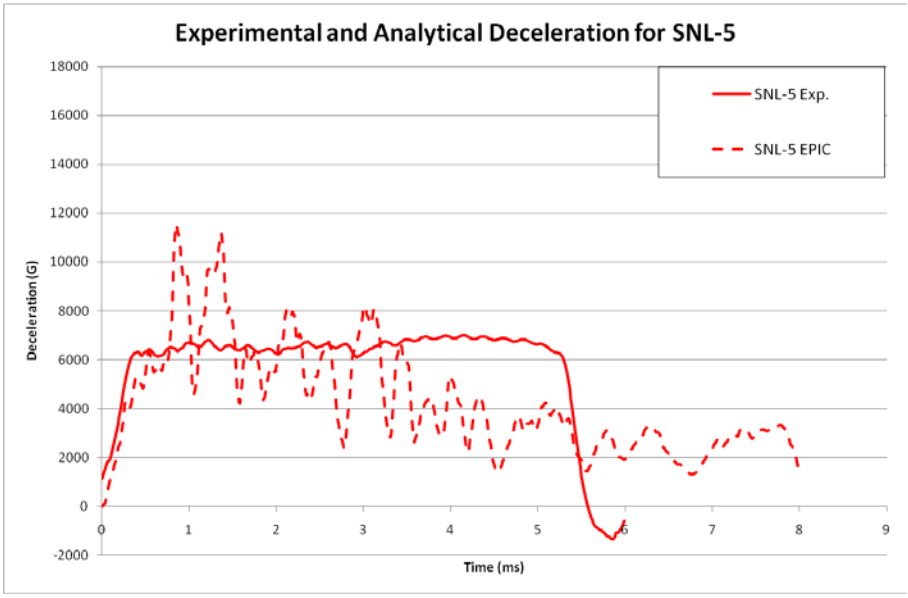

1.6. SNL-6

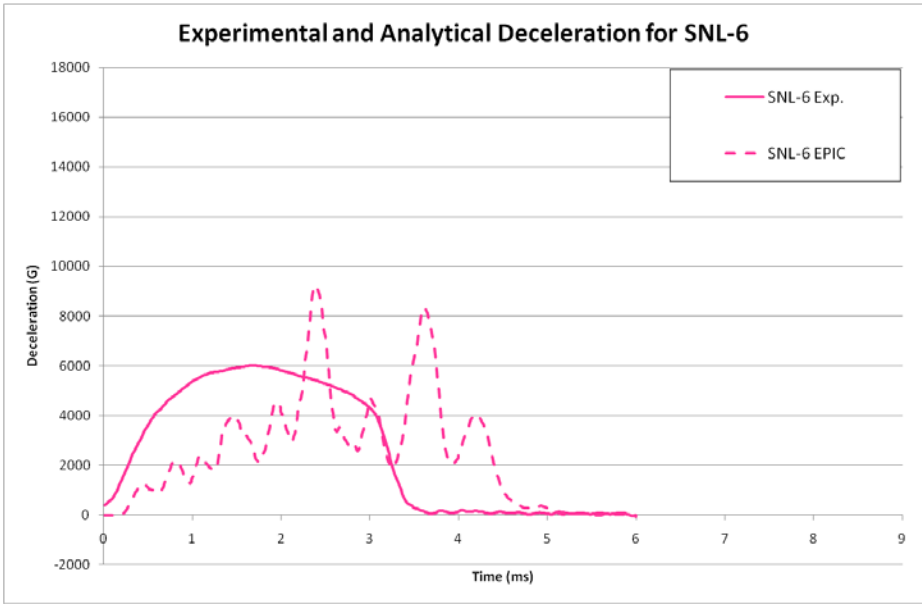

1.7. SNL-7

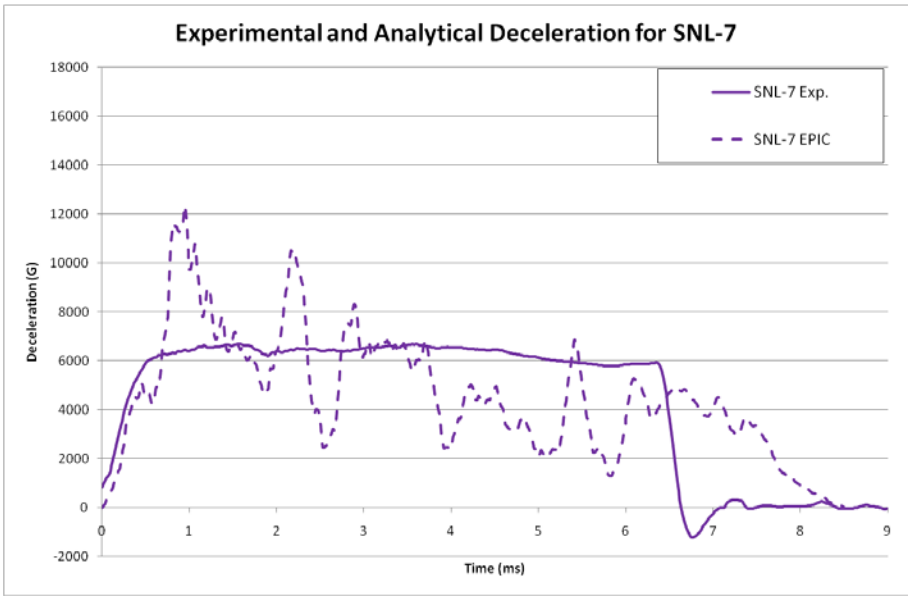

1.8. SNL-8

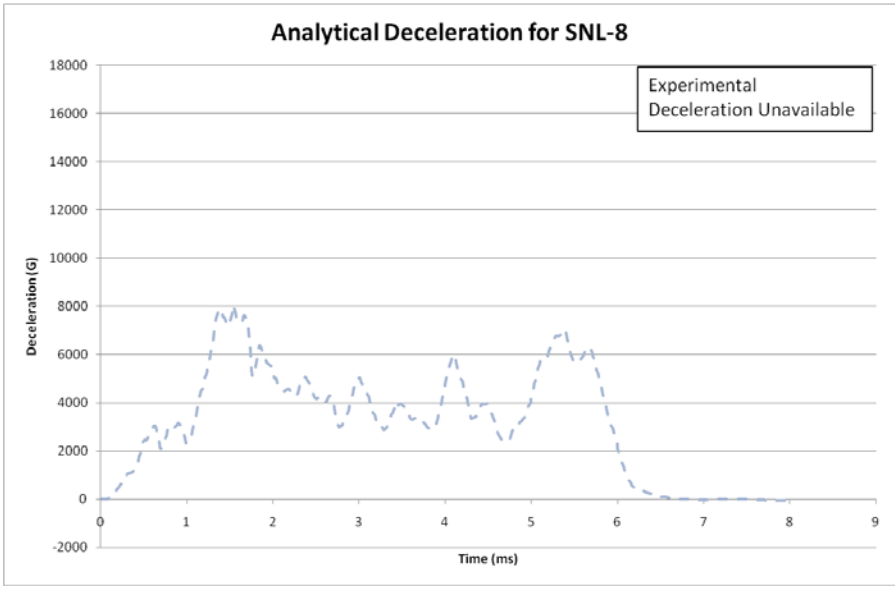

1.9. SNL-9

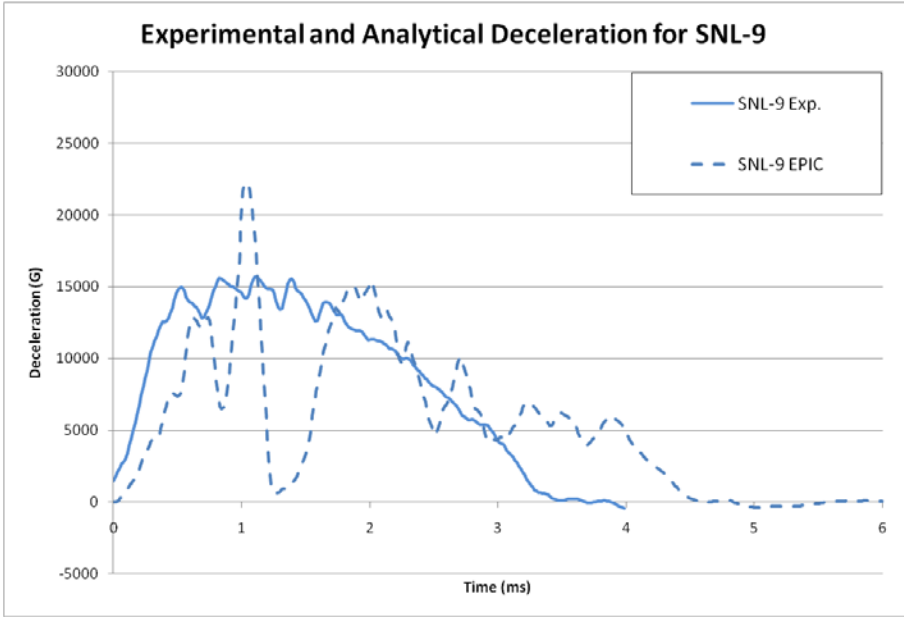

1.10. SNL-10

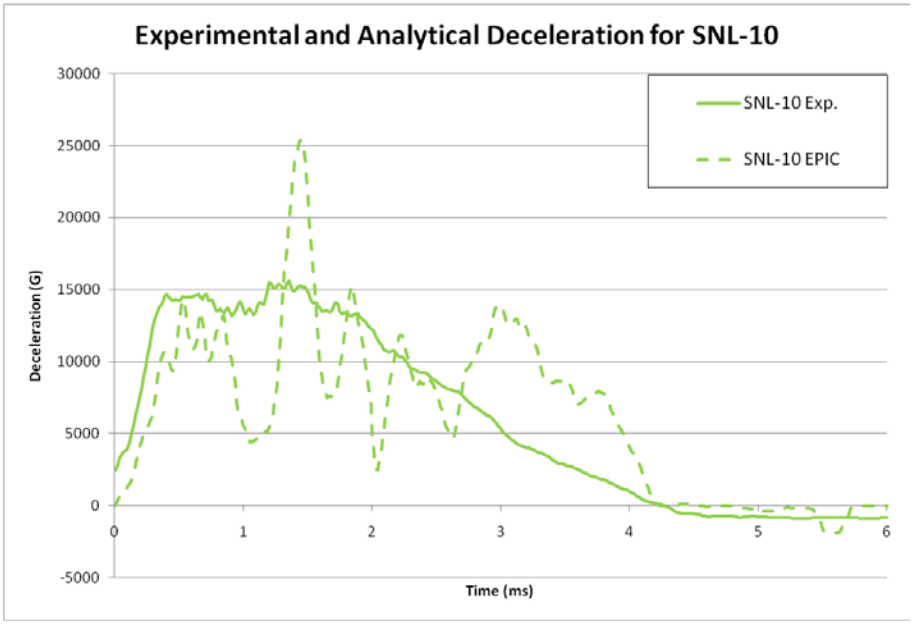

1.11. SNL-11

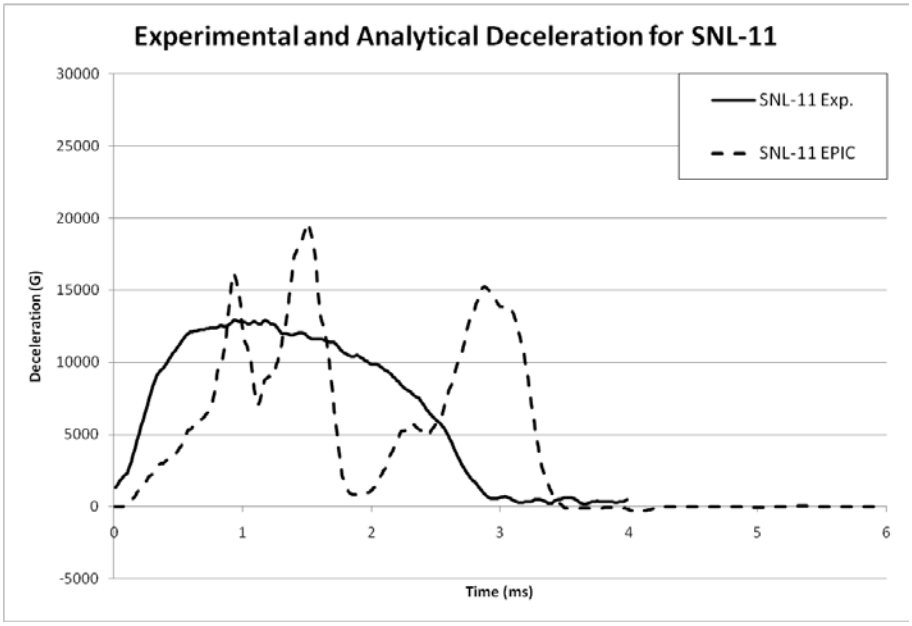

1.12. SNL-12

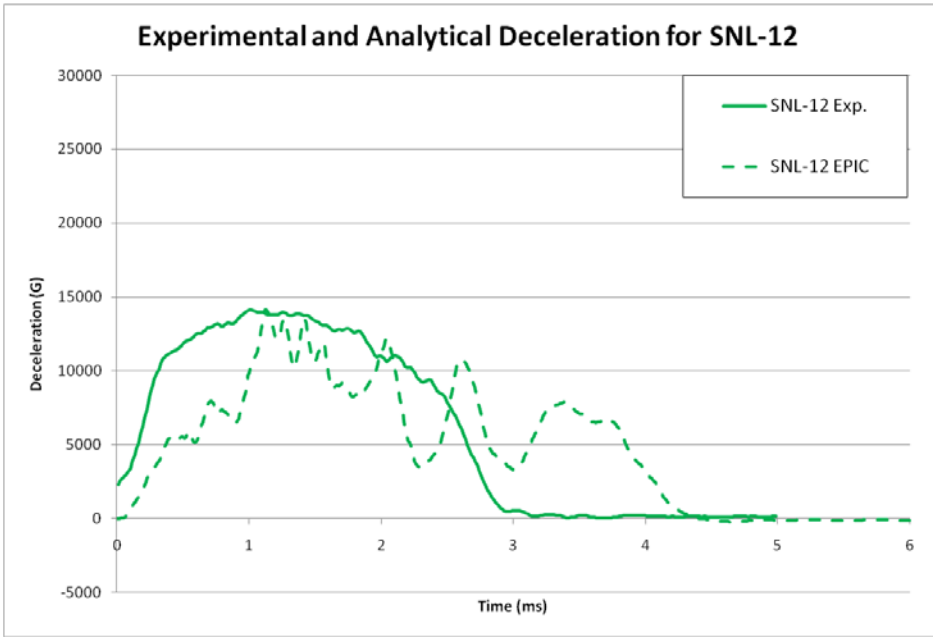

1.13. SNL-14

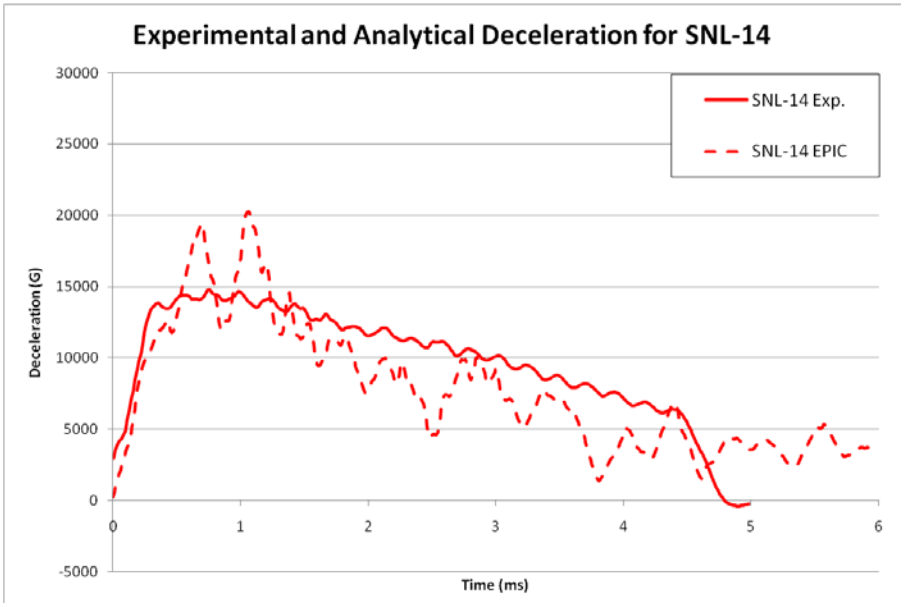

1.14. SNL-15

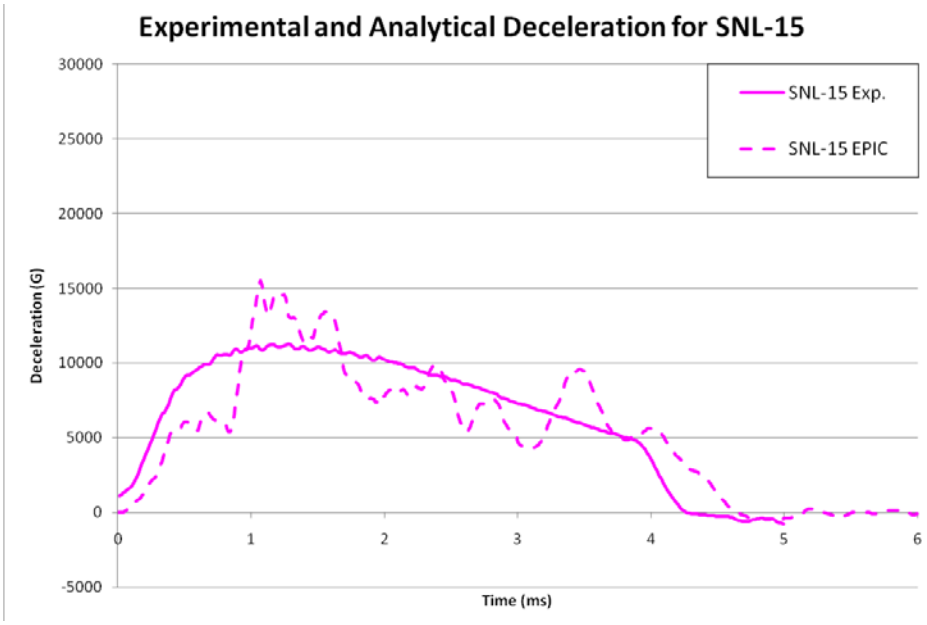

1.15. SNL-16

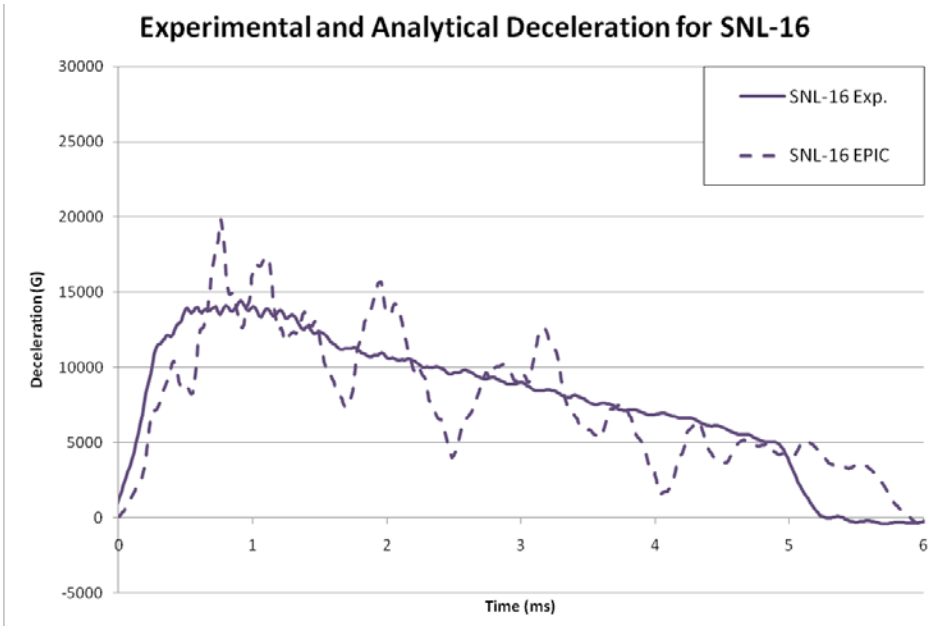

2. Experimental Parameter Study Damage Plots

This section contains the experimental damage images and profiles as well as the analytical damage contours for the experimental parameter study using the E-1 analysis pairing for the 15 experimental impact tests.

2.1. SNL-1



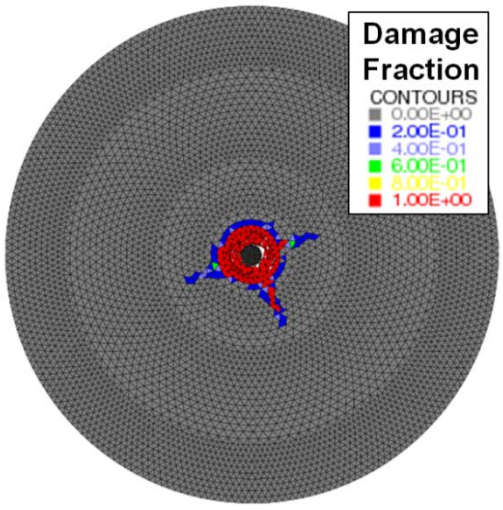

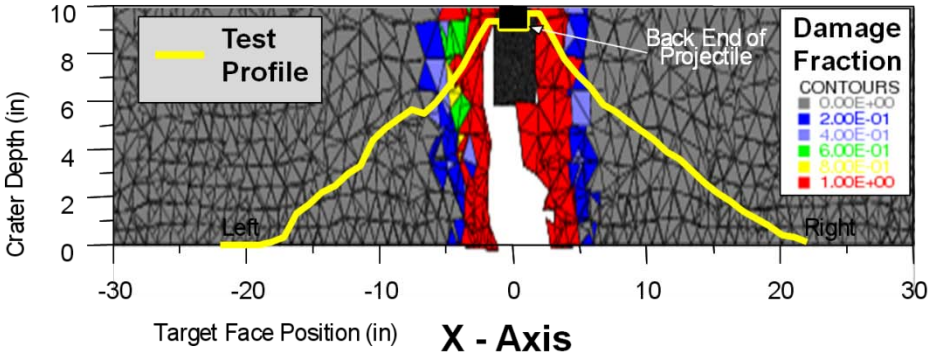

2.2. SNL-2

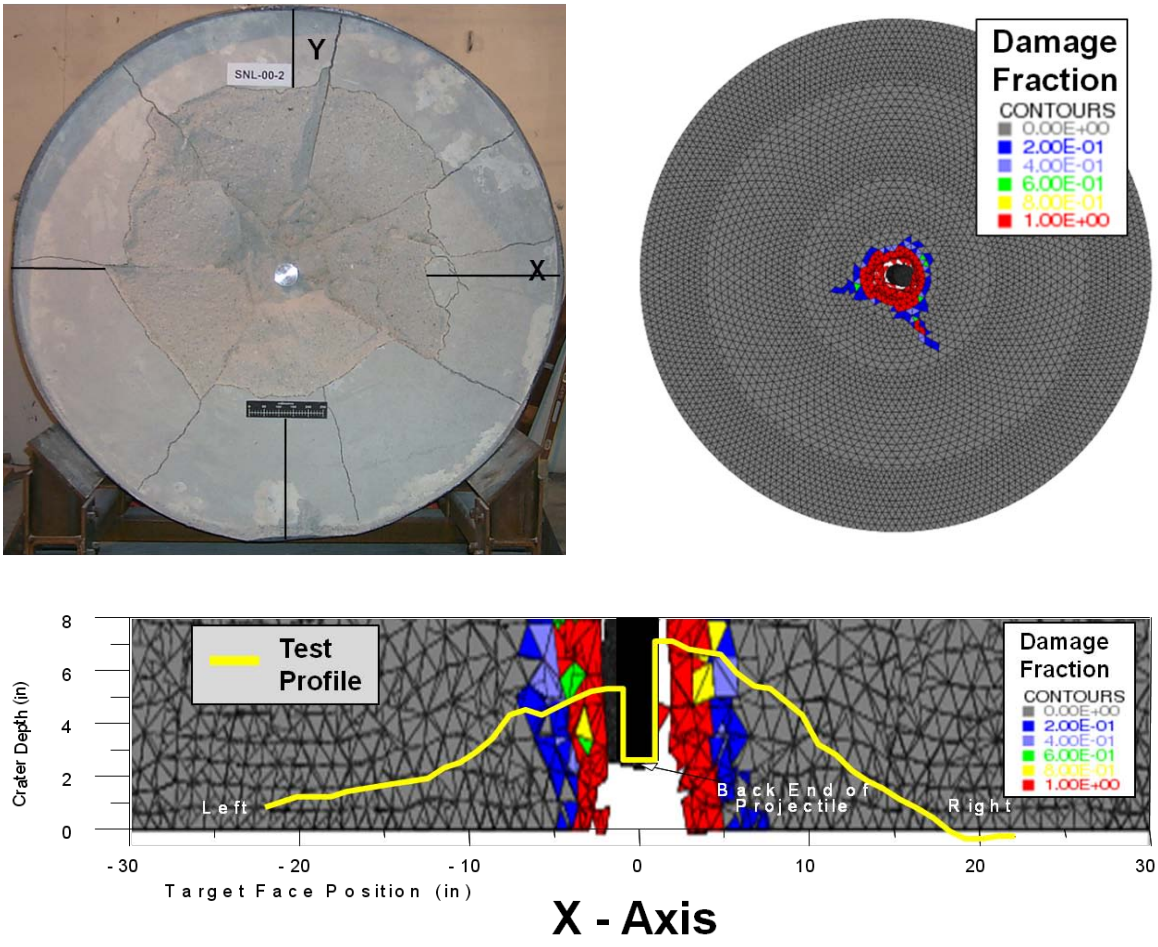
SNL-00-2
Y
X
Damage Fraction
CONTOURS
0.00E+00
2.00E-01
4.00E-01
6.00E-01
8.00E-01
1.00E+00
Test Profile
Crater Depth (in)
8
6
4
2
0
Left
Back End of Projectile
Right
- 30
- 20
- 10
0
10
20
30
Target Face Position (in)
X - Axis

2.3. SNL-3

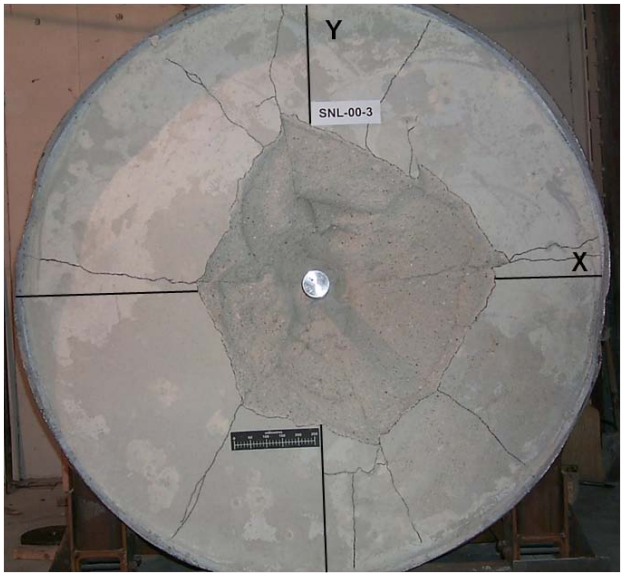
Y
SNL-00-3
X

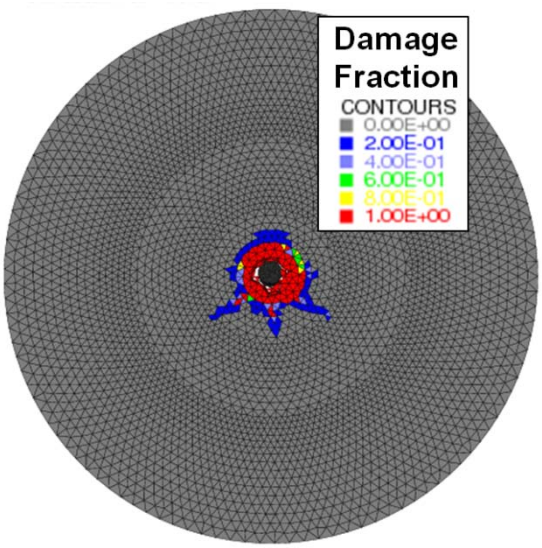
Damage Fraction
CONTOURS
0.00E+00
2.00E-01
4.00E-01
6.00E-01
8.00E-01
1.00E+00

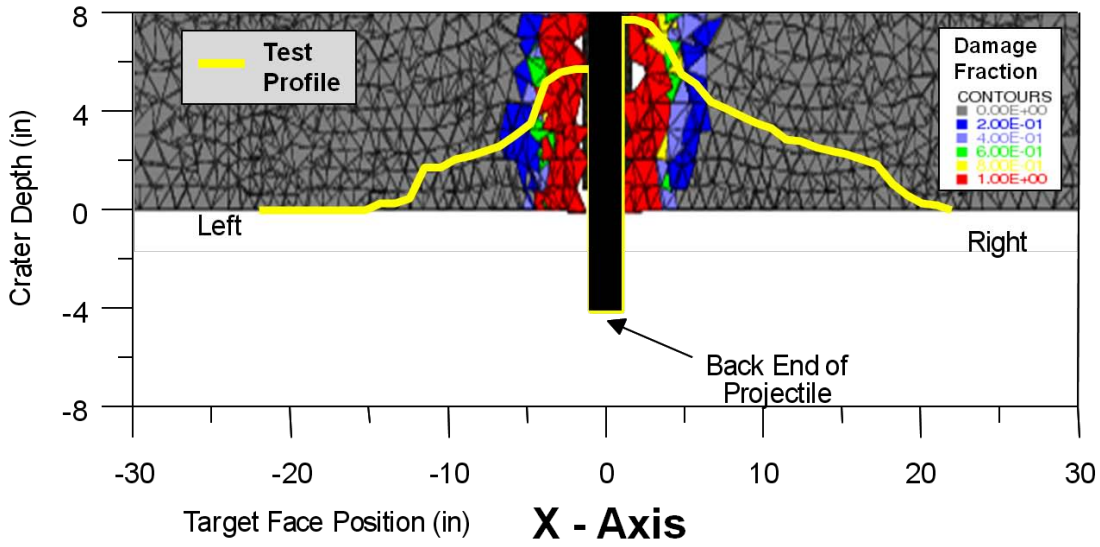
Test Profile
Damage Fraction
CONTOURS
0.00E+00
2.00E-01
4.00E-01
6.00E-01
8.00E-01
1.00E+00
Left
Right
Back End of Projectile
Crater Depth (in)
8
4
0
-4
-8
-30
-20
-10
0
10
20
30
Target Face Position (in)
X - Axis

2.4. SNL-4


Y
SNL-00-4
X

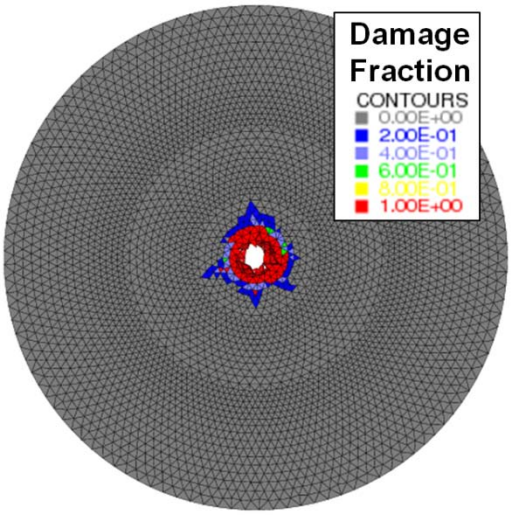
Damage Fraction
CONTOURS
0.00E+00
2.00E-01
4.00E-01
6.00E-01
8.00E-01
1.00E+00

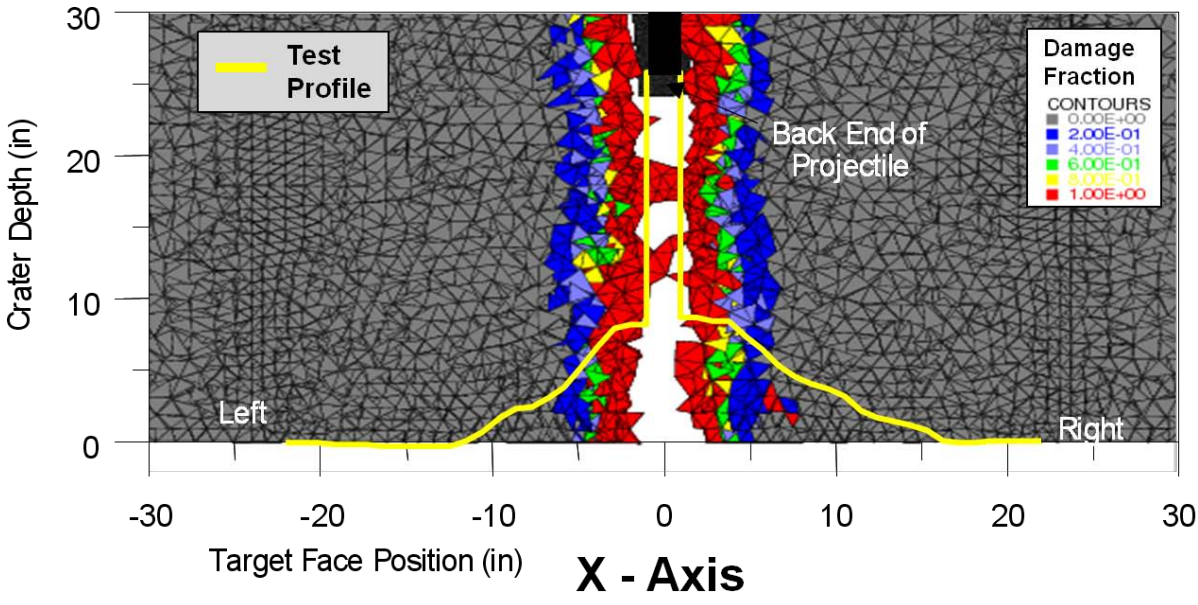
Test Profile
Back End of Projectile
Damage Fraction
CONTOURS
0.00E+00
2.00E-01
4.00E-01
6.00E-01
8.00E-01
1.00E+00
Crater Depth (in)
30
20
10
0
Left
Right
-30
-20
-10
0
10
20
30
Target Face Position (in)
X - Axis

2.5. SNL-5

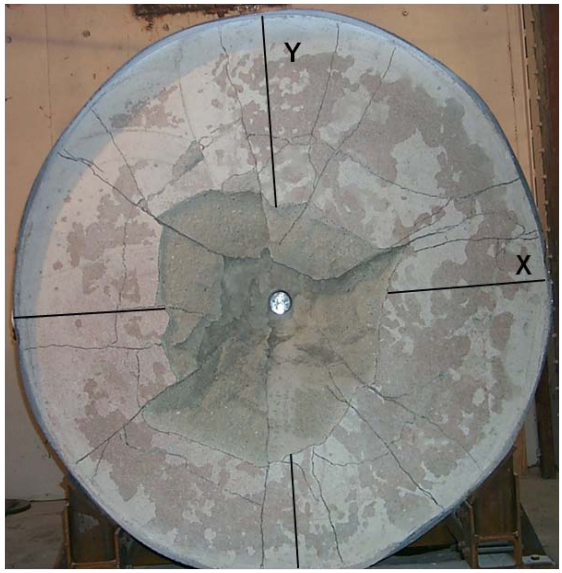
Y
X

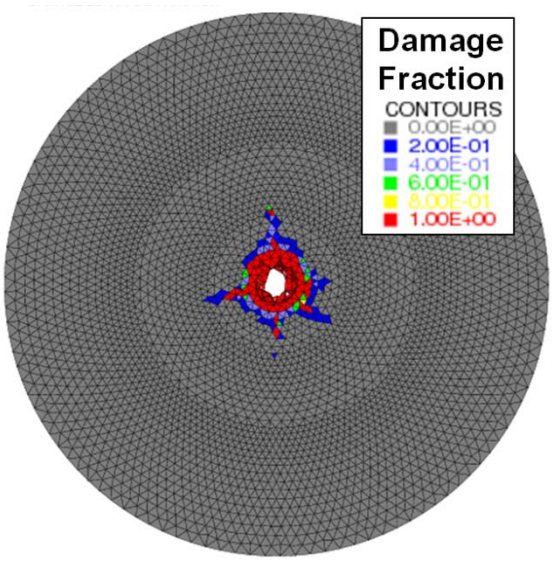
Damage Fraction
CONTOURS
0.00E+00
2.00E-01
4.00E-01
6.00E-01
8.00E-01
1.00E+00

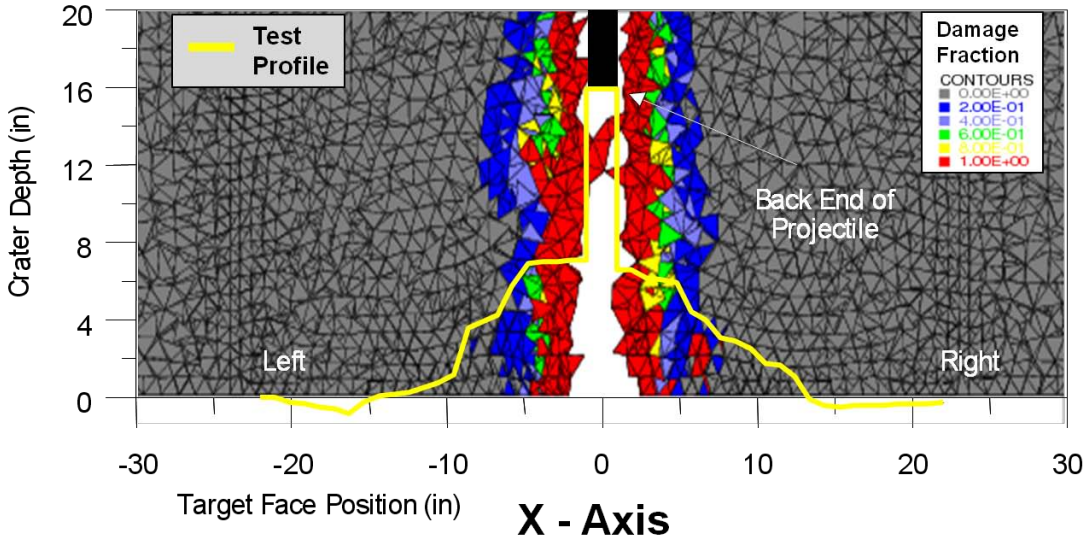
Test Profile
Damage Fraction
CONTOURS
0.00E+00
2.00E-01
4.00E-01
6.00E-01
8.00E-01
1.00E+00
Back End of Projectile
Left
Right
Crater Depth (in)
20
16
12
8
4
0
-30
-20
-10
0
10
20
30
Target Face Position (in)
X - Axis

2.6. SNL-6


SNL-00-6

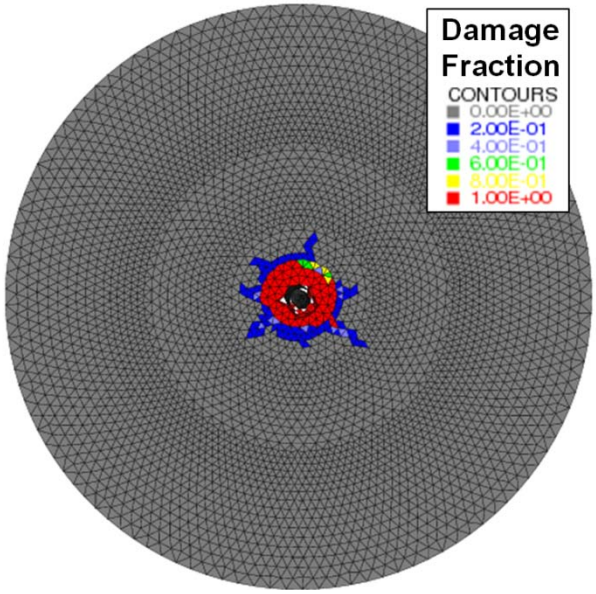
Damage Fraction
CONTOURS
0.00E+00
2.00E-01
4.00E-01
6.00E-01
8.00E-01
1.00E+00

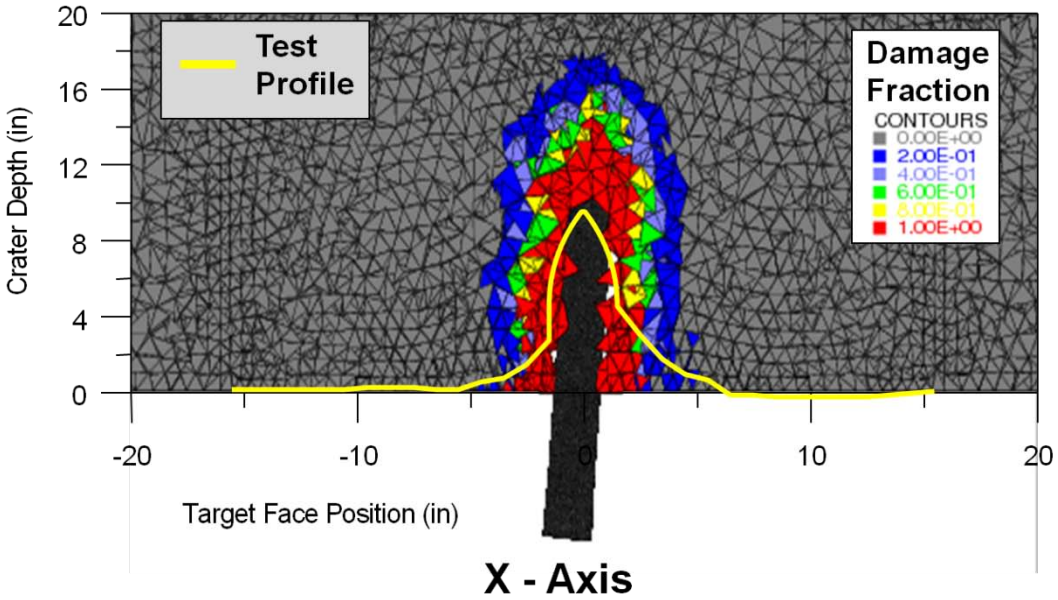
Test Profile
Damage Fraction
CONTOURS
0.00E+00
2.00E-01
4.00E-01
6.00E-01
8.00E-01
1.00E+00
Crater Depth (in)
20
16
12
8
4
0
-20
-10
0
10
20
Target Face Position (in)
X - Axis

2.7. SNL-7


SNL-00-7

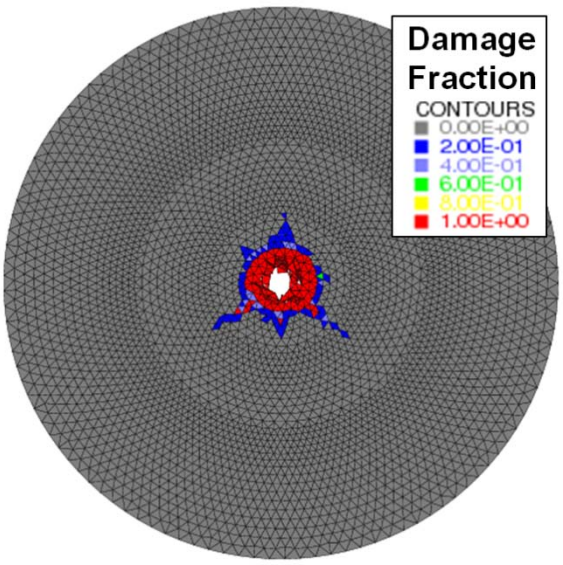
Damage
Fraction
CONTOURS
0.00E+00
2.00E-01
4.00E-01
6.00E-01
8.00E-01
1.00E+00

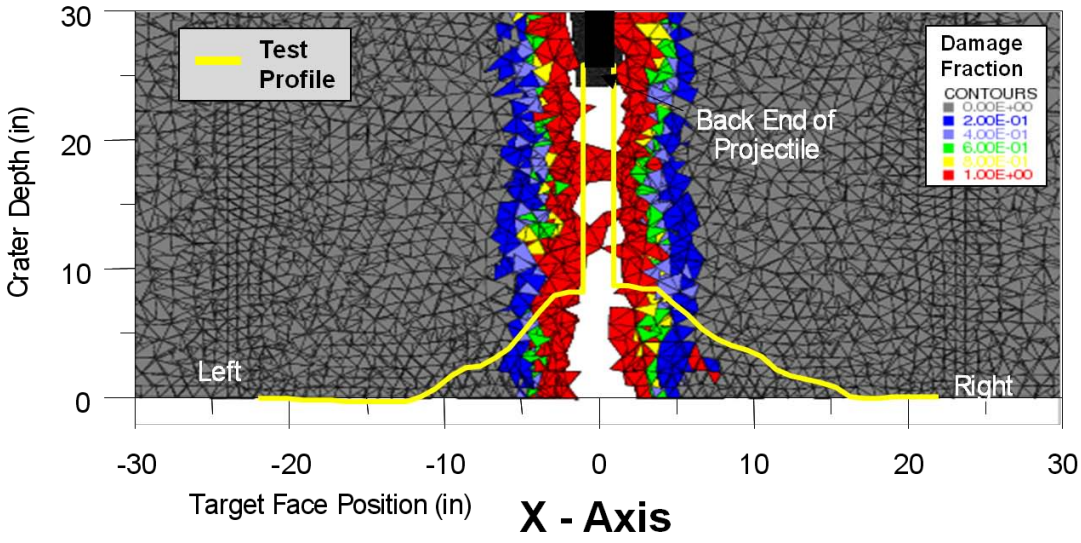
Test
Profile
Back End of
Projectile
Damage
Fraction
CONTOURS
0.00E+00
2.00E-01
4.00E-01
6.00E-01
8.00E-01
1.00E+00
Crater Depth (in)
30
20
10
0
Left
Right
-30
-20
-10
0
10
20
30
Target Face Position (in)
X - Axis

2.8. SNL-8



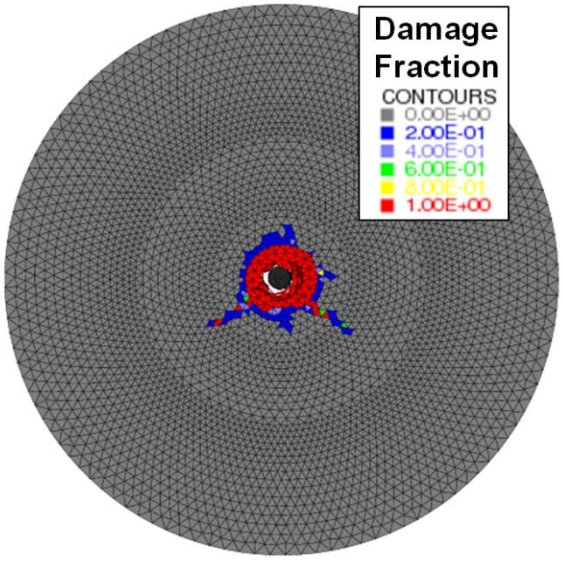
Damage Fraction
CONTOURS
0.00E+00
2.00E-01
4.00E-01
6.00E-01
8.00E-01
1.00E+00

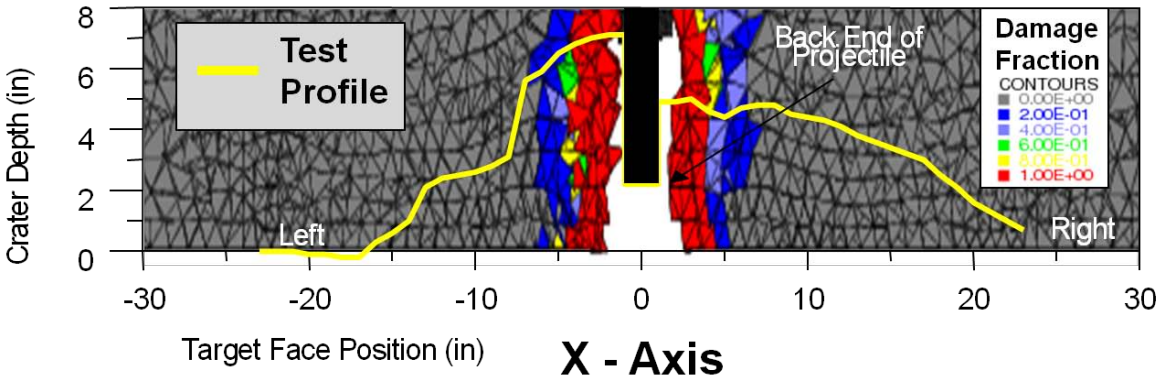
Test Profile
Back End of Projectile
Damage Fraction
CONTOURS
0.00E+00
2.00E-01
4.00E-01
6.00E-01
8.00E-01
1.00E+00
Left
Right
Crater Depth (in)
8
6
4
2
0
-30
-20
-10
0
10
20
30
Target Face Position (in)
X - Axis

2.9. SNL-9


SNL-00-9

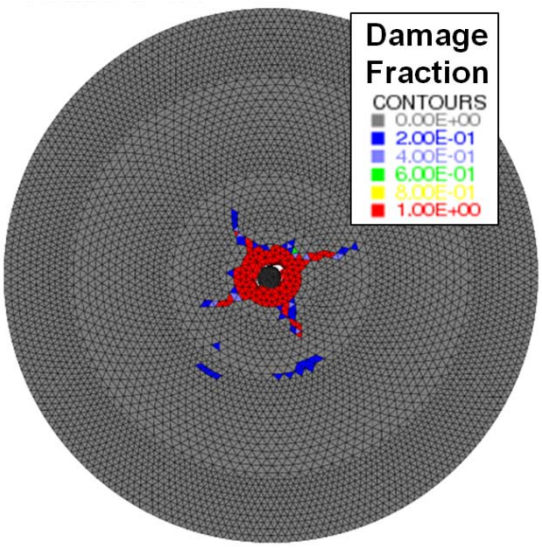
Damage
Fraction
CONTOURS
0.00E+00
2.00E-01
4.00E-01
6.00E-01
8.00E-01
1.00E+00

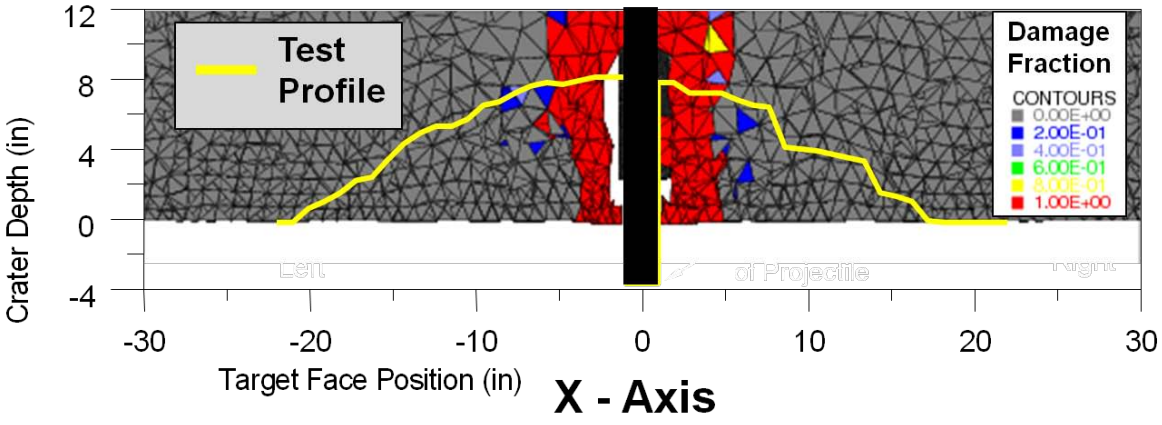
Test
Profile
Damage
Fraction
CONTOURS
0.00E+00
2.00E-01
4.00E-01
6.00E-01
8.00E-01
1.00E+00
Crater Depth (in)
12
8
4
0
-4
-30
-20
-10
0
10
20
30
Target Face Position (in)
X - Axis

2.10. SNL-10


SNL-00-10

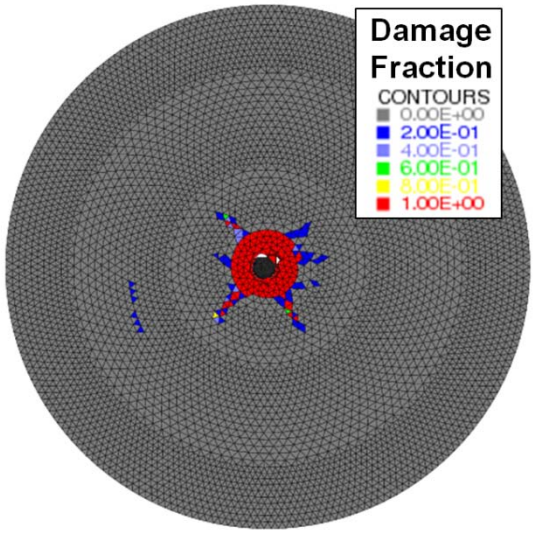
Damage Fraction
CONTOURS
0.00E+00
2.00E-01
4.00E-01
6.00E-01
8.00E-01
1.00E+00

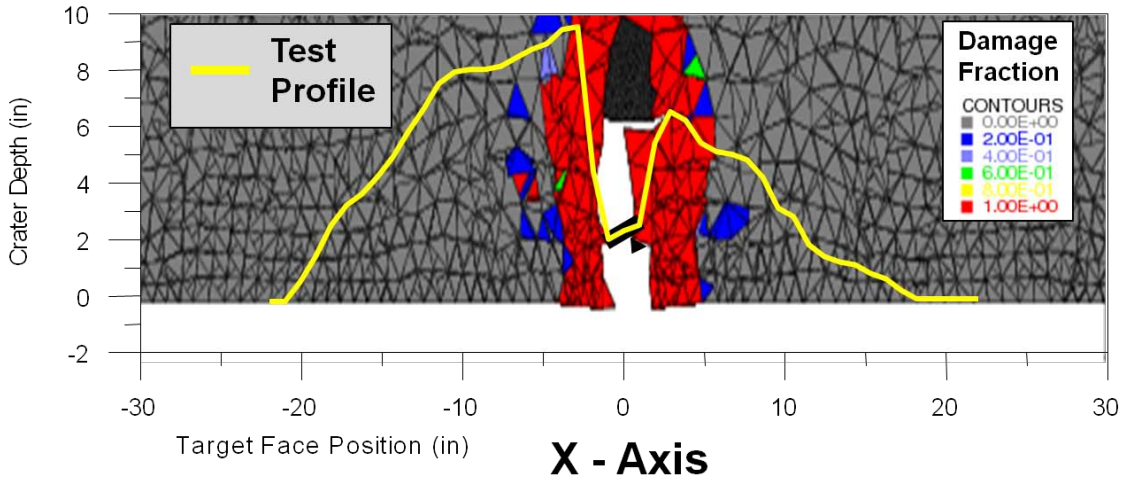
Test Profile
Damage Fraction
CONTOURS
0.00E+00
2.00E-01
4.00E-01
6.00E-01
8.00E-01
1.00E+00
Crater Depth (in)
10
8
6
4
2
0
-2
-30
-20
-10
0
10
20
30
Target Face Position (in)
X - Axis

2.11. SNL-11

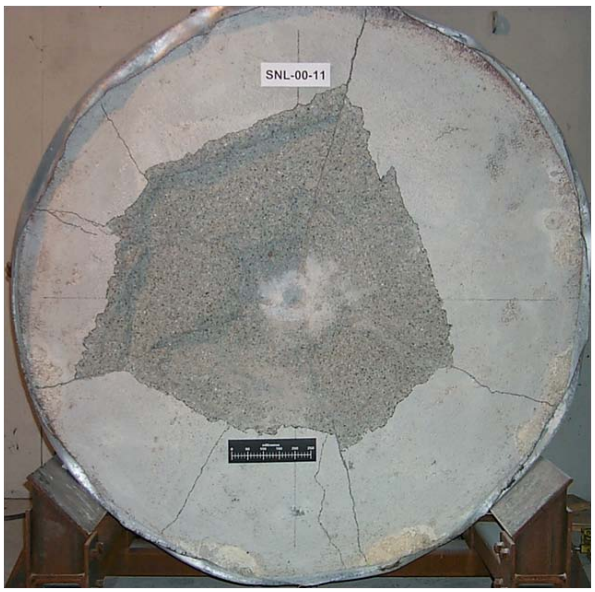
SNL-00-11

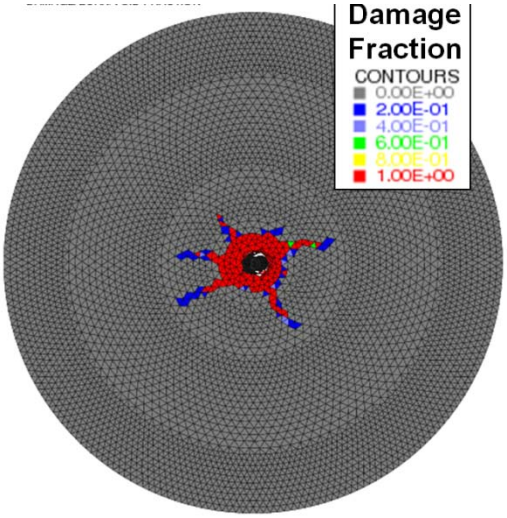
Damage Fraction
CONTOURS
0.00E+00
2.00E-01
4.00E-01
6.00E-01
8.00E-01
1.00E+00

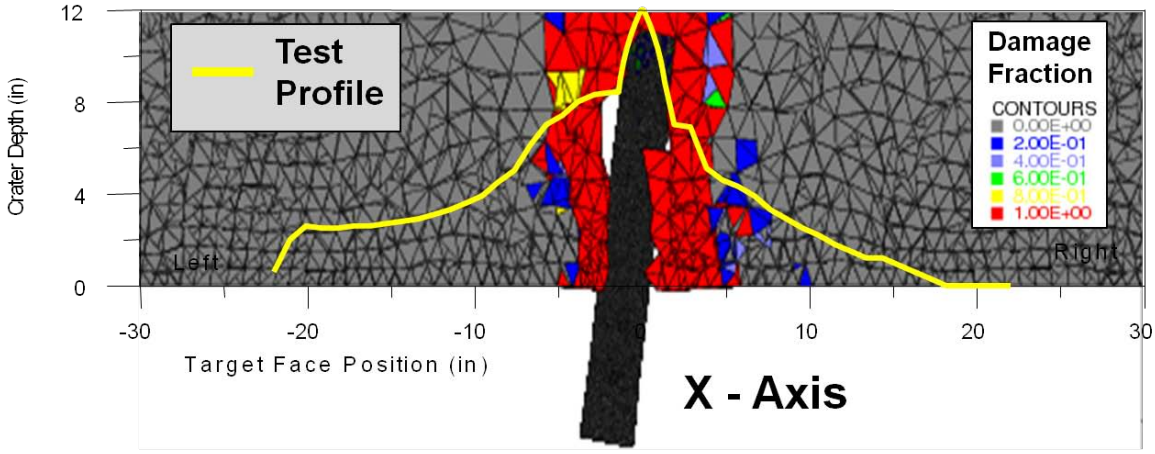
Test Profile
Damage Fraction
CONTOURS
0.00E+00
2.00E-01
4.00E-01
6.00E-01
8.00E-01
1.00E+00
Crater Depth (in)
12
8
4
0
Left
Right
-30
-20
-10
10
20
30
Target Face Position (in)
X - Axis

2.12. SNL-12



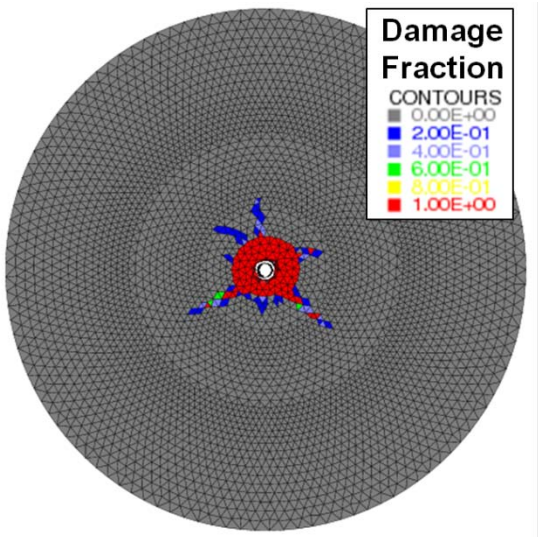
Damage
Fraction
CONTOURS
0.00E+00
2.00E-01
4.00E-01
6.00E-01
8.00E-01
1.00E+00

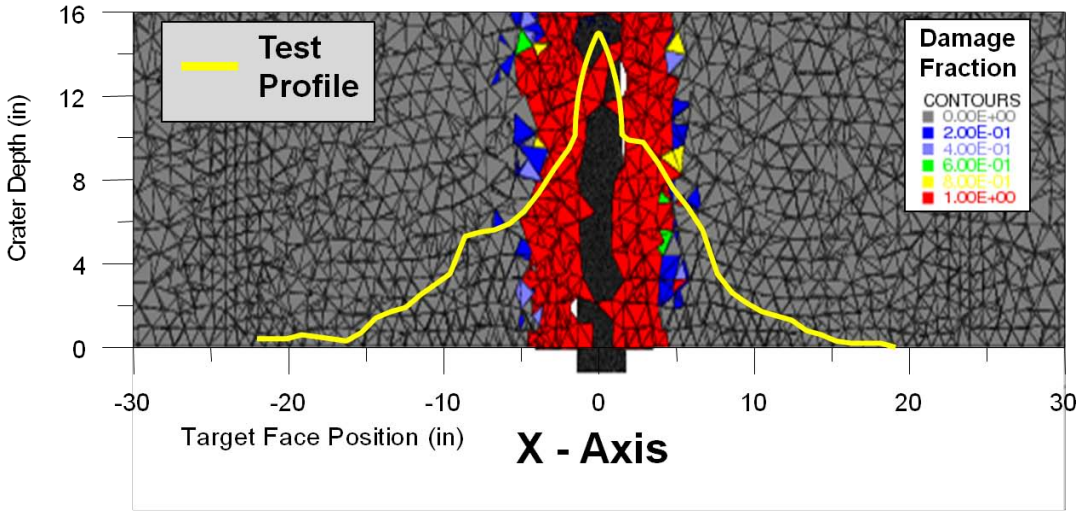
Test
Profile
Damage
Fraction
CONTOURS
0.00E+00
2.00E-01
4.00E-01
6.00E-01
8.00E-01
1.00E+00
Crater Depth (in)
16
12
8
4
0
-30
-20
-10
0
10
20
30
Target Face Position (in)
X - Axis

2.13. SNL-14


SNL-00-14

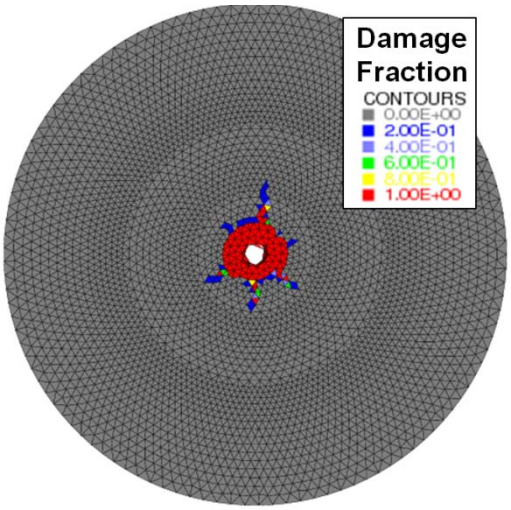
Damage Fraction
CONTOURS
0.00E+00
2.00E-01
4.00E-01
6.00E-01
8.00E-01
1.00E+00

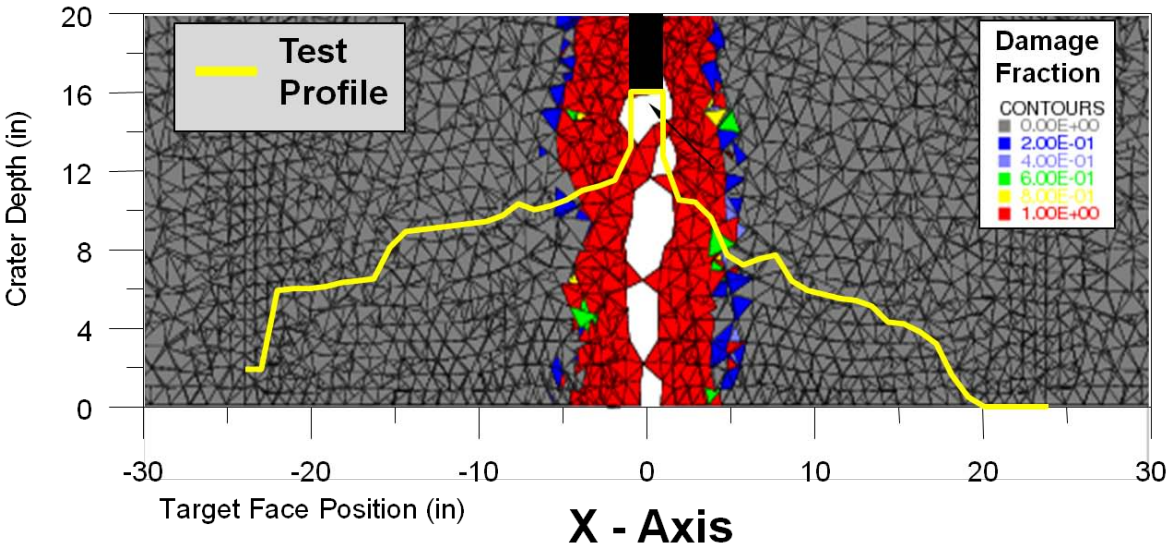
Test Profile
Damage Fraction
CONTOURS
0.00E+00
2.00E-01
4.00E-01
6.00E-01
8.00E-01
1.00E+00
Crater Depth (in)
20
16
12
8
4
0
-30
-20
-10
0
10
20
30
Target Face Position (in)
X - Axis

2.14. SNL-15


SNL-00-15

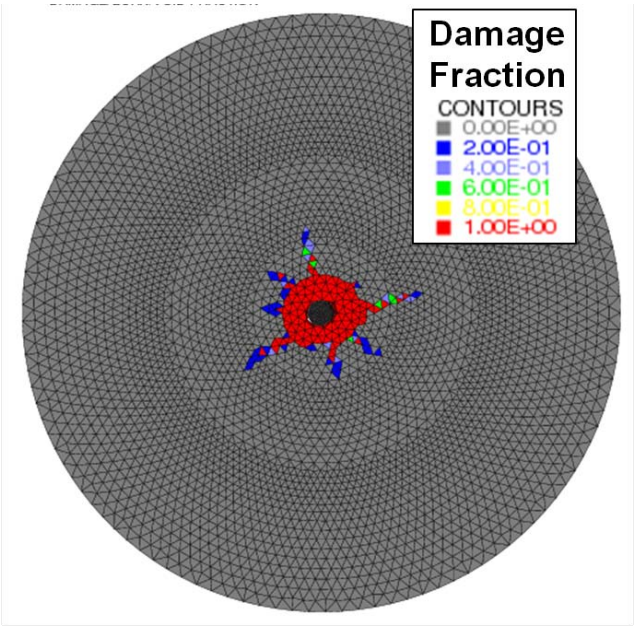
Damage Fraction
CONTOURS
0.00E+00
2.00E-01
4.00E-01
6.00E-01
8.00E-01
1.00E+00

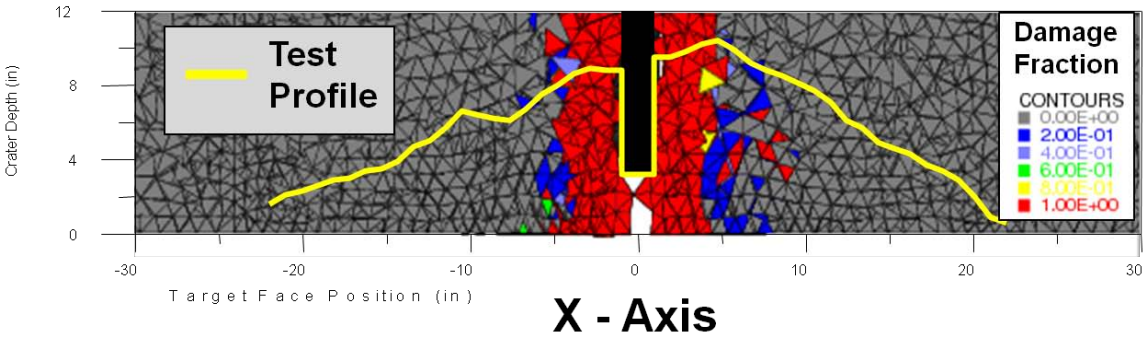
Test Profile
Damage Fraction
CONTOURS
0.00E+00
2.00E-01
4.00E-01
6.00E-01
8.00E-01
1.00E+00
Crater Depth (in)
12
8
4
0
-30
-20
-10
0
10
20
30
Target Face Position (in)
X - Axis

2.15. SNL-16

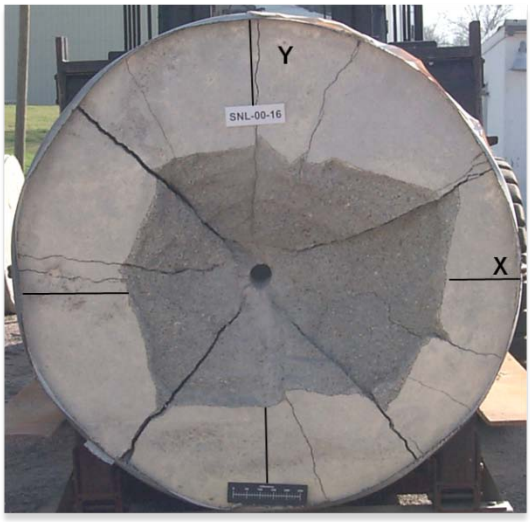
Y
SNL-00-16
X

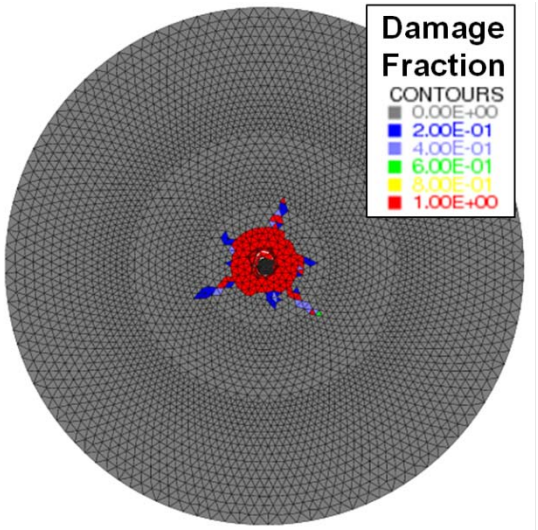
Damage Fraction
CONTOURS
0.00E+00
2.00E-01
4.00E-01
6.00E-01
8.00E-01
1.00E+00

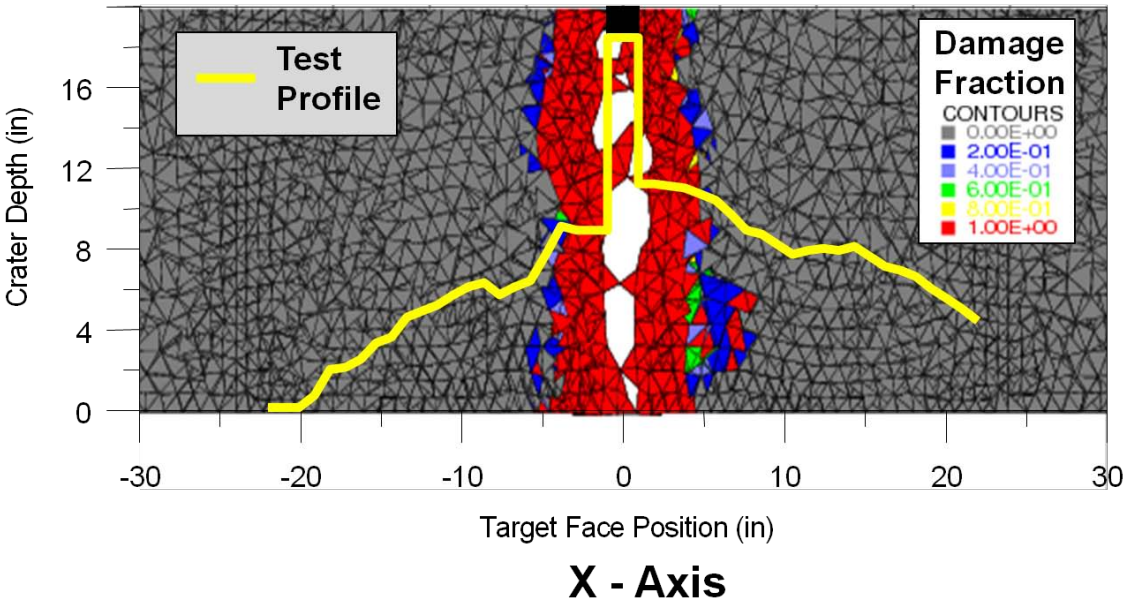
Test Profile
Damage Fraction
CONTOURS
0.00E+00
2.00E-01
4.00E-01
6.00E-01
8.00E-01
1.00E+00
Crater Depth (in)
16
12
8
4
0
-30
-20
-10
0
10
20
30
Target Face Position (in)
X - Axis